GEOTECHNICAL RESEARCH CENTRE

GRC STUDIES
on
SOIL PROPERTIES AND SOIL-WATER RELATIONS

SOIL MECHANICS SERIES No. 57

August 1993

McGill University
Montreal, Que Canada

ISSN 0541-6329

F O R E W O R D

The following selection of papers on Soil Properties and Soil-Water Relations has recently been published - the first two papers in the ASTM Geotechnical Testing Journal, and the last two in the Canadian Geotechnical Journal.

1. Mohamed, A.M.O., Yong, R.N., Caporuscio, F., Cheung, S.C.H. and Kjartanson, B.H. (1993)
   A Coupled Heat and Water Flow Apparatus pp.85-99.

2. Mohamed, A.M.O., Yong, R.N., and Cheung, S.C.H. (1992)
   Temperature Dependence of Soil Water Potential pp.330-339.

3. Yong, R.N. and Mohamed, A.M.O. (1992)
   A Study of Particle Interaction Energies in Wetting of Unsaturated Expansive Clays pp.1060-1070.

4. Yong, R.N., Mohamed, A.M.O. and Wang, B.W. (1992)
   Influence of Amorphous Silica and Iron Hydroxide on Interparticle Action and Soil Surface Properties pp.803-818.

Abdel-Mohsen O. Mohamed,[1] *Raymond N. Yong,*[2] *Frank Caporouscio,*[3] *Steven C. H. Cheung,*[4] *and Bruce H. Kjartanson*[5]

Authorized Reprint 1993 from Geotechnical Testing Journal, MARCH 1993

A Coupled Heat and Water Flow Apparatus

REFERENCE: Mohamed, A. M. O., Yong, R. N., Caporuscio, F., Cheung, S. C. H., and Kjartanson, B. H., "A Coupled Heat and Water Flow Apparatus," *Geotechnical Testing Journal*, GTJODJ, Vol. 16, No. 1, March 1993, pp. 85-99.

ABSTRACT: To study the performance of a compacted buffer material under thermal and isothermal conditions, a coupled heat and water flow apparatus is designed and presented. In the preliminary design, a one dimensional flow of heat and water was not achieved. However, control of temperature gradient, existence of one-dimensional flow, and uniformity of temperature and volumetric water content distributions at any cross section within the specimen are achieved in the modified design.

Experimental results have shown that the temperature stabilizes very rapidly after a period of approximately 6,107 days. The moisture moves away from the hot end along the longitudinal direction of the specimen due to imposed thermal gradient. The time required for moisture to stabilize is in order of days.

KEYWORDS: moisture, flow, temperature, unsaturated flow, expansive, transient, insulation, cooling, one dimensional, diffusion

Safe and permanent disposal of radioactive waste requires isolation of a number of diverse chemical elements from the environment. The Canadian Nuclear Fuel Waste Management Program is assessing the concept of disposing of waste in a vault excavated at a depth of 500 to 1000 m below the ground surface in plutonic rock of the Canadian Shield. Besides the natural low-permeability rock, a number of engineered barriers are used to limit radionuclide release. These are the corrosion-resistant container, the buffer, and the backfill. The containers will be placed in boreholes drilled into the floors of emplacement rooms and separated from the host rock by bentonite-sand buffer material. The remainder of the vault will be filled with an earthen, clay-based backfill.

The buffer and backfill will be compacted clay-based materials with low ionic and hydraulic diffusivities (Cheung et al. 1987; Mohamed et al. 1990). The mineral compositions and engineering properties of the buffer and backfill have been reported elsewhere (Gray and Cheung 1986; Yong et al. 1986). The hydraulic pressure, temperature, and solute concentrations in the pore water will vary spatially and temporally in the clay barrier materials. Multi-flow of heat, water, and dissolved solids, including radionuclides released from breached containers, will occur in the clay barriers under the changing driving gradients (Cheung and Gray 1990; Mohamed et al. 1990).

In the Canadian disposal vault, temperatures and hydraulic potentials in the buffer and backfill material are expected to be as follows.

Temperatures

The heat produced by radioactive decay of the waste in the container will be dissipated through the buffer, backfill, and rock. The temperature will decrease away from the container, and the temperature gradient will be higher in the region closest to the container. The vault is designed generally to limit maximum temperature at the surface of the container to 100°C or less. After 500 years [the minimum design container lifetime (Hancox 1986)], container surface temperatures will be less than 100°C and a maximum temperature gradient of 1°C/m in the buffer is estimated from the overall heat transfer processes.

Hydraulic Conditions

The hydraulic conditions in the buffer and backfill depend on, among other factors, the permeability of the surrounding rock. The naturally lower permeability of the intact rock can be significantly increased by natural fractures. Excavation of the vault will induce fracturing in the rock surrounding the excavation, and the extent of induced fracturing will depend on the excavation method, geometry and orientation, and the stress field in the rock mass. For the Canadian disposal vault, it is proposed that the rooms and shafts will be excavated by blasting, the boreholes in which the buffer and waste will be emplaced will be drilled or bored.

The time it takes to water-saturate the barrier materials under in-situ rock conditions at the Stripa Mine, Sweden has been investigated (Pusch et al. 1985). This study showed that the backfill could become virtually water saturated in a few years. The time it will take to saturate the buffer in the boreholes will be longer and will vary with the frequency with which natural water-bearing fractures are intersected by the borehole and the availability of groundwater.

[1]Research associate, Geotechnical Research Centre (GRC), adjunct professor, Civil Engineering Dept., McGill University, 817 Sherbrooke St. West, Montreal, Quebec H3A 2K6.

[2]William Scott Professor, Civil Engineering Dept., Director, GRC, McGill University.

[3]Research assistant, GRC, McGill University.

[4]Associate professor, Civil Engineering Dept., Concordia University, 1455 de Maisonneuve Blvd., West, Montreal, Quebec H3G 1M8.

[5]Research scientist, AECL Research, Whiteshell Laboratories, Pinawa, Manitoba, Canada R0E 1L0.

During the presaturation period, buffer near the container could undergo drying, shrinkage, and cracking due to heat-induced moisture movement away from the container. These processes tend to reduce the buffer's thermal conductivity, resulting in higher container temperatures and perhaps further moisture movement. The condition of the buffer near the rock will depend on the degree of thermally induced moisture redistribution and the moisture boundary conditions. Thus, to a large extent, processes and conditions in the buffer will depend on local moisture content and moisture transients during the presaturation period. Understanding the coupled processes of heat and moisture transfer is thus important to confirming in-situ buffer performance.

This study is focused on the transport processes in the buffer material before full saturation. Much research has been done on coupled heat and mass flows in unsaturated soils. Smith (1943) and Philip and de Vries (1957) have postulated a moisture transfer model consisting of a series of evaporation and condensation steps together with a discontinuous flow of liquid film. Taylor and Cary (1960) and Nielsen et al. (1972) applied nonequilibrium thermodynamics to analyze the associated coupling effects.

Generally, the following two approaches were used. The first approach is mechanistic (Philip and Vries 1957) and requires that physical properties of the porous system affecting both heat and moisture movement be known so that reliable estimates can be made of the individual diffusion parameters in the transport equation. Yong et al. (1990) presented a comparative study using Cassel et al. (1969), in which the calculations were made for a nonswelling soil and showed that there is a difference of at least one order of magnitude between the values calculated for the isothermal water diffusivity coefficient by the Yong and Xu (1988) model (based on experimental data as well as on an identification technique) and the Philip and de Vries (1957) model (based on a mechanistic approach). The discrepancies with the Philip and de Vries model can be attributed to: (1) not considering the full coupling effect; (2) not accommodating fully any considerations for vapor transfer and the resultant pressure gradient; and (3) assumptions related to the independence of the soil water potential with temperature. Furthermore, the role of locked-in stresses and associated volume change or developed swelling pressure (local) within the system as moisture transfer progresses have not been taken into consideration for swelling soils in the Philip and de Vries model.

The second approach (Yong and Xu 1988; Yong et al. 1990; Mohamed et al. 1990), which directly uses experimental data, requires that the moisture distribution and the temperature distributions in the time domain be measured. Then the diffusion parameters can be calculated by using the measured profiles and an identification technique. The basic principle of the identification technique used to determine the coefficients of the diffusion parameters relies on matching experimentally obtained values for volumetric water content and temperature at various time states of a controlled test with the predicted diffusion parameters.

The preceding highlights the need for experimental data of temperature and moisture distributions as functions of space and time in order to accurately predict the heat and moisture flow in unsaturated buffer material. Therefore, this study is designed to provide the necessary experimental data for both temperature and moisture distributions. A coupled heat and moisture flow apparatus has been designed and fabricated at the Geotechnical Research Centre of McGill University for this purpose. This paper describes the stages of development of this apparatus and presents the time-dependent temperature and moisture-content profiles of a compacted buffer subjected to specified boundary conditions to demonstrate the reliability and versatility of the apparatus.

Description of the Apparatus

Testing Cell

In the design of the coupled heat and moisture flow apparatus, the following criteria were considered:

1. One-dimensional heat and moisture flow has to be ensured for simplicity in measurement and analysis.
2. The temperature and hydraulic gradient can be applied in the same or opposite directions. The range of the temperature gradient and the maximum temperature in the soil are 20 to 500°C/m and 100°C, respectively. The apparatus must be capable of controlling the influx and efflux of water. This criterion is adapted specifically to meet the thermal and hydraulic environment of clay-based sealing materials used in the Canadian Nuclear Fuel Waste Disposal Vault (Yong et al. 1989, 1990). For example, before the near field hydraulic conditions are reestablished and during the early stages of closure of the vault, the system may be simulated by a closed system. As the hydraulic conditions reestablish, the buffer adsorbs water from the surrounding rock and the system is simulated by an open system.
3. Under the imposed temperature and/or hydraulic gradients, the soil pressure—due to swelling and thermal expansion, temperature, and soil moisture content—has to be measured as a function of time and space. This criterion is adopted in order to provide the necessary input data for modelling heat and moisture flow in buffer material. Hence, thermal and hydraulic diffusivity parameters can be calculated. Furthermore, dependence of diffusivity parameters on the initial water content and imposed temperature can be characterized.
4. The cell has to be sufficiently rigid to withstand the high compactive forces used in specimen preparation and swelling pressure of soil during heating and rewetting.

Preliminary Design

A schematic design meeting the above criteria is shown in Fig. 1. Each end of the specimen can be heated or cooled with a temperature-controlled plate. A pressure transducer (h—Fig. 1) is encased in one of the end plates to measure the development of buffer pressure, which may be used to indicate movement of water with development of swelling pressure (Yong et al. 1990). The specimen is insulated around its outer surface by a PVC liner (l—Fig. 1). The PVC liner is capable of resisting the compactive and swelling pressure. It is then encased with concrete (m—Fig. 1) and steel tube (n—Fig. 1) around its perimeter and steel plates at its ends. A copper cooling coil is installed inside the concrete and on one of the end plates (q—Fig. 1). Its role is to act as a heat sink so that the constant temperature of the concrete can be maintained and the temperature of the end plates can be lowered to create a temperature gradient within the buffer material. The dimensions of the specimen are 203.20 mm in

diameter by 87.00 mm in length. This arrangement in dimensions is intended to: (1) provide one-dimensional flow of heat and moisture in the middle third of the buffer material; and (2) be used for testing the backfill material which contains aggregate sizes up to 20 mm (Yong et al. 1986).

Temperature Control Unit

Temperature gradients in the buffer material were imposed by heating one of the end plates with a 124-W (ring-type) element heater. The dimensions of the heater are 63.50 mm in diameter by 7.62 mm in thickness (e — Fig. 1). A copper plate (f — Fig. 1) was housed in the piston base plate (c — Fig. 1) to transmit the heat to the buffer material. The dimensions of the copper plate are 203.20 mm in diameter by 6.35 mm in thickness. The heater supply was automatically controlled to maintain the constant elevated temperature required at the end plate. The temperature control unit used in this investigation is shown in Fig. 2. Each time the heater was activated, the time totalizer would record the total time of heater supply output, from which the cumulative thermal energy was calculated. It should be noted that the heater diameter is about one third of the copper plate diameter. It was assumed that the heat could be conducted very rapidly and there would be no loss of heat from its surroundings. This will be shown later to be insufficient. It needs to be further corrected.

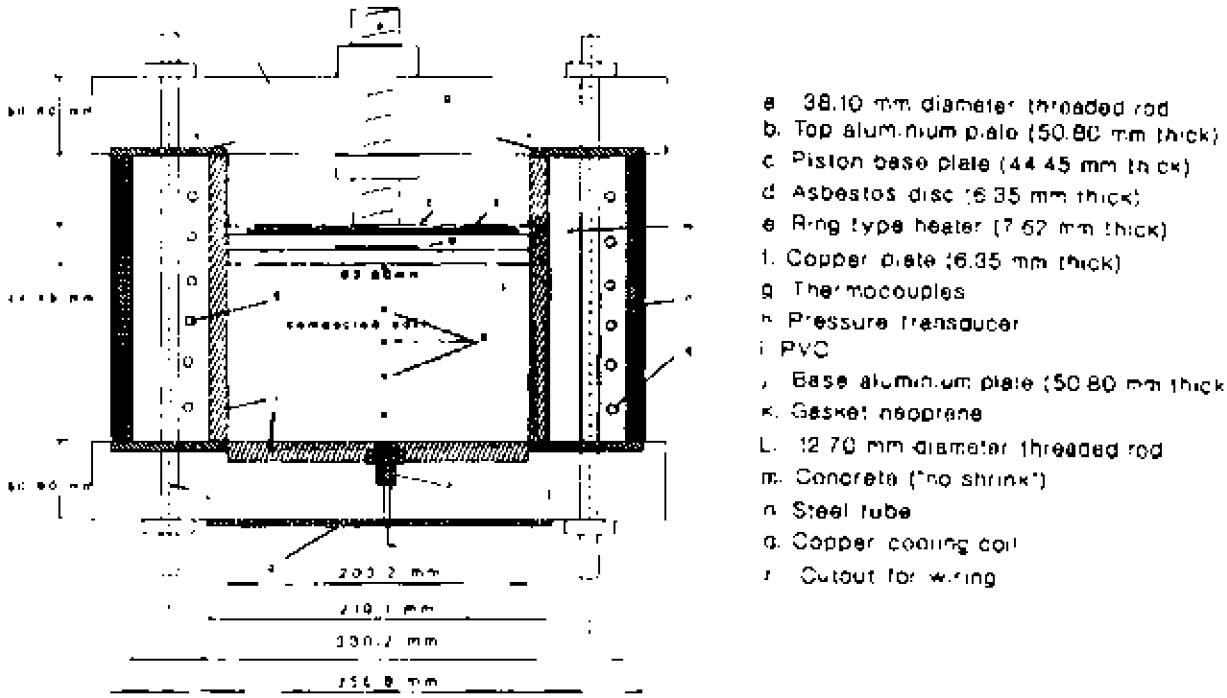

FIG. 1 — *Schematic diagram of the preliminary design of the heating cell*

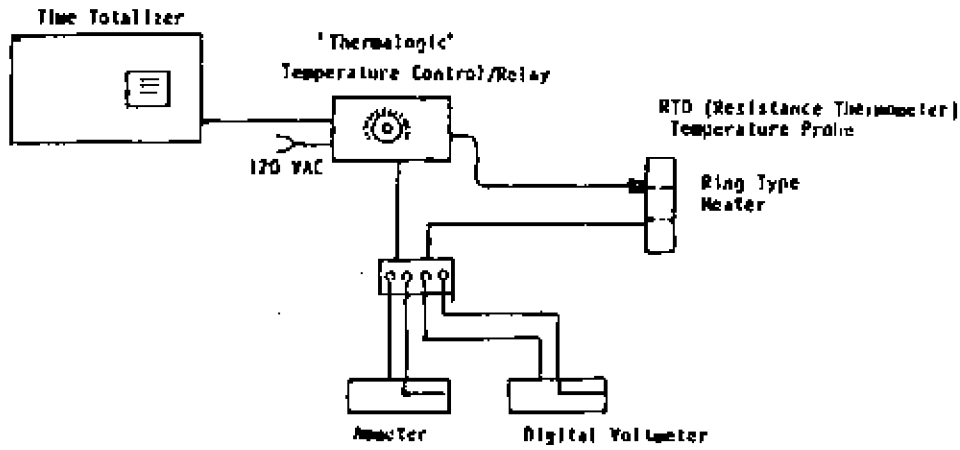

FIG. 2—*Temperature control unit.*

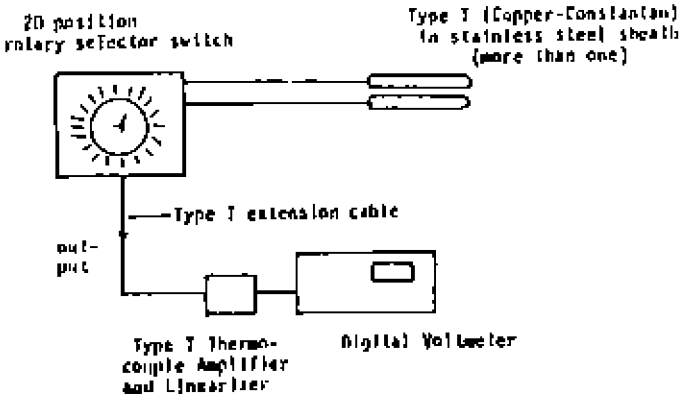

FIG. 3—*Temperature monitoring unit*

Temperature Monitoring Unit

The temperatures within the buffer material were monitored by Type T (Copper-Constantan) thermocouples, each encased in a stainless steel sheath. A 20-position rotary selector is set to read the various thermocouples installed (Fig. 3). A Type T thermocouple amplifier and linearizer unit is used to convert the thermocouple millivolts to degrees centigrade to be read by the digital voltmeters.

Material and Method

Material

The buffer material selected for this investigation was a laboratory-prepared mixture of sodium bentonite (Avonseal) and graded Indusmin sand (in equal proportion by dry weight). The detailed composition of the bentonite has been reported by Quigley (1984). The mixing solution used is "reference" synthetic granitic groundwater (GGW) according to a recipe given by Abry et al. (1982). The liquid limit of the Avonseal clay was 284.0% and the plastic limit was 40.7%, while the grain size distribution was 3% sand, 12% silt, and 85% clay. The specific proportions of the mixture were chosen because of their potentially attractive physical, chemical, and mechanical properties for the required performance criteria adopted by the Canadian Nuclear Fuel Waste Disposal Program Currently under Investigation by AECL Research.

Specimen Preparation

Specimens were prepared by mixing the above specified bentonite and sand material with GGW water to reach a water content of about 19%. Specimens were stored in a humid room for a period of one week to allow equilibration. To achieve a 1.67-Mg/m^3 uniform dry density, specimens were divided into five layers and a known quantity of wet material compacted statically in each layer. Thermocouples were placed inside the soil specimen after compaction at different positions along the length of the specimens. After the installation procedures, specimens were left for a period of 24 h to equilibrate. To check the uniformity of initial water content and dry density, one specimen was taken out and sectioned into nine portions before testing. It was found that the distributions of water content and dry density were uniform within 1%.

Following the above-described procedures, specimens were heated at one end by the heater to a constant temperature, and the perimeter of the specimens (i.e., the concrete section around the specimen) was cooled to a known constant temperature. Temperature measurements as a function of space and time were recorded during heating. Furthermore, tests were ended at different times and the specimens were sectioned into nine portions to determine the moisture distributions along its length.

Experimental Results

Preliminary Design

The test results of two series of experiments are described below. In the first series, Test No. 1 was evaluated at a 100°C elevated temperature and a heating time of 24 days. In the second series, Test Nos. 2, 3, and 4 were evaluated for the same boundary conditions but for different times at which moisture distributions were measured. Table 1 presents initial and boundary conditions for the two series conducted in the heat and moisture flow apparatus according to its preliminary design.

First Series

In the first series, only Test No. 1 was performed for a long period (24 days) to determine the maximum time required to establish the equilibrium moisture content distribution. The temperature profiles as a function of space and time are presented in Fig. 4 for a time period up to one day only. The temperature distributions from 1 day to 24 days are not shown in this figure. For time greater than one day, the temperature distribution profiles were positioned in a narrow band between the last two profiles. It can be seen from Fig. 4 that the temperature distributions stabilize very fast, in about 0.16 days. For water content determinations, specimens were taken from the center of the heated specimen using a sampler with 67.73 mm diameter and 87.00 mm lengths as shown in Fig. 6a. Specimens were then extruded from the sampler and sectioned into nine portions for volumetric water content determinations. The volumetric water content distribution after a period of 24 days, i.e., at the time the test stopped, is presented in Fig. 5. The volumetric water content is defined as the ratio between the volume of water and the volume of solids, V_s, water and air, V_a, i.e.,

$$\theta = \frac{V_w}{V_s + V_w + V_a}$$

Second Series

Test Nos. 2, 3, and 4 are included in the second series as shown in Table 1. The only difference between the various tests is the duration of time at which the water content distributions were measured. As an example for Test No. 2, the time at which the water content is measured is 2.397 days, i.e., at which time the test was stopped. In this group, only experimental data from Test No. 2 will be presented due to the similarity of the results.

The temperature distribution profiles at the center of Test No. 2 as a function of space and time are presented in Fig. 7. It can

TABLE 1—*Various test conditions conducted during the preliminary design*

Test Series	Test No.	Initial Conditions: Water Content, %	Initial Conditions: Volumetric Water Content	Initial Conditions: Dry Density, Mg/m³	Boundary Conditions: Heater Temperature, °C	Boundary Conditions: Cooler Temperature, °C	Test Duration: Test Duration, days
First	1	20 78	0.3033	1.46	100	15	24 000
Second	2	19 39	0 2753	1 42	100	15	2 397
	3	19.38	0 2769	1 43	100	15	4.995
	4	19.07	0 2721	1.43	100	15	11.970

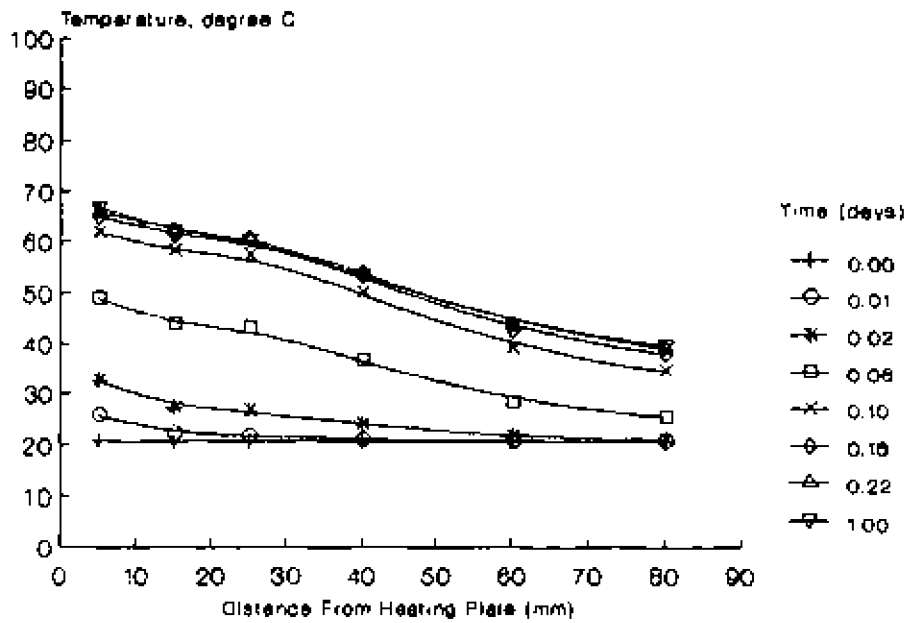

FIG 4—*Temperature distribution profiles for Test No. 1.*

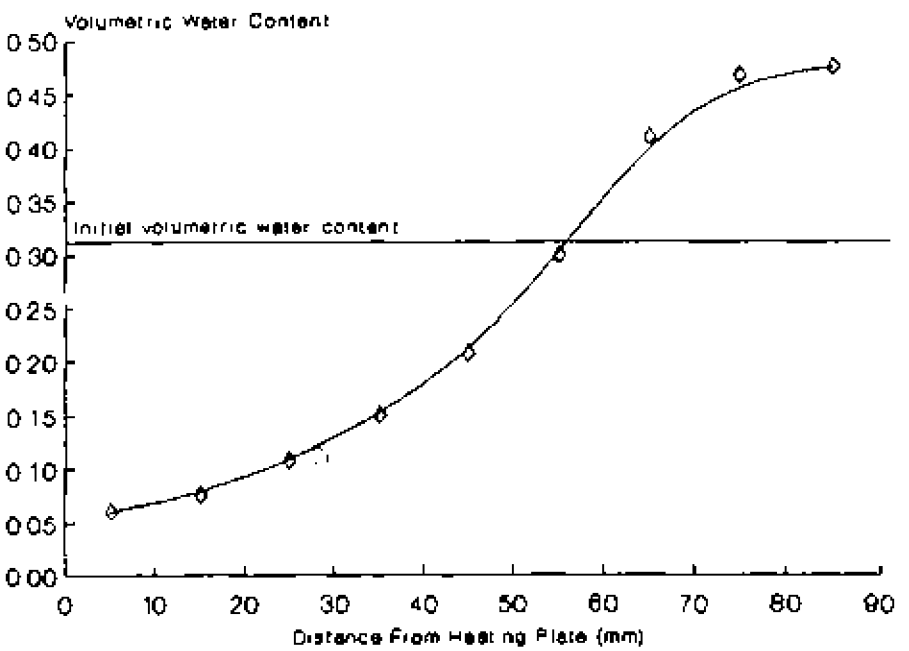

FIG. 5—*Volumetric water content distribution for Test No. 1.*

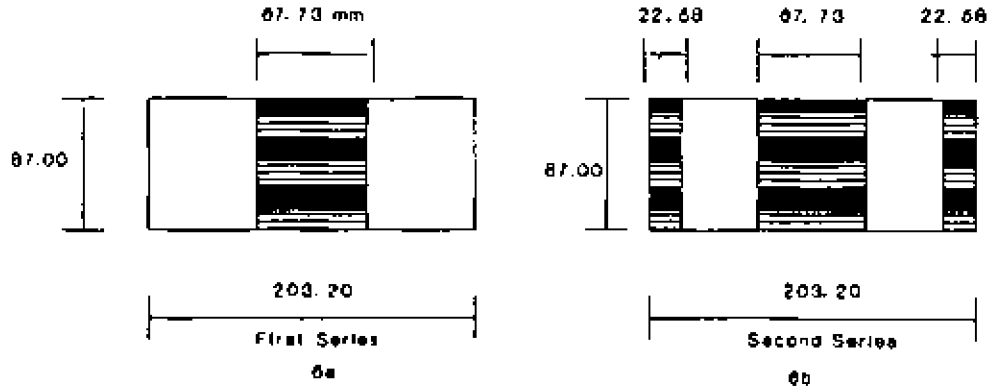

FIG. 6—*Sampling positions and sections for volumetric water content measurements after heating for both first and second series.*

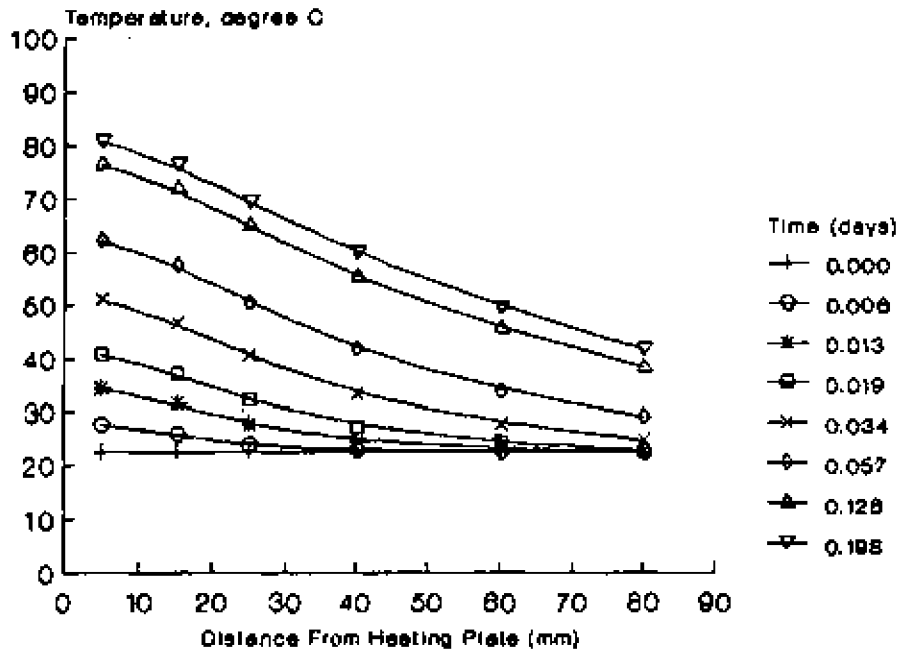

FIG. 7—*Temperature distribution profiles for Test No. 2*

be seen that the temperature distribution stabilizes in a period of 0.198 days, thus reaching a steady state condition. For time greater than 0.198 days, the temperature profiles were positioned in a narrow band between the last two profiles, i.e., for times 0.126 and 0.18 days. However, to highlight this type of temperature distributions, Fig. 8 presents the temperature distributions as a function of time for three positions of thermocouples along the length of the specimen. For example, at a distance of 5 mm from the heater the temperature rises up to 82.0°C after 0.313 days and drops to 74.0°C after 2.77 days. This relaxation in temperature commences after the water moves due to the imposed thermal gradient and can be attributed to the phase change of the water into vapor. Similar behavior is observed for the other two positions as shown in Fig. 8.

Furthermore, it can be seen from Fig. 7 that there is a difference of 20°C between the heating element and the closest soil layer to the heating element. This difference can be attributed to the radial flow of heat from the copper plate as well as from the soil specimen itself. To justify this statement, the temperature distributions in a vertical cross section inside the specimen at steady state condition are presented in Fig. 9. The contour lines of equal temperature are generated by the computer by inputting the temperature values for different positions inside and at the perimeter of the specimen. It seems that due to the cooling temperature, which is 15°C at the boundary, there is a gradient of temperature at the interface of the specimen with the heater, and hence the temperature distributes in a radial direction. At the same time there is another gradient of temperature in the longitudinal direction. This means that the temperature varied in two dimensions within the specimen.

Additionally, the temperature distribution is related to the volumetric water content distribution within the specimen, as shown in Fig. 10. From the volumetric water contents at different locations inside the specimen at locations given in Fig. 6*b*, con-

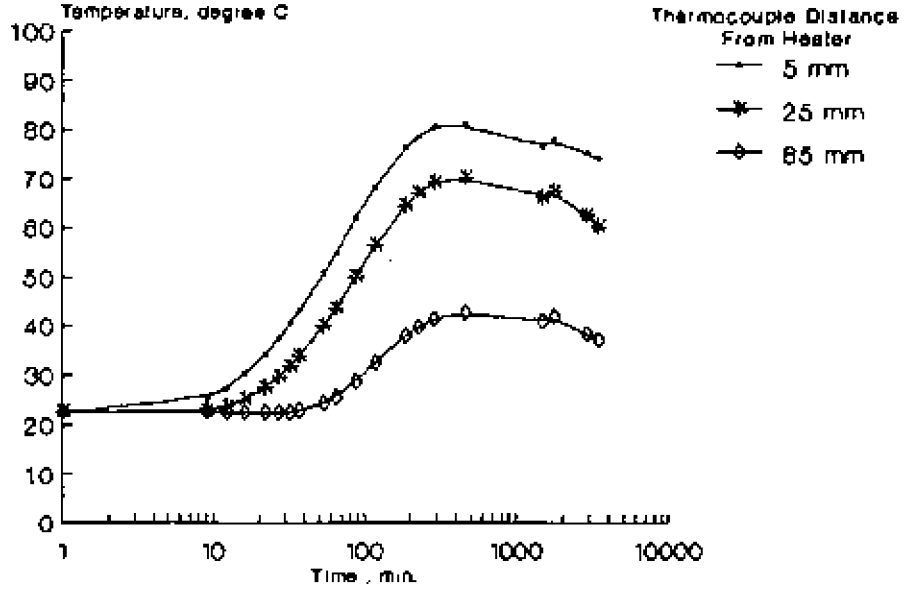

FIG. 8—*Variation of temperature with time for Test No. 2.*

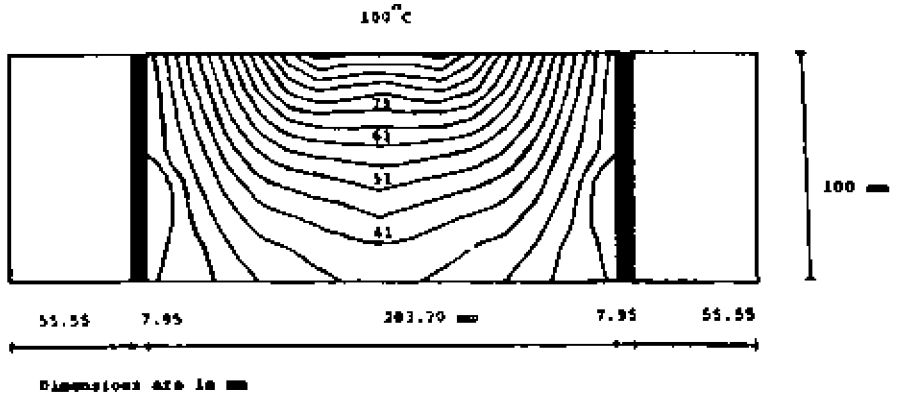

FIG. 9—*Temperature distribution for Test No. 2.*

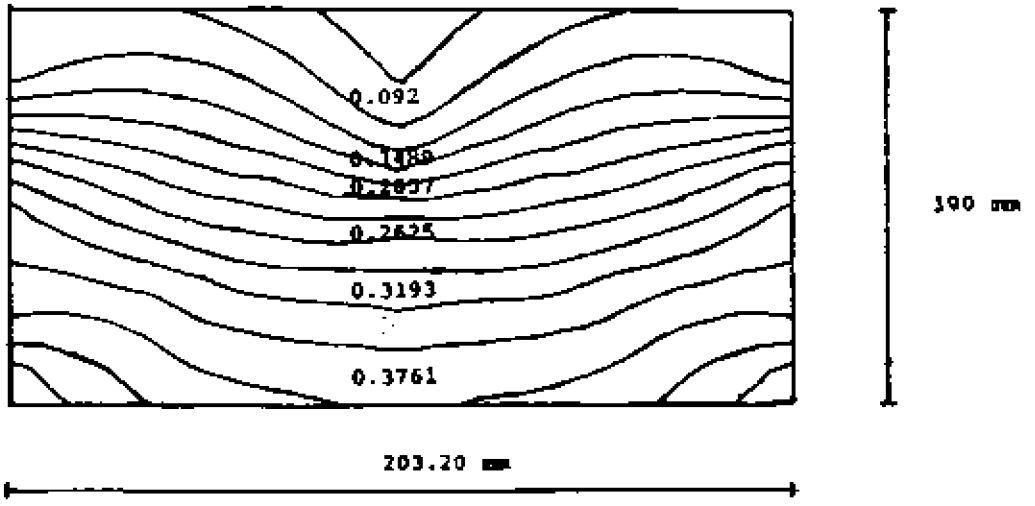

FIG. 10—*Volumetric water content distribution for Test No. 2*

tour lines were generated by computer to cover the area under investigation. The moisture moves away from the heater side to the other sides longitudinally and radially. The volumetric water content distribution is high towards the bottom and the perimeter of the specimen. When the test was stopped, a cone shape of dry material in the middle of the specimen was noticed. The base of the cone is in contact with the heater, and the apex of the cone lies in the longitudinal direction, which is perpendicular to the heater. According to test results, a total mass balance before and after heating was maintained.

It will be recalled that the preliminary design assumed that within the middle third of the specimen, measured in the radial direction, one-dimensional flow of heat and moisture in the longitudinal direction could be achieved. However, the previous discussion highlights the existence of a two-dimensional flow of both heat and moisture within the whole specimen. Examination of the temperature distribution in the middle third of the specimen (Fig. 9) highlights the nonuniformity of the temperature distribution at any cross section. A similar result can be concluded from the volumetric water content distribution presented in Fig. 10. This demonstrates that the condition of one dimensionality does not exist within the specimen even in the middle third. Therefore, a new specimen size was designed in order to achieve the one-dimensional flow of heat and moisture during a prolonged heating period. These changes will be addressed in the next section.

Modified Design

Before giving details of the modified design, it is appropriate to note that the length of the specimen could not be decreased due to the loss of useful measurements of temperature and volumetric water contents along the length of the specimen. The other alternative was to increase the diameter of the specimen. This would create a problem in handling the cell in terms of movement and compaction. To ensure one-dimensional heat flow, the radial boundary needs to be made as close to adiabatic as possible; this was achieved by placing a smaller diameter specimen within the original test apparatus and providing radial insulation.

A schematic diagram of the new specimen size is shown in Fig. 11. Specimen dimensions are 80.50 mm in diameter by 87.00 mm in length. The specimens are enclosed in a new, installed PVC tube measuring 80.50 mm and 94.70 mm in inner and outer diameters, respectively. The space between the new, installed and previously designed PVC tubes is filled with styrofoam to minimize radial heat flow.

Before engaging in a full spectrum of testing, the apparatus was checked for the following cases.

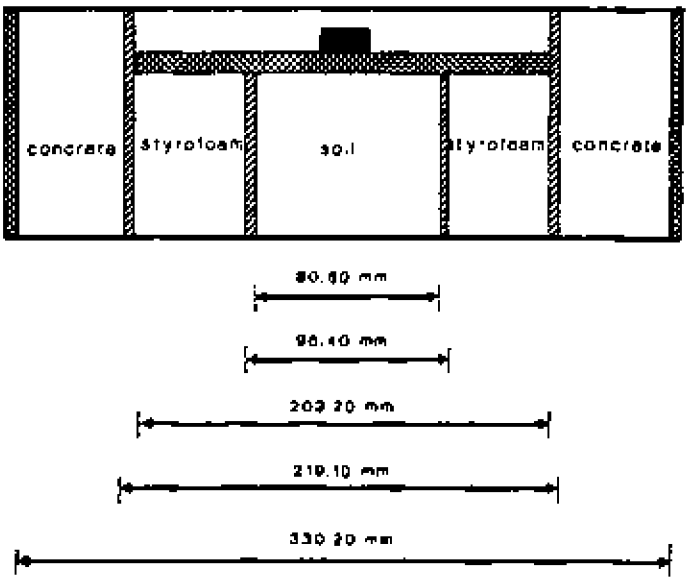

FIG. 11—*Schematic diagram illustrating the new specimen dimensions used in the third series*

Case 1: Cooling Temperature

Case 1 considers the effect of cooling temperature on the temperature distribution within the specimen. This can be achieved by conducting three experiments. Firstly, no cooling temperature is used during heating of the specimen; hence the temperature in the outer boundary of the apparatus is a direct response to the imposed boundary temperature by the heater as well as any radial temperature dissipation from the soil specimen. The initial and boundary conditions for Test No. 5, which represent this condition, are outlined in Table 2. The test results in terms of temperature distribution profiles are presented in Fig. 12. The temperature distribution profiles as a function of time and space within the specimen are shown in Fig. 12*a*. Temperature distributions at three different cross sections across the apparatus for heating time of 0.146 days are presented in Fig. 12*b*. From Fig. 12*a*, it can be seen that the temperature increases as a function of time for each position of thermocouple within the specimen as well as within the PVC adjacent to the concrete and the concrete itself. Temperature distributions show a tendency for equilibrium with the specimen after approximately 0.139 days. However, the temperature distributions within the outer PVC and concrete show a tendency for an increase in temperature with time. Therefore, for a longer period of heating time the temperature in the outer PVC as well as the concrete might be

TABLE 2—*Various test conditions conducted during the modified design*

		Initial Conditions			Boundary Conditions			
Test Series	Test No.	Water Content, %	Volumetric Water Content	Dry Density, Mg/m^3	Heater Temperature, °C	Cooler Temperature, °C	Description	Test Duration, days
Third	5	19.00	0.310	1.67	100	22	No cooling	0.416
Fourth	6	19.00	0.310	1.67	100	10	Cooling end plate only	0.416
Fifth	7	19.03	0.317	1.67	100	10	Cooling end plate and concrete	0.313
Sixth	8	19.00	0.31	1.67	100	10	Cooling end plate and concrete	0.300

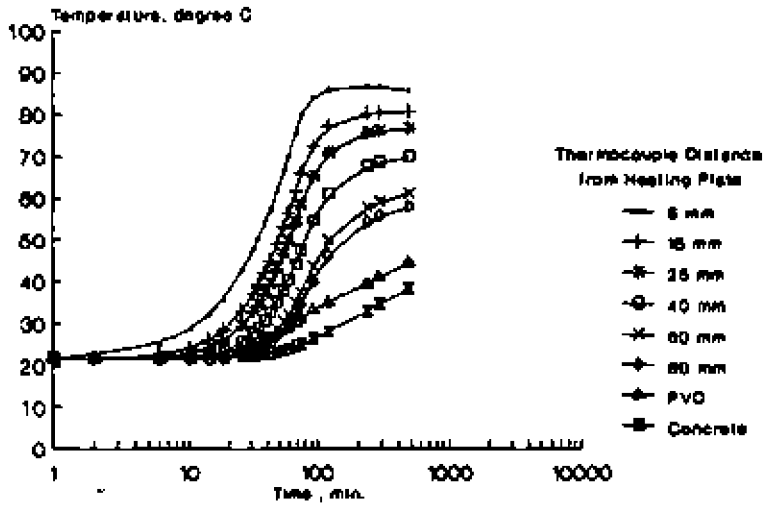

FIG. 12a—Temperature distribution profiles for Test No. 5.

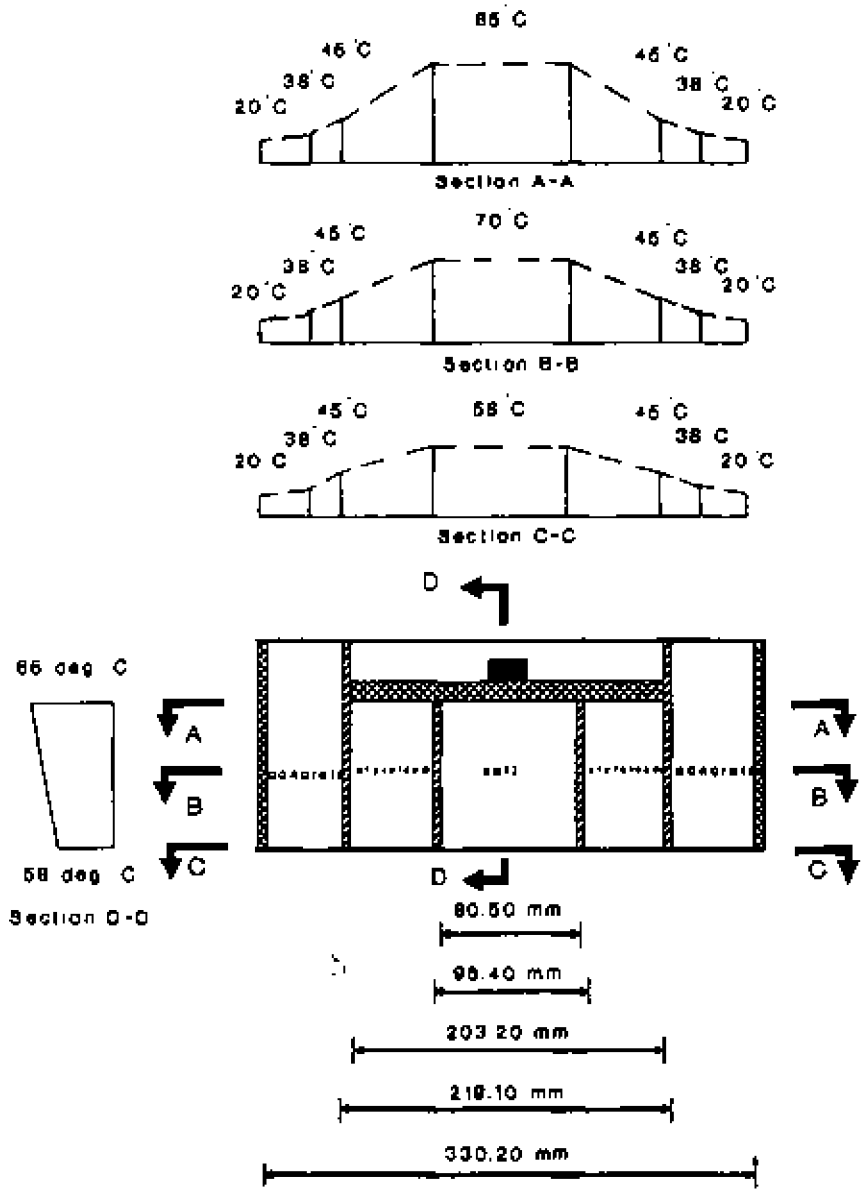

FIG. 12b—Temperature distribution across the apparatus after testing time = 0.416 days for Test No. 5.

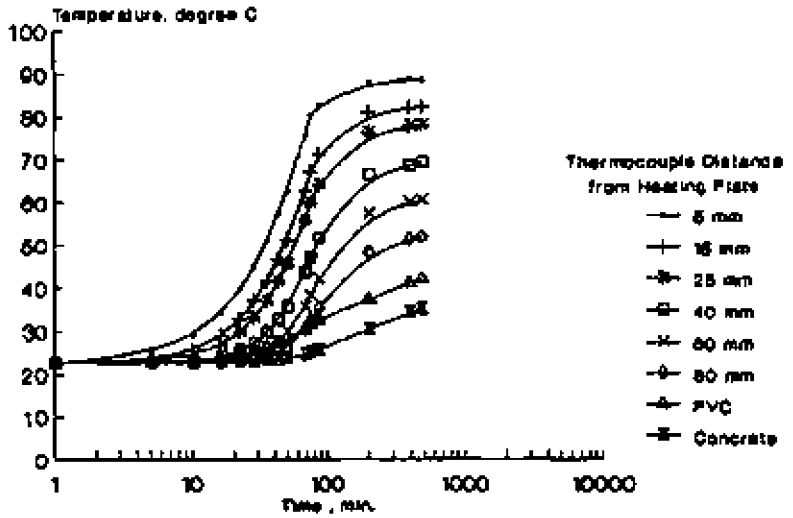

FIG. 13a—*Temperature distribution profiles for Test No. 6.*

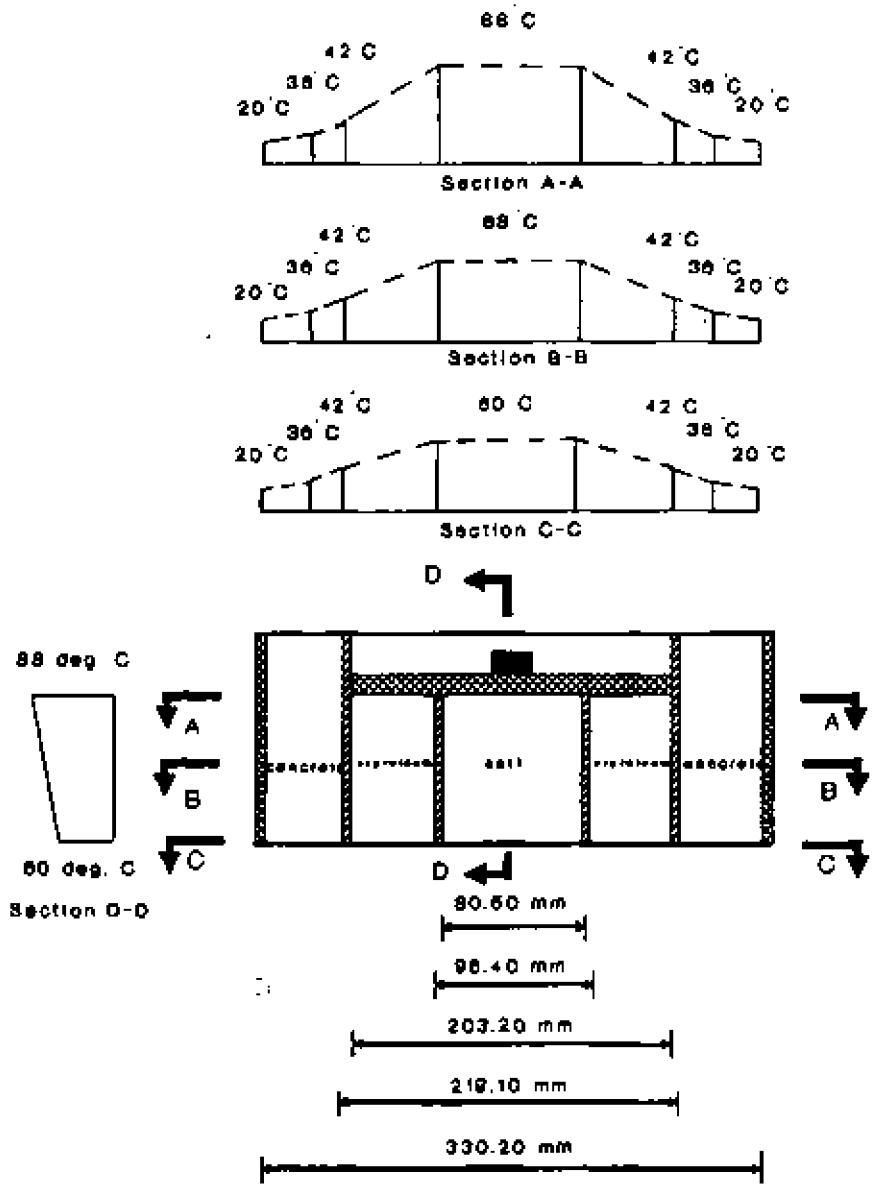

FIG. 13b—*Temperature distribution across the apparatus after heating time: 0.416 days for Test No. 6.*

increased to an equal or higher values than the temperature at some positions within the specimen. Hence, the boundary condition will not be controlled and the accurate modelling of heat and mass flow will be difficult to establish.

Furthermore, the temperature distributions at different cross sections shown in Fig. 12*b* demonstrate the existence of a temperature gradient across the apparatus in the radial direction. The real question can be stated as follows: Is there any radial gradient within the specimen or not? If there is a gradient in the radial direction within the specimen, one-dimensional flow of heat and moisture will not be achieved. Therefore, the temperature distribution within the specimen in the radial direction has to be measured. This will be discussed in a later section of this paper.

Secondly, cooling temperature is used only at the opposite end to the heater via circulation of cold water at a specified temperature on the bottom of the base aluminum plate (j—Fig. 1). Therefore, the boundary temperatures are constant at the extreme two ends of the specimen. The initial and boundary conditions for Test No. 6, which represents this condition, are outlined in Table 2. The test results in terms of temperature distribution profiles are presented in Fig. 13. The temperature distribution profiles as a function of space and time within the specimen are shown in Fig. 13*a*. Figure 13*b* gives the temperature distribution at four different cross sections across the apparatus for heating time equals 0.416 days. Similar results to Test No. 5 have been obtained except that the time required to reach equilibrium is longer than that required for Test No. 5 as shown from Figs. 12*a* and 13*a*. Also, one can note the difference in the shape of the temperature distribution profiles, i.e., temperature profiles for Test No. 5 are steeper than those for Test No. 6.

Thirdly, cooling temperature is used in the concrete section as well as in the opposite end plate to the heater. The heater temperature is set to 100°C, while the cooling temperature is set to 10°C. The initial and boundary conditions for Test No. 7, which represents this condition, are outlined in Table 2. The test results are shown in Fig. 14. The temperature distribution profiles as a function of space and time within the specimen are shown in Fig. 14*a*. Temperature distributions at four different cross sections across the apparatus for heating time equals 0.313 days are shown in Fig. 14*b*.

From these three different cases of boundary conditions, the preferred case is Case 7, where both the base plate and the concrete are temperature controlled and cooled. Cooling concrete increases the efficiency of the base plate heat sink and also provides controlled testing boundaries. Although the radial temperature gradients are higher, the efficiency of the insulation is such to sufficiently retard radial heat flow, thus giving one-dimensional conditions.

In order to fully ensure one-dimensional flow of heat in the longitudinal direction within the specimen, one last check for the uniformity of the temperature distribution in the radial direction at any position within the specimen has to be executed. This situation will be discussed in the next section.

Case 2: Radial Temperature Distribution

As discussed above, in order to ensure a uniform temperature distribution at any cross section, Test No. 8 was conducted. The initial and boundary conditions for Test No. 8 are shown in Table 2. Three cross sections are used to measure the temperature distributions within the specimen as a function of time. Each cross section has two thermocouples; Nos. 6 and 1 are placed at 5.0 mm from the heating plate, while thermocouple Nos. 5 and 3 are placed at 82.0 mm from the heating plate. Thermocouples Nos. 4 and 2 are placed approximately at the middle of the specimen, i.e., at 42 mm from the heating end. The heating plate was set to 100°C and the cooling system to 10°C at the start of the test. These boundary conditions are exactly the same as those of Test No. 7. Temperatures are measured as a function of time for all the inserted thermocouples. It can be seen from Fig. 15 that the temperature distribution at any radial cross section is uniform as a function of time. Hence, there is no temperature gradient within the specimen in the radial direction.

The above discussion of Case Nos. 1 and 2 demonstrates the importance of the use of a heat sink to extract the heat from the apparatus as well as to control the temperature gradients within the specimen and its surrounding components with insulation.

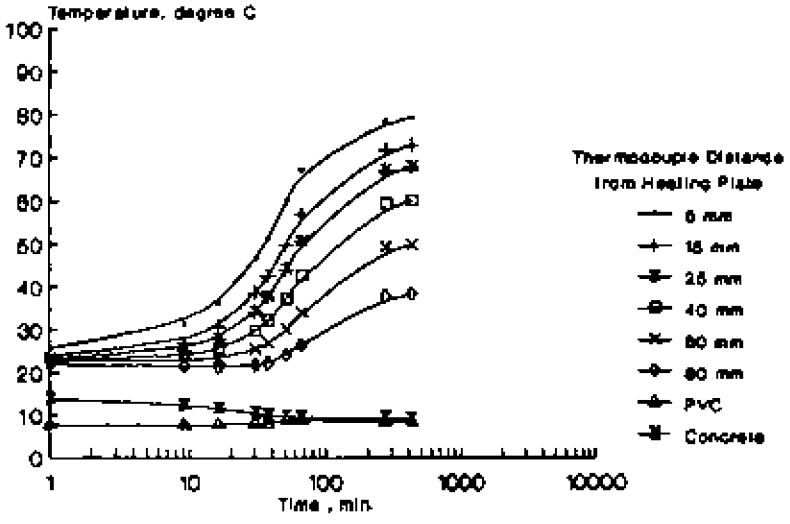

FIG. 14*a*—*Temperature distribution profiles for Test No. 7*

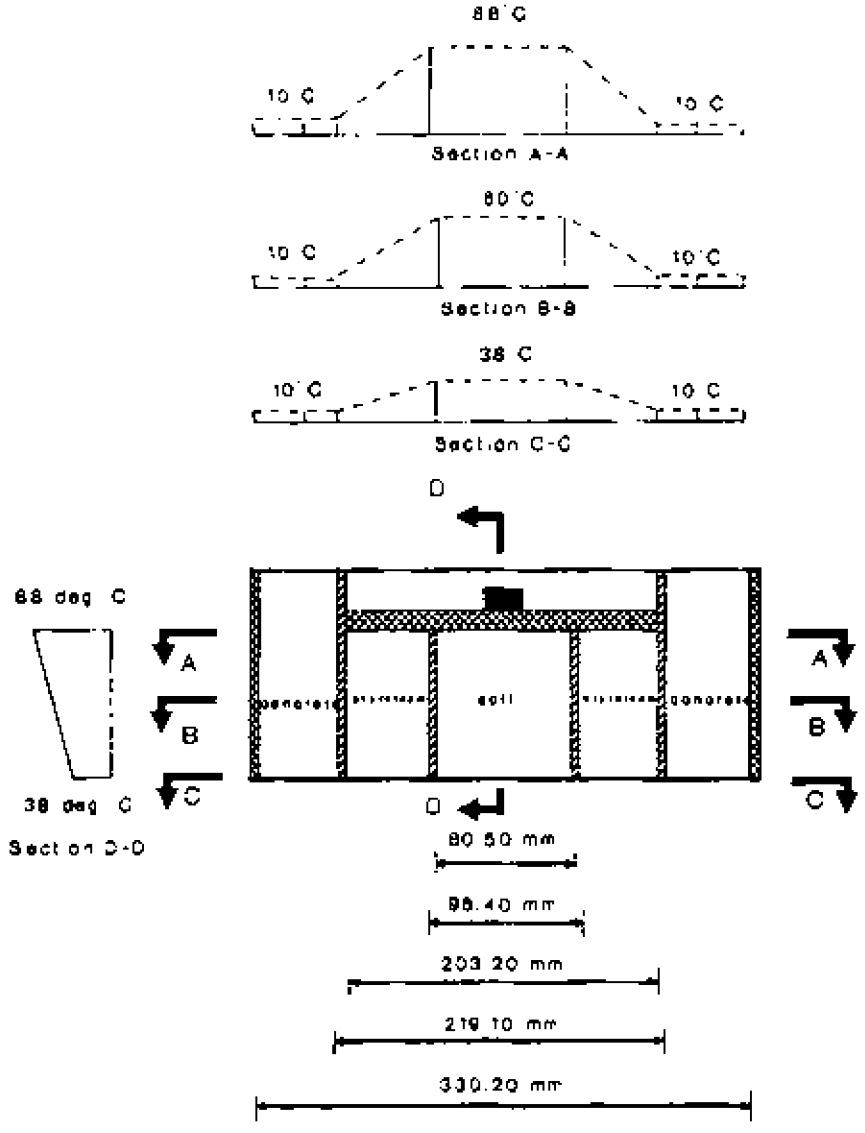

FIG. 14b—Temperature distribution across the apparatus after heating time = 0.313 days for Test No. 7

Furthermore, uniformity of temperature distribution in the radial direction within the specimen proves the existence of one-dimensional flow of heat in the longitudinal direction. Therefore, the modified design for heat and mass flow apparatus demonstrates the potential use of this apparatus to study the coupled thermal and moisture flow in buffer material. The next section addresses the performance of buffer material due to imposed temperature gradient as an example of the experimental data that can be obtained from this new designed apparatus.

Temperature and Moisture Distributions

In the final series of the experiment, Test Nos. 9, 10, 11, and 12 are included. The initial and boundary conditions for the seventh series are presented in Table 3. The only difference between the tests in this series is the time at which the tests are stopped and specimens sectioned for volumetric water content measurements. Test No. 11 was stopped immediately after the temperature distribution reached equilibrium, and specimens were sectioned into nine portions for volumetric water content measurement. Each portion was 80.5 mm in diameter by 9.7 mm in thickness. At that time one could not measure a noticeable variation in volumetric water content distribution due to the time required to: (1) remove the specimen from the mould, (2) cut the specimen into nine portions, and (3) take measurements. Visual inspection of the section after cutting for volumetric water content measurement indicates that the water content was uniformly distributed in the radial direction. This is expected due to the uniformity of temperature in the radial direction at any cross section. Therefore, the time at which the water content was first measured was increased to 0.294 days.

Due to the similarity of temperature distributions as a function of space and time for all the experiments in the third series, temperature distribution profiles are presented only for Test No. 9. Figure 16 presents the temperature distribution profiles for Test No. 9 for various time intervals. Figure 16 indicates that the difference between the heating element and the soil layer is completely eliminated, which indicates that there is no radial

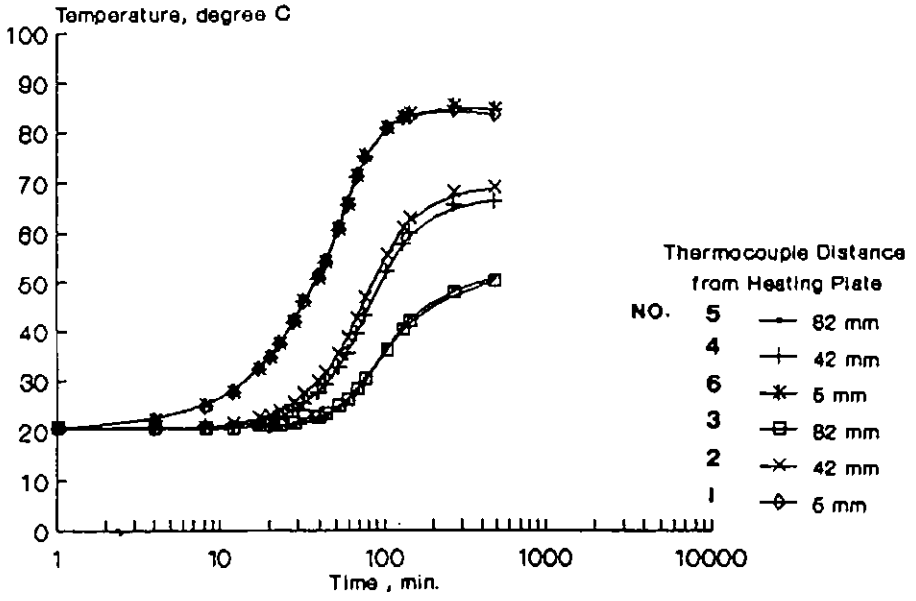

FIG. 15—*Temperature distribution profiles for Test No. 8.*

TABLE 3—*Various test conditions conducted to study temperature and moisture distributions.*

Test Series	Test No.	Initial Conditions: Water Content, %	Initial Conditions: Volumetric Water Content	Initial Conditions: Dry Density, Mg/m³	Boundary Conditions: Heater Temperature, °C	Boundary Conditions: Cooler Temperature, °C	Test Duration, days
Seventh	9	18.42	0.3076	1.67	100	10	0.985
	10	18.96	0.3166	1.67	100	10	2.792
	11	18.84	0.3146	1.67	100	10	0.083
	12	19.03	0.3178	1.67	100	10	0.294

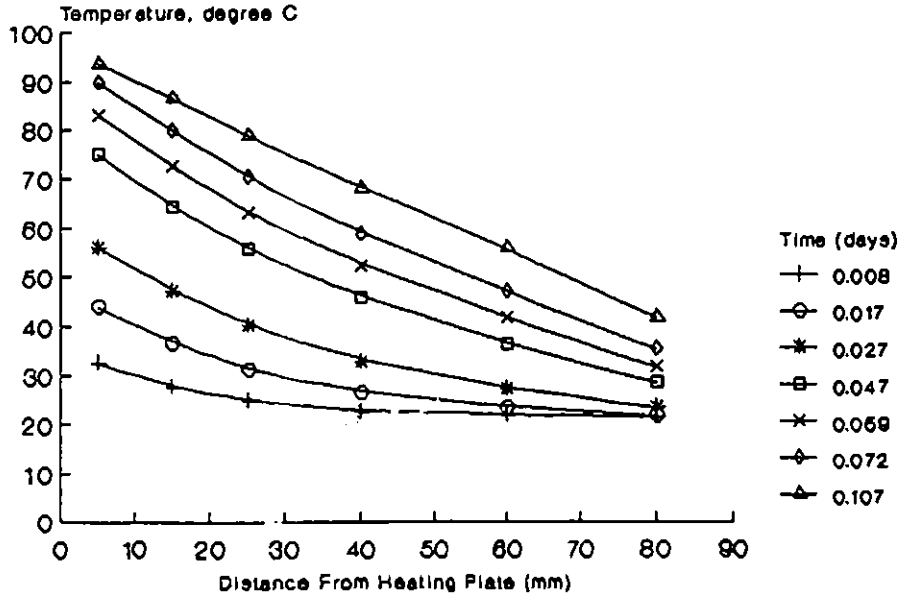

FIG. 16—*Temperature distribution profile for Test No. 9.*

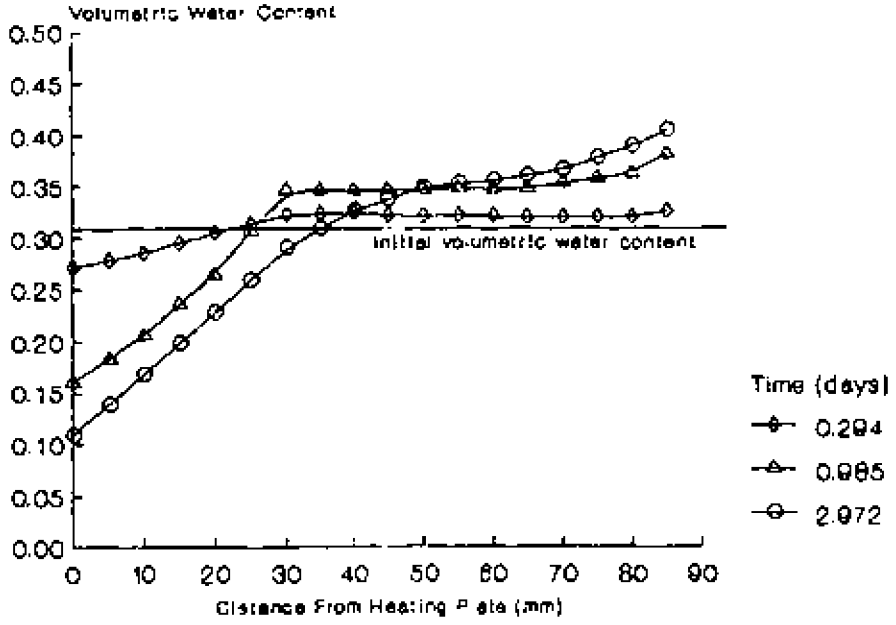

FIG. 17—*Volumetric water content distributions for Test Nos. 8, 10, and 12.*

flow of heat and hence uniform moisture distribution in the radial direction as discussed in the sixth series, i.e., Test No. 8. Temperature reached a steady state condition after 0.107 days.

Figure 17 presents the volumetric water content distribution along the longitudinal direction of the specimen for Test Nos. 9, 10, and 12. The volumetric water content reduces at the hot end due to the induced heat flux at this boundary and moves from the hot end along the longitudinal direction. The first measurable profile is achieved after 0.294 days. After approximately three days, the volumetric water content reduced at the heater side to 11%, while at the cold end it increased to 40%. All the experiments in the seventh series show a mass balance as shown in Fig. 17.

Conclusions

A coupled heat and water flow apparatus, in which a specimen is confined between top and bottom aluminum end plates and a perimeter consisting of a PVC liner, concrete, and steel, offers a means by which to study the performance of buffer under thermal and isothermal conditions.

In the preliminary design of the apparatus, one-dimensional flow of heat and moisture was not achieved. In spite of the specimens' diameter-length ratio of 2, radial flow of heat and moisture was demonstrated by the experimental data.

In the modified design, a new ratio between the specimen's diameter and length was designed to be equal to 0.92. More effective insulation between the new side of the specimen and the old perimeter was included in the new apparatus. The third, fourth, and fifth test series, i.e., test Nos. 5, 6, and 7, demonstrate the usefulness of the cooling system and properly designed insulation to control the temperature gradients and to ensure the existence of one-dimensional flow. Test series No. 6 demonstrates the uniformity of temperature and volumetric water content distribution at any cross section in the radial direction within the specimen. Good quality data for temperature and volumetric water content distributions were obtained.

The temperature distribution stabilizes very rapidly after a period of approximately 0.107 days. The moisture moves away from the hot end along the longitudinal direction of the specimen due to the imposed thermal gradient. A good quality measurement of volumetric water content was achieved after a period of 0.294 days. Additionally, total mass balance was achieved during the heating period, which indicates that there is no moisture loss due to evaporation.

The temperature distributions as well as volumetric water content distributions as a function of space and time are very important input data in order to calculate the diffusion parameters as a function of temperature and volumetric water content as demonstrated by Yong and Xu (1988), Yong et al. (1990), and Mohamed, et al. (1990). Future studies will address the calculation of the diffusion parameters and calibrate the different models which predict the flow of heat and moisture in unsaturated swelling buffer material.

Acknowledgment

This study was financially supported by the Canadian Nuclear Fuel Waste Management Program, which is jointly funded by Atomic Energy of Canada Limited (AECL) and Ontario Hydro under the auspices of the CANDU owners group.

References

Abry, D. R. M., Abry, R. G. F., Tickner, K. V., and Vandergraaf, T. T., 1982, "Procedure to Determine Sorption Coefficients of Radionuclides on Rock Coupons under Static Conditions," Technical Record TR-189, Atomic Energy of Canada Limited, Pinawa, Manitoba.

Cassel, D. K., Nielsen, D. R., and Biggar, J. W., 1969, "Soil-Water Movement in Response to Imposed Temperature Gradients," *Soil Science*, Vol. 33, pp. 493-500.

Cheung, S. C. H., Gray, M. N., and Dixon, D. A., 1987, "Hydraulic and Ionic Diffusion Properties of Bentonite/Sand Buffer Materials," *Proceedings*, International Symposium on Coupled Processes Affecting the Performance of a Nuclear Waste Repository, Berkeley, CA, pp. 393–407.

Cheung, S. C. H. and Gray, M. N., 1990, "Coupled Flow of Heat and Mass in Clay Materials and Is Significance to Barrier Performance," 1990, Annual Conference, Canadian Society of Civil Engineering, Hamilton, Ontario, pp. 18–27.

Gray, M. N. and Cheung, S. C. H., 1986, "Disposal Vault Sealing," Technical Record, TR-375, Atomic Energy of Canada Limited, Pinawa, Manitoba, pp. 235–263.

Hancox, W. T., 1986, "Progress in the Canadian Nuclear Fuel Waste Management Program," Canadian Nuclear Society International Conference on Radioactive Waste Management, Winnipeg, Manitoba, pp. 1–9.

Mohamed, A. M. O., Xu, D. M., Yong, R. N., and Cheung, S. C. H., 1990, "Application of an Identification Technique to Evaluate Diffusion Parameters in a Coupled Flow," *Proceedings*, IASTED International Symposium on Modelling, Simulation and Optimization, Montreal, Canada, Z. Jacyno, Ed, pp. 103–105.

Nielsen, D. R., Jackson, R. D., Cary, J. W., and Evans, D. D., 1972, "Soil Water," American Society of Agronomy and Soil Science Society of America, Madison, WI.

Philip, J. R. and de Vries, D. A., 1957, "Moisture Movement in Porous Materials under Temperature Gradients," *Transactions of the American Geophysical Union*, Vol. 38, p. 222–232.

Pusch, R., Borgesson, L., and Ramqvist, G., 1985, "Final Report of the Buffer Mass Test, Vol. 2: Test Results. Stripa Project," KBS-Sp-85-12. Swedish Nuclear Fuel and Waste Management Co., Stockholm, Sweden.

Quigley, R. M., 1984, "Quantitative Mineralogy and Preliminary Pore-Water Chemistry of Candidate Buffer and Backfill Materials for Nuclear Waste Disposal Vault," Report AECL-7827, Atomic Energy of Canada Limited, Pinawa, Manitoba.

Smith, W. O., 1943, "Thermal Transfer of Moisture in Soils," *Transactions of the American Geophysics Union*, Vol. 24, pp. 511–523.

Taylor, S. A. and Cary, J. W., 1960, "Analysis of the Simultaneous Flow of Water and Heat or Electricity with the Thermodynamics of Irreversible Processes," *Seventh International Congress of Soil Science Transactions*, Vol. 1, pp. 80–90.

Yong, R. N., Boonsinsuk, P., and Wong, G., 1986, "Formulation of Backfill Material for a Nuclear Fuel Waste Disposal Vault," *Canadian Geotechnical Journal*, Vol. 23, pp. 216–228.

Yong, R. N. and Xu, D., 1988, "An Identification Technique for Evaluation of Phenomenological Coefficients in Coupled Flow in Unsaturated Soils," *International Journal for Numerical and Analytical Methods in Geomechanics*, Vol. 12, p. 283–299.

Yong, R. N., Mohamed, A. M. O., and Cheung, S. C. H., 1989, "Thermal Performance of Backfill Material for a Nuclear Fuel Waste Disposal Vault," Symposium, Scientific Basis for Nuclear Fuel Waste Management, *Material Research Society*, Vol. 176, pp. 649–656.

Yong, R. N., Mohamed, A. M. O., and Xu, D. M., 1990, "Coupled Heat-mass Transport Effects on Moisture Redistribution Prediction in Clay Barriers," *Engineering Geology*, Vol. 28, pp. 315–324.

Abdel-Mohsen O. Mohamed,[1] Raymond N. Yong,[2] and Steven C. H. Cheung[3]

Authorized Reprint 1992 from Geotechnical Testing Journal, December 1992

Temperature Dependence of Soil Water Potential

REFERENCE: Mohamed, A. M. O., Yong, R. N., and Cheung, S. C. H., "Temperature Dependence of Soil Water Potential," *Geotechnical Testing Journal*, GTJODJ, Vol. 15, No. 4, December 1992, pp. 330–339.

ABSTRACT: To understand the process of coupled heat and water transport, the relationship between temperature and soil water potential must be known. Two clays, Avonlea bentonite and Lake Agassiz clay, are being considered as the clay-based sealing materials for the Canadian nuclear fuel waste disposal vault. Avonlea bentonite is distinguished from Lake Agassiz clay by its high sealing potential in water. A series of experiments was performed in which the two clays were mixed with equal amounts of sand and were compacted to a dry density of 1.67 Mg/m³ under various moisture contents and temperatures. A psychrometer was placed within the compacted clay-sand to measure the soil water potential based on the electromotive force measured by the psychrometer. The results indicate that the soil water potential at a particular temperature is higher for both clay-sand mixtures than predicted by the change in the surface tension of water; this effect is much more prominent in the Avonlea bentonite and at low moisture contents. The paper presents empirical equations relating the soil water potential with the moisture content and temperature of the two clay-sand mixtures.

KEYWORDS: temperature, soils, soil water potential, volumetric water content, unsaturated, swelling, surface tension, diffused double layer, nuclear water management

The safe and permanent disposal of radioactive waste requires that a number of diverse chemical elements be isolated from the environment for a long time. The concept of emplacing the waste in a vault excavated in the plutonic rock of the Canadian Shield at a depth of 500 to 1000 m below the surface is being evaluated as part of the Canadian Nuclear Fuel Waste Management Program. In addition to the naturally low-permeability rock, a number of engineered barriers such as the corrosion-resistant container, the buffered waste containers, and the backfill in both drift and shaft are used to limit the release of radionuclides from the solidified waste, as shown in Fig. 1. The corrosion resistant containers will be placed in boreholes drilled into the floors of the emplacement rooms and separated from the host rock by a buffer material. The remainder of the vault will be filled with an earthern clay-based backfill.

[1]Research associate, Geotechnical Research Centre, adjunct professor, Civil Engineering Department, McGill University, 817, Sherbrooke St. West, Montreal, PQ, H3A 2K6.

[2]William Scott professor, Civil Engineering Department, director, Geotechnical Research Centre, McGill University, 817, Sherbrooke St. West, Montreal, PQ, H3A 2K6.

[3]Soil scientist, AECL Research, Whiteshell Laboratories, Pinawa, MB, ROE 1L0. Current address: Concordia University, 1455 de Maisonneuve Blvd. West, Montreal, PQ, H3G 1M8.

The buffer and backfill will be compacted clay-based materials with low ionic and hydraulic diffusivities (Cheung et al. 1985; Mohamed et al. 1990). The mineral compositions and engineering properties of the buffer and backfill were reported by Gray and Cheung (1986) and by Yong et al. (1986). The hydraulic pressure, temperature, and solute concentrations in the pore water vary spatially and temporally in the clay and barrier materials. A multi-flow of heat, water, and dissolved solids, including radionuclides released from breached containers, is expected in the clay barriers under changing driving conditions (Cheung and Gray 1990; Mohamed et al. 1990).

The Philip-de Vries model (Philip and de Vries 1957) is generally used to predict the movement of moisture under non-isothermal conditions. The change in soil water potential with temperature for a given water content is attributed solely to the effects of temperature on the surface tensions of the water (Wilkinson and Klute 1962, Gardner 1965; Haridasan and Jensen 1972, Yong et al. 1969; Nimmo 1983). These workers also suggested that the temperature coefficient of the soil water potential increases because of the presence of solute in the soil solution, which changes the temperature coefficient of the water's surface tension and the presence of entrapped air. A number of investigators (Constantz 1983, Ploeker et al. 1968) studied the temperature dependence of the soil water potential. They concluded that, (1) for coarse soil, the dependence is about as strong as expected from the surface tension hypothesis; (2) for the fine-grained soil, the dependence is significantly stronger; and (3) the temperature dependence increases with the dryness of the soil. The investigation of the temperature dependence was not extended to include wide ranges of temperature or moisture content or the effect of swelling soils such as bentonite clay. Peck (1960), Chahal (1964, 1965), de Backer (1967), and Cary (1967) investigated the influence of entrapped air on the temperature coefficient of the soil water potential.

This study is designed to examine the effects of temperature on soil water potential for the clay-based sealing materials being proposed for the Canadian nuclear fuel waste disposal vault. Two clays, Avonlea bentonite and Lake Agassiz clay, are being considered for the buffer and backfill material. Avonlea bentonite is distinguished from Lake Agassiz clay by its high surface area and high swelling potential in water. In a series of experiments, the two clays were mixed with sand and were then compacted to a dry density of 1.67 Mg/m³ under various moisture contents and temperatures. A psychrometer was placed within the compacted clay to determine the soil water potential based on the electromotive force measured by the psychrometer using an equation derived on the basis of psychrometric principles and

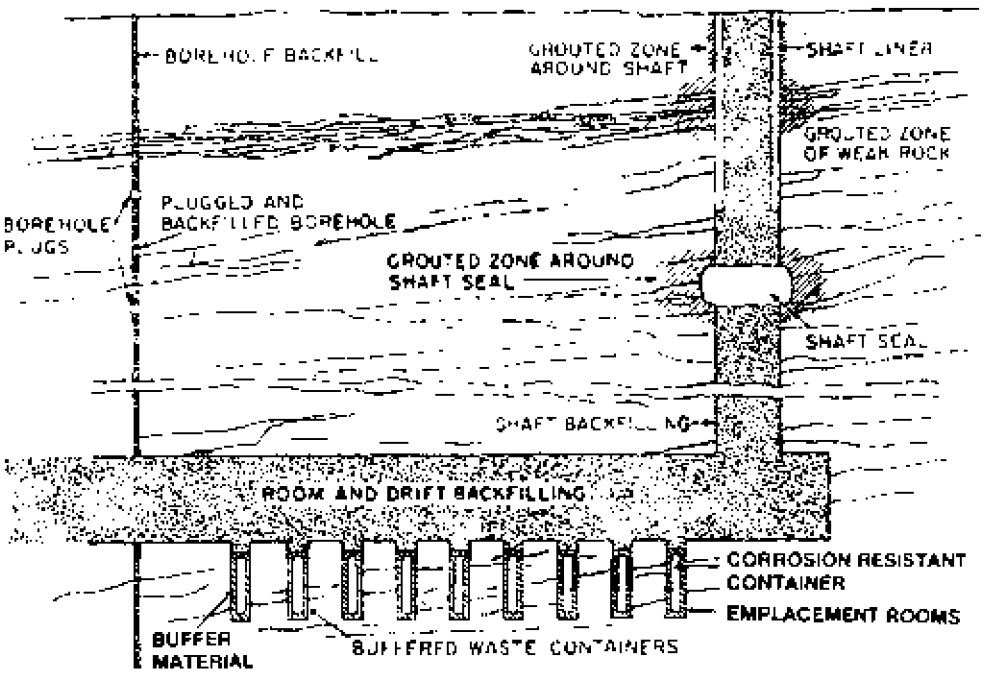

FIG. 1—*Engineered barriers and components of a nuclear fuel waste disposal vault*

equilibrium thermodynamics. The empirical equations relating the soil water potential with the moisture content and temperature of the two clay-sand mixtures are presented. The soil water potential calculated from experimental data and from the surface tension effect (the Philip-de Vries model) is compared for the two clay sand mixtures.

Description of Test Facility

Testing Cell

The following criteria were considered in the design of the water potential cell test equipment.

1. The unsaturated clay soil specimen is completely sealed in thick Teflon to prevent evaporation of water or escape of air.
2. A large mass of clay material is required to cover the entire chamber wall of the psychrometer. This eliminates any temperature differences between the chamber and the reference junction, and also minimizes the error associated with the heating of air (i.e., a decrease in relative humidity arising from the increased capacity of the air to hold water vapor).

The test equipment shown schematically in Fig. 2 was designed to meet these criteria. Basically, the unsaturated clay specimen is statically compacted at a specified water content and constant dry density. The specimen is surrounded by a rigid Teflon liner so that any volume change in the soil specimen is negligible during testing. The specimen and the Teflon liner are enclosed within cast iron to assure further rigid support.

Psychrometer

The psychrometer used to measure the soil water potential consists of a specimen chamber where the drop in the wet-bulb temperature can be measured (Fig. 3). Usually this wet bulb is

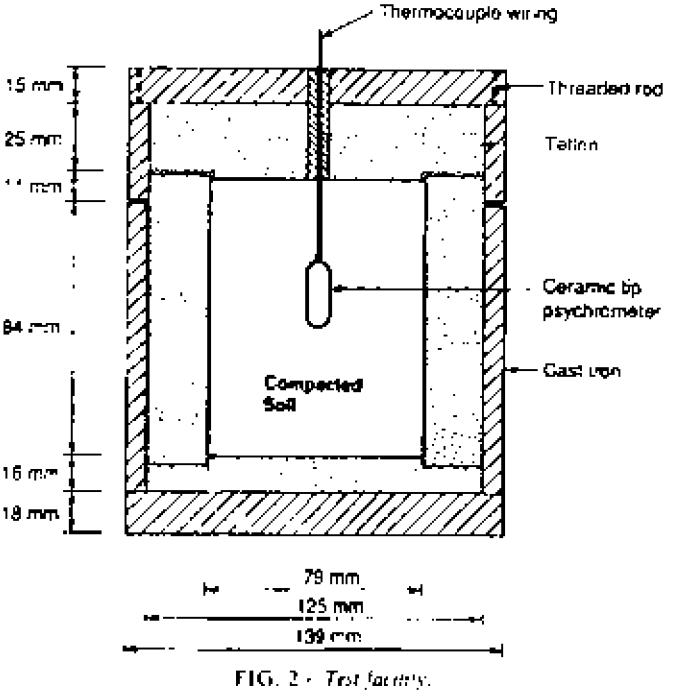

FIG. 2—*Test facility.*

one junction of the thermocouple with the reference junction at the specimen chamber wall. The water potential of a specimen is calculated from the temperature difference between these two junctions given by the thermocouple electromotive force (EMF).

A thermocouple measurement is based on a difference in resistances, which represent the difference between the junction temperature at the head of the psychrometer test chamber where the chromel and constantan wires are fastened to the connecting pins. The offset reading, obtained after initialization, should be less than 3 μV for a meaningful measurement, as specified by

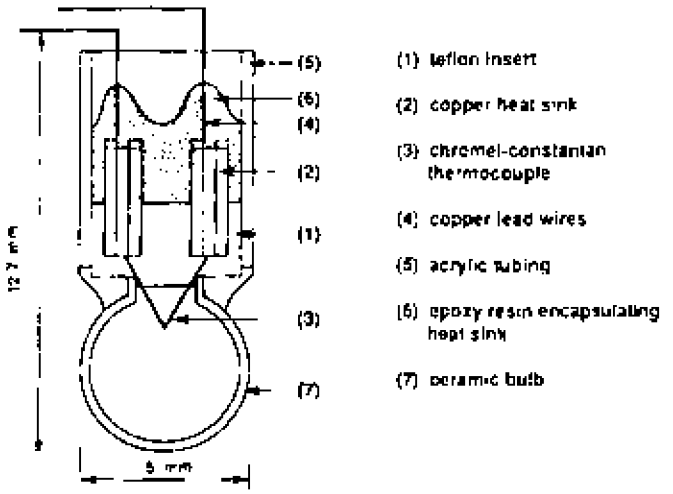

FIG. 3—*Cross section of a thermocouple psychrometer for soil water potential measurements.*

the reference manual provided by the manufacturer. Higher offset readings are evidence of excessive thermal gradients. Therefore, soil water potentials for temperatures above 47 and 67°C could not be measured for the Lake Agassiz clay/sand mixture and the sodium bentonite/sand mixtures specimens, respectively. This is determined based on the increase in the offset readings, which indicated excessive thermal gradients and hence an error in the measurements.

Psychrometer Microvoltmeter

The PR-55 psychrometer microvoltmeter is a control unit and read-out device used with the Peltier cooled-thermocouple psychrometer to measure the thermocouple electromotive force (EMF). Two modes of operation are provided: the PR-55 may be operated manually or in a semiautomatic mode. The PR-55 measures temperature, zero offset, and the psychrometric plateau. Ten sensors may be connected at one time. A single switch selects the sensor to be used. The sensors are connected to the microvoltmeter with surefast connectors and receptacles. A digital display indicates the voltage from −100 to +100 μV in the 100-μV position and voltages from −1000 to +1000 μV in the 1000-μV position.

Experimental Procedure

Material

The material selected for this investigation was a laboratory mixture of: (1) Lake Agassiz clay and graded indusmin silica sand (called Type 1 clay), and (2) sodium bentonite (Avonseal) and graded indusmin silica sand (called Type 2 clay). Yong et al. (1986) and Gray and Cheung (1986) described a study on the general composition of these two types of clay. These clay-sand materials were considered because of their physical, chemical, mechanical, and engineering properties for the required performance criteria adopted for the Canadian Nuclear Fuel Waste Disposal Program (Lopez 1984, Cheung et al. 1991, Xu et al. 1991). The material properties of the clays used in this study are shown in Table 1.

A specific clay-sand mixture involving an equal amount of clay and sand was selected for this study. The mixture, using both Type 1 and Type 2 clay, was then statically compacted to a dry density of 1.67 Mg/m³ with various amounts of a mixing solution of a "reference" synthetic granitic ground water (GGW) with a recipe given by Abry et al. (1982). The specific proportion of sand and the dry density were adopted for the reference buffer material using sodium bentonite. Lake Agassiz clay was used to highlight the differences of soil water potential between a low swelling and a high swelling clay (Avonseal).

TABLE 1—*Material properties.*

Parameter	Silica Sand	Lake Agassiz Clay	Sodium Bentonite
Grain Size			
Sand %	89	0	1
Silt (20 to 2 μm) %	11	39	39
Clay (< 2 μm) %	0	61	60
Consistency Limits			
Liquid limit %	NA	111.5	290
Plastic limit %	NA	30.8	200
Mineralogy (in decreasing order)		Montmorillonite, illite, quartz, kaolinite, feldspar	Montmorillonite, kaolinite, quartz, feldspar, illite
Specific Gravity	2.65	2.79	2.75
Surface Area, m²/g		239	615
Chemical Analysis			
Soluble Cations, meq/L			
Na^+		5.2	19.3
K^+		0.57	2.10
Ca^{2+}		3.90	1.70
Mg^{2+}			0.40
Extractable Cations meq/100 g			
Na^+		4.57	53.7
K^+		2.33	1.4
Ca^{2+}		62.12	17.9
Mg^{2+}			5.1

Sample Preparation

Specimens were prepared by mixing the material specified above with different amounts of GGW to achieve a different initial moisture content for each specimen. Specimens were stored in a humid room for a period of 24 h before testing. To achieve a constant dry density (1.67 Mg/m³), the prepared specimens were divided into five layers, and a known quantity of wet material was compacted statically in each layer. After compaction, a small hole was drilled into the middle of the specimen to allow the psychrometer to be inserted.

Test Procedure

A period of 24 h was allowed for equilibration with the psychrometer before any reading. After the first reading of the thermocouple electromotive force (EMF), specimens were placed in a temperature-controlled oven, and the temperature was raised to a specified value. A reading was taken 24 h after each subsequent temperature increase. In general, a cooling period of at least 30 s was needed for the thermocouple to produce a stable reading. The number and conditions of experiments conducted in this study program are shown in Table 2.

Calculation of Soil Water Potential

Appendix outlines the procedure for deriving the relationship between soil water potential and the measured electromotive force, E, from the psychrometer. The equation is derived on the basis of the psychrometer operating principles and equilibrium thermodynamics. The relationship is

$$\psi = -35.545 \frac{E}{T} \qquad (1)$$

where

ψ = soil water potential in MPa,
E = electromotive force in μV, and
T = soil temperature in K.

The soil water potential is calculated as shown in Fig. 4 for different values of electromotive force and temperature. When the temperature is kept constant, the soil water potential increases (i.e., becomes more negative) and the electromotive force increases. The relationship between the soil water potential and the electromotive force is linear, and the slope of the line decreases with an increase in temperature. Furthermore, either Eq. 1 or the graphic representation of Eq. 1 shown in Fig. 4 can be used to calculate the soil water potential.

Test Results

Figure 5 shows the relationships between the calculated soil water potential and temperature using various moisture contents for Type 1 clay (Lake Agassiz clay/sand mixture). The experimental data were fitted to straight line for each moisture content. The fitted equations are shown in Fig. 5. The material parameters are then correlated with volumetric water content in order to express the soil water potential as a function of volumetric water content as will be discussed later. The soil water potential for specimens with an initial water content greater than 15.20% (63.23% of water saturation) has a very small dependence on temperature. However, for moisture contents less than 15.20%, the temperature has a greater effect on the soil water potential. The measured values for soil water potential for Type 1 clay ranged between 0 to −3.0 MPa. Furthermore, Fig. 5 shows that, for the same temperature, the soil water potential increases as the moisture content decreases since the surface tension increases. Additionally, for the same moisture content, the soil water potential increases (becomes more negative) with the increase in temperature because of the decrease in viscosity.

The dependence of the calculated soil water potential on temperature for various moisture contents for Type 2 clay (sodium-bentonite/sand mixtures) is shown in Fig. 6. For specimens with an initial water content greater than 20.66%, the soil water potential depends very little on temperature. However, for moisture content less than 20.66 the temperature has a greater effect on the soil water potential. In other words, the higher the water content, the less the change of soil water potential is with temperature. At the same temperature, the soil water potential increases as the moisture content decreases because of the increase in surface tension. Also, it can be noted that the range of the measured soil water potential for Type 2 clay was from 0 to −6.0 MPa. Based on the experimental data presented in Figs. 5 and 6 and the above discussion, it can be stated that the soil water potential for Type 2 clay has a stronger dependence on temperature than the Type 1 clay. This is attributed to the clay type used in each specimen. For Type 2 clay, sodium bentonite is used which has very high swelling potential; hence high soil water potential. However, for Type 2 clay, natural clay is used which does not have high swelling potential.

Generally, the experimental results have shown that the soil water potential (negative) increases with increasing temperature. To explain this phenomenon, one has to investigate various pa-

TABLE 2—*Number and conditions of experiments conducted in this study.*

Test No.	Clay Type	Water Content, %	Degree of Saturation, %	Temperature Range, K
1	Lake Agassiz clay/sand	9.33	38.81	275 to 320
2		11.32	47.09	
3		12.97	53.74	
4		15.20	63.23	
5		17.11	71.18	
6		19.09	79.41	
7	Sodium bentonite/sand	16.05	68.25	275 to 320
8		20.66	87.85	
9		23.4	99.50	

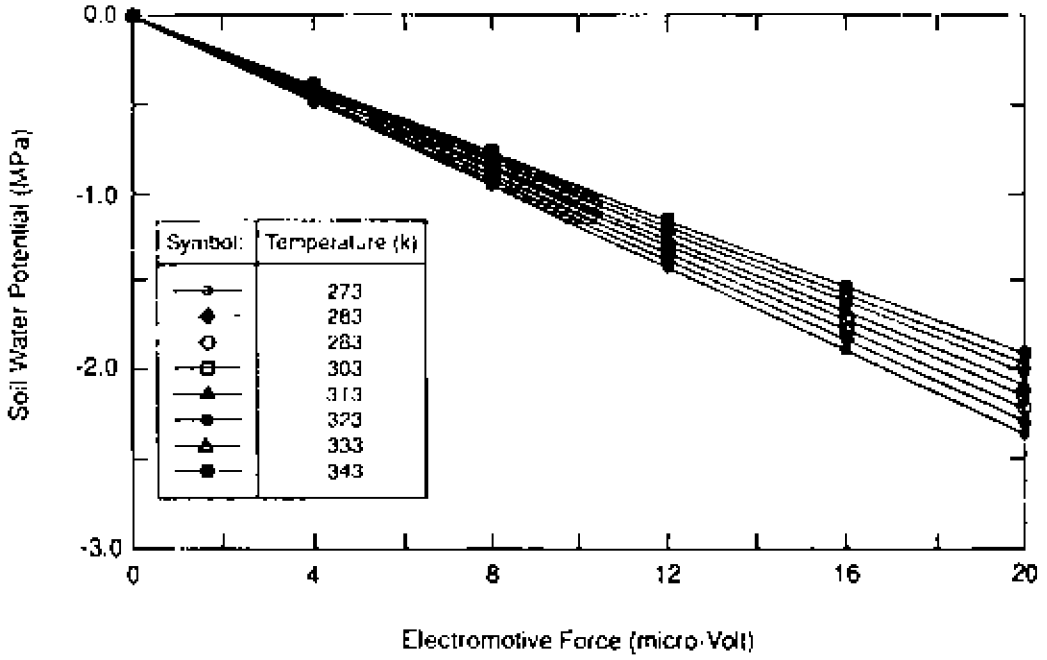

FIG. 4 — *Electromotive force/soil water potential relationships*

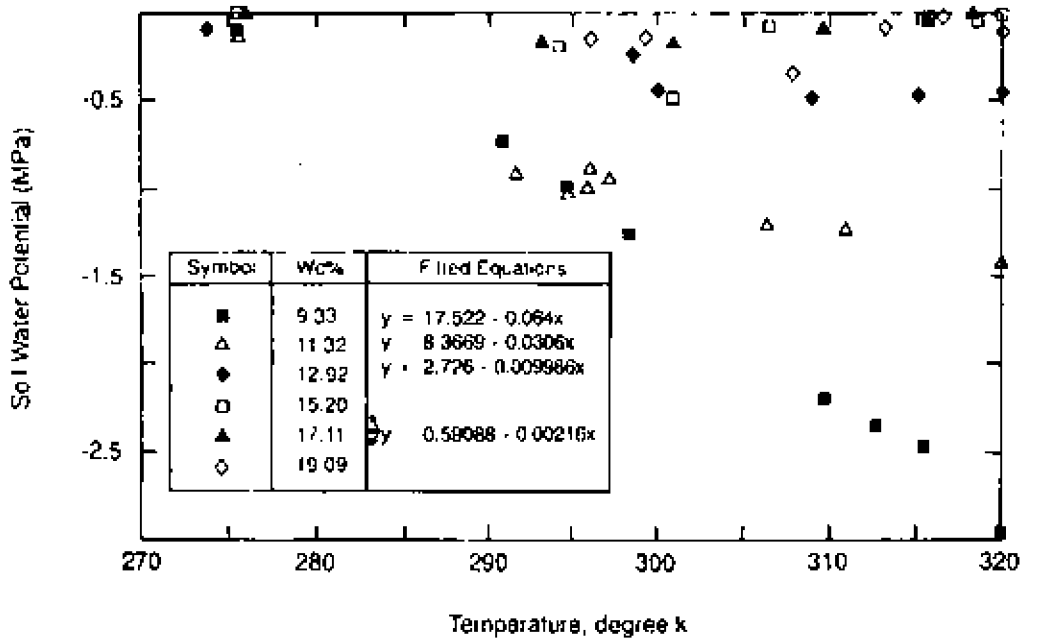

FIG. 5— *Soil water potential temperature relationships for Lake Agassiz clay/sand mixture*

rameters that contribute to this effect such as viscosity, surface tension, dielectric constant, activation energy of molecules, and measured electromotive force.

1. *Viscosity*: it is known that as temperature increases, viscosity decreases. Based on a CRC handbook of Chemistry and Physics (1985), the relationship between viscosity and temperature may be given as follows

$$\eta = 1.74 - 0.05T + 0.0017T^2 - 0.0000175T^3 \quad (2)$$

where

η = the absolute viscosity in centipose, and
T = the temperature in °C

2. *Surface tension*: it is known that as temperature increases, surface tension of soil water decreases, which leads to a reduction in water content at a given pressure head. Based on a CRC Handbook of Chemistry and Physics (1985), the relationship

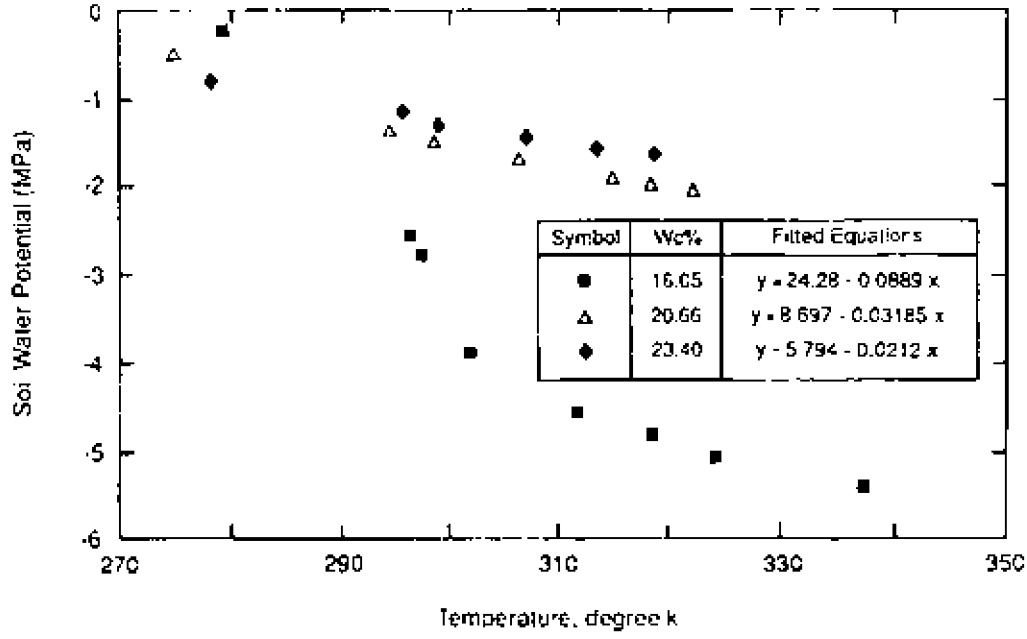

FIG. 6—*Relationship between soil water potential and temperature for bentonite:sand mixture*

between surface tension, σ, and temperature may be given as follows

$$\sigma = 75.882 + 0.165T \tag{3}$$

where

σ = surface tension in dyne/cm, and
T = the temperature in °C

3. *Dielectric constant*: It is also known that as temperature increases, dielectric constant of the soil water decreases, which leads to a reduction in the thickness of the diffused double layer. On the basis of the diffuse double layer theory, the relationship between the thickness of the double layer and the various parameters can be written as follows

$$d = \left(\frac{DKT}{8\pi C_i \varepsilon^2 \nu^2}\right)^{-0.5} \tag{4}$$

where

d = double layer thickness,
K = Boltzman constant,
T = absolute temperature,
C_i = ion concentration,
ε = unit electronic charge, and
ν = ion valence

It can be seen from the relationship that the thickness of the double layer is directly proportional to square root of dielectric content and temperature. It should be emphasized that the product of DT decreases with increasing temperature, hence, reduction in the thickness of the diffused double layer

4. *Activation energy*: As temperature increases, activation energy of water molecules and cations increases, which leads to an increase in the thickness of the diffused double layer.

5. *Electromotive force*: As temperature increases, electromotive force increases due to an increase in evaporation of water between the reference junction and the wet junction of the psychrometer

The final results to all these processes are (1) a decrease in thickness of the diffused double layer, (2) reduction in the repulsive forces, (3) increase in the attractive forces, (4) a tendency to form flocculated structure, and (4) reduction in soil water potential (i.e., increase in the negative value of the soil water potential).

After each test, specimens were taken so that the moisture content could be determined at five equal spaces at different levels along the length of the soil specimen (i.e., in each layer of the five compacted layers). There was no loss in mass during heating because the initial water content was equal to the average calculated water content after testing. However, some specimens had a very small gradient in moisture content in the order of 1.0% per meter between the bottom part of the specimen and the top part because the specimen base had been in direct contact with the heating coils in the oven.

Calculation of Soil Water Potential Based on Philip-de Vries Equation

For a given water content, can the soil water potential be fully explained on the basis of the temperature effect on the surface tension of water? To answer this question, the soil water potential is calculated using the Philip-de Vries equation (1957). The Philip de Vries equation describes the change of soil water potential with temperature

$$\frac{\partial \psi}{\partial T} = \frac{\psi}{\sigma}\frac{\partial \sigma}{\partial T} \tag{5}$$

where

ψ = soil water potential,
T = temperature, and
σ = surface tension of water

The calculation procedure can therefore be summarized as follows:

1. Using the relationship between the surface tension of water, σ, and temperature, T, given by Eq 3
2. For the same water content, the surface tension is calculated on the basis of soil temperature measured experimentally.
3. An initial soil water potential measured experimentally at room temperature is then used to calculate the soil water potential using Eq 5 in association with Steps 1 and 2

The predicted soil water potentials given by Eq 5 are presented in Figs. 7 and 8 for the two types of clay mixtures. Figure 7 shows the relationship between the experimentally determined and the predicted soil potential versus temperature for the Lake Agassiz clay/sand mixture, and Fig. 8 shows the experimentally determined and predicted relationships of the sodium bentonite/sand mixture. It can be seen that there is a large difference between the predicted soil water potential based on surface tension and the experimentally calculated soil water potential, especially at lower moisture contents. A larger temperature dependence for

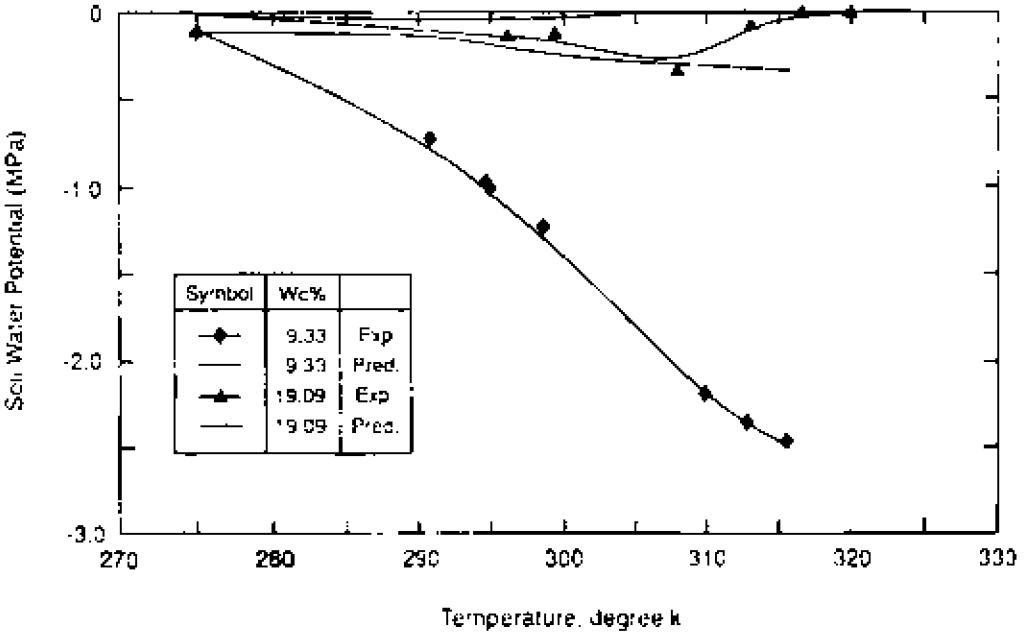

FIG. 7—*Experimental and predicted soil water potential temperature relationships for Lake Agassiz clay sand mixture*

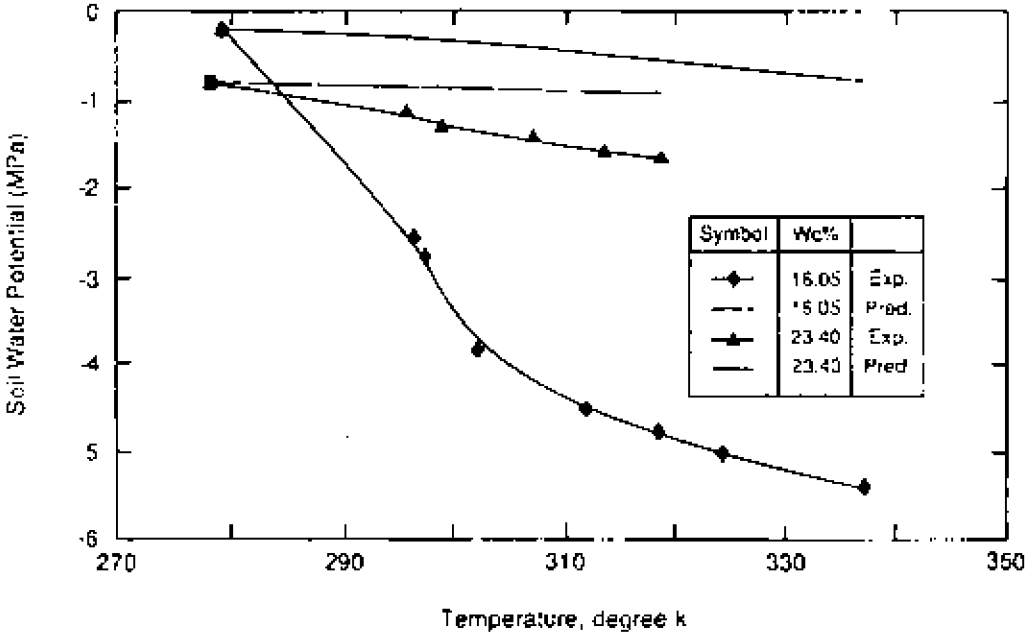

FIG. 8—*Experimental and predicted soil water potential temperature relationships of bentonite/sand mixture*

the soil water potential can be attributed to (1) the presence of solutes in soil solution [from granite groundwater (GGW)], which changes the temperature coefficient of the surface tension of water; (2) the reduction of the diffused ion layer thickness at higher temperatures, decreasing the soil water potential; and (3) the presence of entrapped air. Also, it should be noted that Eq 5 does not even predict the trend of increasing soil water potential (i.e., decrease in the negative value) with increasing soil water content for the bentonite/sand mixture, but it does for the Lake Agassiz/sand shown in Fig. 7.

Soil Water Potential-Temperature Relationships

Based on the experimental data presented in Figs. 5 and 6, the soil water potential relative to temperature and volumetric water content can be expressed as

$$\psi = A - BT \tag{6}$$

where

ψ = soil water potential in MPa,
A and B = soil parameters that are functions of volumetric water content, and
T = temperature in K.

For each specific value of volumetric water content, A and B parameters are given in Figs. 6 and 7. Furthermore, these values are then correlated to volumetric water content in order to express the A and B parameters as a function of volumetric water content. The calculated values from the curve-fitting procedures can be represented as follows.

1. *For clay Type 1: Lake Agassiz clay/sand mixture*

$$A = -\left(\frac{\ln \theta + 1.2658}{0.042}\right) \text{ and } B = 0.003654A$$

2. *For clay Type 2: sodium bentonite/sand mixture*

$$A = 0.1538\theta^{-1.555} \text{ and } B = 0.004A$$

where θ = volumetric water content.

By using the material parameters and Eq 6, the following equations for the dependence of soil water potential on volumetric water content and temperature can be derived.

1. *For clay Type 1*

$$\psi = -\left(\frac{\ln \theta}{0.042} + 30.139\right)(1 - 0.003654T) \tag{7}$$

2. *For clay Type 2:*

$$\psi = 0.1538\theta^{-1.555}(1 - 0.004T) \tag{8}$$

It should be noted that Eq 7 is applicable only for volumetric water content less than 0.2538, while Eq 8 is applicable only for a volumetric water content less than 0.3908. When the volumetric water content is greater than these two limit values, the soil water potential is considered to be independent of temperature variations. These equations (i.e., 7 and 8) are derived based on the obtained experimental data presented in Figs. 5 and 6. They can be used to calculate the soil water potential and hence the diffusivity parameter in the unsaturated buffer material based on the following equations

$$\frac{\partial \theta}{\partial t} = \frac{\partial}{\partial x}\left(K(\theta)\frac{\partial \psi}{\partial x}\right) \tag{9}$$

$$\frac{\partial \theta}{\partial t} = \frac{\partial}{\partial x}\left(K(\theta)\frac{\partial \psi}{\partial \theta}\right)\frac{\partial \theta}{\partial x} = \frac{\partial}{\partial x}\left(D(\theta)\frac{\partial \theta}{\partial x}\right) \tag{10}$$

Conclusion

Test equipment was designed and built to study the dependence of soil water potential on temperature and the volumetric water content of clay soil with high swelling potential. Two soil types were used: a Lake Agassiz clay/sand mixture and a sodium bentonite/sand mixture. The sodium bentonite/sand mixture had a high swelling potential in water relative to the Lake Agassiz clay/sand mixture. Two series of experiments were conducted for different water contents and temperatures. The results showed that an increase in water content increased the soil water potential (i.e., decrease in the negative value) for a constant temperature. When the water content remained constant, an increase in temperature resulted in a decrease in the soil water potential (i.e., increase in the negative value).

A mathematic equation relating the soil water potential to the electromotive force measured by a psychrometer was derived using psychrometer principles and equilibrium thermodynamics. A family of curves relating the soil water potential to the electromotive force was calculated. Additionally, a mathematical equation was developed relating the soil water potential to temperature and the volumetric water content.

The results show that the soil water potential decreases with temperature in both clay/sand mixtures more than predicted by the change of surface tension of water. The study demonstrated the importance of other parameters such as (1) viscosity of the pore fluid, (2) dielectric constant, (3) activation energy, and (4) electromotive force. The final results to all these interaction processes are (1) decrease in the thickness of the diffused double layer, (2) reduction in the repulsive forces, (3) increase in the attractive forces, (4) tendency to form flocculated structure, and (5) reduction in the measured soil water potential (i.e., increase in the negative value of the soil water potential). This effect is much more prominent in swelling clays at lower moisture contents.

The relationship developed for the soil water potential, temperature, and volumetric water content will enable us to calculate the diffusion parameters in coupled heat and mass flow problems. Further studies will address the calculation of the diffusion parameters and calibration of different models to predict the flow of heat and moisture in unsaturated expansive soils.

Acknowledgment

This study was supported financially under the Canadian Nuclear Fuel Waste Management Program, which is jointly funded by Atomic Energy of Canada Limited (AECL) and Ontario Hydro under the auspices of the CANDU owners group.

APPENDIX

Calculation of Soil Water Potential From Psychrometer Measurements

The aim of the psychrometer measurements is to measure the potential of water vapor existing in equilibrium with the soil water, i.e.

$$\psi = \psi_p + \psi_w + \psi_o = \psi_v \tag{1}$$

where

ψ = the total potential,
ψ_p = the potential due to external pressure,
ψ_w = the potential of water,
ψ_o = the osmotic potential, and
ψ_v = the potential of water in the vapor phase.

Since $\psi_p = 0$,

$$\psi = \psi_w + \psi_o = \psi_v \tag{2}$$

This method retains the advantages of the sorption balance method in that an air gap is used as an ideal semipermeable membrane. The time to equilibrium is shortened to zero since the potential of water vapor is measured in equilibrium with the soil water, so that no transfer of water through a vapor phase is necessary.

The measurement is based on the assumption that water vapor behaves like an ideal gas

$$\psi_v = V_v\, dP \tag{3}$$

where

V_v = the partial molar volume or specific volume of the vapor, and
P = the vapor pressure.

By substituting (RT/P) for V_v and integrating

$$\psi_v = RT \ln\left(\frac{P}{P_0}\right) \tag{4}$$

where

R = the gas constant,
T = absolute temperature,
P = the vapor pressure of water in the soil, and
P_0 = the vapor pressure of pure water.

Furthermore, when the psychrometer wet bulb is placed in a humid atmosphere, the temperature of the wet bulb is lowered as water evaporates. The maximum theoretical water bulb temperature drops to the ambient atmosphere temperature. In practice, however, the maximum depression will never be obtained due to heat transfer from the surroundings to the wet bulb. In order to present the fundamental physical principle on which the psychrometric technique is based, it is assumed that the only mechanism of heat transfer between the wet bulb and its vicinity is by the evaporation of water. Under this assumption, the placement of the wet bulb in the atmosphere is equivalent to the process of lowering the vapor pressure of water from P_0 to P. At equilibrium the free energy of both phases of vapor and liquid are equivalent and can be represented by

$$dG_v = V_v dP - S_v dT_v \tag{5a}$$

$$dG_L = V_L\, dP_L - S_L\, dT_L \tag{5b}$$

where

V and L = the vapor and liquid phases, respectively,
dG = the free energy,
V = specific volume,
dP = change in the pressure,
S = specific entropy; and
dT = temperature change.

Following any change in the system, the condition for equilibrium is that

$$dG_v = dG_L \tag{6}$$

Therefore,

$$V_v\, dP_v - S_v\, dT_v = V_L\, dP_L - S_L\, dT_L \tag{7a}$$

$$V_v\, dP_v - V_L\, dP_L = S_v\, dT_v - S_L\, dT_L \tag{7b}$$

but, since $dT_v = dT_L$ = temperature change,

$$V_v\, dP_v - V_L\, dP_L = (S_v - S_L)\, dT = \frac{L}{T} dT \tag{8}$$

where L is the latent heat of vaporization (per mole). Assuming that $dP_v = dP_L = dp$, then

$$(V_v - V_L)\, dP = \frac{L}{T} dT \tag{9a}$$

or

$$\frac{dP}{dT} = \frac{L}{(V_v - V_L)T} \tag{9b}$$

In most circumstances, one can safely assume that $V_v \gg V_L$, and Eq 9 becomes

$$\frac{dP}{dT} = \frac{L}{V_v T} \tag{10}$$

Since the vapor phase is assumed to behave as an ideal gas,

$$\frac{dP}{dT} = \frac{LP}{RT^2} \tag{11a}$$

or

$$\int_{P_0}^{P} \frac{dP}{P} = \frac{L}{R} \int_{T}^{T+\Delta T} \frac{dT}{T^2} \tag{11b}$$

where it is assumed that the temperature difference T is small

enough so that L may be considered a constant. After integration Eq 11 becomes

$$\ln\left(\frac{P}{P_o}\right) = -\frac{L\Delta T}{RT_o(T_o - \Delta T)} \quad (12)$$

Substituting Eq 12 into Eq 4

$$\psi = \frac{L\Delta T}{T_o - \Delta T} \quad (13)$$

The quantity ΔT is called the wet bulb depression since it represents the difference in temperature between a dry and a wet point existing in a humid atmosphere. Equation 13 represents the soil water vapor potential as a function of the latent heat of vaporization, bulb depression, and temperature.

Furthermore, ΔT is measured with a thermocouple thermometer. ΔT is related to the electromotive force (E) by

$$E = \alpha\Delta T \quad (14)$$

where

E = the electromotive force in μV,
α = the thermoelectric power of the thermocouple in V/K, and
ΔT = the bulb depression.

Combining Eqs 13 and 14

$$\psi = \frac{LE}{\alpha\left(T_o - \frac{E}{\alpha}\right)} \quad (15)$$

Since E/α is very small, Eq 15 can be reduced to

$$\psi = \frac{L}{\alpha}\frac{E}{T_o} \quad (16)$$

Equation 16 represents the final relationship between the thermocouple output, E, and the soil water potential. By using Eq 16 and taking $L = 539$ cal/g and $\alpha = 63\ \mu V/K$, the final relationship can be presented as

$$\psi = -35.848\frac{E}{T} \quad (17)$$

where ψ is the soil water potential in MPa.

References

Abry, D. R. M., Abry, R. G. F., Tickner, K. V., and Vandergraaf, T. T., 1982, "Procedure to Determine Sorption Coefficients of Radionuclides on Rock Coupons under Static Conditions," Atomic Energy of Canada Limited Technical Record, TR-159, Pinawa, Manitoba, unpublished report available from SDDO, AECL Research, Chalk River, Ontario K0J 1J0.

Cary, J. W., 1967, "Experimental Measurements of Soil-Moisture Hysteresis and Entrapped Air," *Soil Science*, Vol. 103, pp. 174–180.

Chahal, R. S., 1964, "Effect of Temperature and Trapped Air on the Energy Status of Water in Porous Media," *Soil Science*, Vol. 98, pp. 170–[illegible].

Chahal, R. S., 1965, "Effect of Temperature and Trapped Air on Matric Suction," *Soil Science*, Vol. 100, pp. 262–266.

Cheung, S. C. H., Gray, M. N., and Dixon, D. A., 1985, "Hydraulic and Ionic Diffusion Properties of Bentonite/Sand Buffer Materials," in Proceedings of the International Symposium on Coupled Processes Affecting the Performance of a Nuclear Waste Repository, Berkeley, CA, pp. 166–169.

Cheung, S. C. H. and Gray, M. N., 1990, "Coupled Flow of Heat and Mass in Clay Materials and its Significance to Barrier Performance," CSCE, *Proceedings*, Annual Conference and 1st Biennial Environmental Specialty Conference, Hamilton, Ontario, Supplementary Volume, pp. 18–27.

Cheung, S. C. H., Gray, M. N., Yong, R. N., and Mohamed, A. M. O., 1991, "The Effects of Moisture Content, Salinity and Temperature on the Load Bearing Capability of a Dense Clay-Based Backfill," *Material Research Society Symposium Proceedings*, Vol. 212, pp. 491–497.

Constanza, J., 1983, "Laboratory Analysis of Water Retention in Unsaturated Materials at High Temperature," in *Role of the Unsaturated Zone in Radioactive and Hazardous Waste Disposal*, J. W. Mercer et al., Eds., Ann Arbor Science, Ann Arbor, MI, pp. 147–164.

CRC Handbook of Chemistry and Physics, 1985, 66th ed., R. C. Weast, M. J. Astle, and W. H. Beyer, Eds.

Flocker, W. J., Yamaguchi, M. and Nielsen, D. R., 1968, "Capillary Conductivity and Soil Water Diffusivity Values from Vertical Soil Columns," *Agronomy Journal*, Vol. 60, pp. 605–610.

de Backer, L. W., 1967, "The Measurement of Entrapped Gas in the Study of Unsaturated Flow Phenomena," *Water Resour. Res.*, Vol. 3, pp. 246–249.

Gardner, R., 1955, "Relation of Temperature of Moisture Tension of Soil," *Soil Science*, Vol. 97, pp. 257–265.

Gray, M. N. and Cheung, S. C. H., 1986, "Disposal Vault Sealing," Atomic Energy of Canada Limited Technical Record, TR-375, pp. 253–263, unpublished report available from SDDO, AECL Research, Chalk River, Ontario K0J 1J0.

Handasah, M. and Jensen, R. D., 1972, "Effect of Temperature on Pressure Head-Water Content Relationship and Conductivity of Two Soils," *Soil Science Society Proceedings*, Vol. 36, pp. 703–708.

Lopez, R. S., 1984, "Disposal Vault Sealing," *Proceedings*, 18th International Meeting of the Nuclear Fuel Waste Management Program, Atomic Energy of Canada Limited, Geotechnical Record TR-320, pp. 150–191, unpublished report available from SDDO, AECL Research, Chalk River, Ontario, K0J 1J0.

Mohamed, A. M. O., Xu, D. M., Yong, R. N., and Cheung, S. C. H., 1990, "Application of an Identification Technique to Evaluate Diffusion Parameters in a Coupled Flow," *Proceedings*, IASTED International Conference on Modelling Simulation and Optimization, Montreal, pp. 103–106.

Nimmo, J. R., 1985, "The Temperature Dependence of Soil-Moisture Characteristics," Ph.D. dissertation, University of Wisconsin-Madison.

Peck, A. J., 1969, "Change of Moisture Tension with Temperature and Air Pressure: Theoretical," *Soil Science*, Vol. 89, pp. 303–310.

Philip, J. R. and de Vries, D. A., 1957, "Moisture Movement in Porous Media Under Temperature Gradients," *Transactions of the American Geophysics Union*, Vol. 38, No. 2, pp. 222–232.

Wilkinson, G. E. and Klute, A., 1962, "The Temperature Effect on the Equilibrium Energy States of Water Held by Porous Media," *Soil Science Society of America Proceedings*, Vol. 26, pp. 326–329.

Xu, D. M., Mohamed, A. M. O., Yong, R. N., and Cheung, S. C. H., 1991, "Evaluation of Thermal Conductivity of Backfill Material," *Material Research Society Symposium Proceedings*, Vol. 212, pp. 507–513.

Yong, R. N., Chang, R. K., and Warkentin, B. P., 1969, "Temperature Effect on Water Retention and Swelling Pressure of Clay Soils," in Special Report 103, Highway Research Board, National Research Council, Washington, DC, pp. 132–137.

Yong, R. N., Boonsinsuk, P., Wong, G., and Cheung, S. C. H., 1986, "Backfill Formulation for a Nuclear Waste Disposal Vault," in *Proceedings*, Second International Conference on Radioactive Waste Management, pp. 202–211, Canadian Nuclear Society, Toronto.

Yong, R. N., Mohamed, A. M. O., and Cheung, S. C. H., 1988, "Thermal Behaviour of Backfill Material for a Nuclear Fuel Waste Disposal Vault," *Material Research Society Symposium Proceedings*, Vol. 176, pp. 649–656.

A study of particle interaction energies in wetting of unsaturated expansive clays[1]

RAYMOND N. YONG AND ABDEL MOHSEN O. MOHAMED

Geotechnical Research Centre, McGill University, Montreal, P.Q., Canada H3A 2K6

Received July 10, 1991

Accepted June 12, 1992

The results of infiltration (wetting) experiments conducted on expansive soils demonstrate several requirements and constraints to the techniques used for the study of wetting performance of such soils. In part, these constraints are a necessary outcome of limitations imposed by the difficulties (impossibility?) of measurement of swelling pressure at the wetting front. To provide a better insight into the development of swelling and reaction pressure in the soil during the wetting process, the energies of interaction between particles and water are examined, especially in regard to those forces developed in the Stern layer. The Grahame modification of the Stern layer has been used in this study to provide the basis for calculations of interaction energies in the inner and outer Helmholtz planes. Comparison with high-pressure consolidation of a sodium montmorillonite at very close particle separation distances suggests that the addition of the energies of interaction developed in the Stern layer to the Gouy–Chapman model would permit the double-layer model to be extended to close particle spacings. Whether this is sufficient to account for the stage I wetting process is a question that remains to be further studied. For the present, the test results suggest that the expression for the total soil–water potential ψ should account for those forces of interaction, thereby providing a better account of the physical processes involved in wetting of the expansive clay and a more realistic diffusion coefficient for the total wetting process.

Key words: soil-water potential, osmotic potential, swelling pressure, volume change, wetting front, Stern layer, inner Helmholtz plane, outer Helmholtz plane, Coulombic forces, dipole–dipole interaction, ion–dipole interaction.

Les résultats d'expériences d'infiltration (mouillage) réalisées sur des sols gonflants démontrent l'existence de plusieurs exigences et contraintes pour les techniques utilisées pour l'étude du comportement au mouillage de tels sols. En partie, ces contraintes sont l'aboutissement nécessaire des limitations imposées par les difficultés (impossibilité?) de mesurer la pression de gonflement au front de mouillage. Pour fournir une meilleure compréhension du développement du gonflement et de la pression résultante dans le sol au cours du processus de mouillage, les énergies de l'interaction entre les particules et l'eau sont examinées, spécialement en ce qui concerne ces forces développées dans la couche de Stern. La modification de Grahame de la couche de Stern a été utilisée dans cette étude pour fournir la base des calculs des énergies d'interaction dans les plans intérieurs et extérieurs de Helmholtz. La comparaison avec la consolidation à forte pression d'une montmorillonite de sodium ayant des distances de séparation très faibles entre les particules suggère que l'addition au modèle Gouy–Chapman des énergies d'interaction développées dans la couche de Stern permettrait du modèle de double-couche d'être étendu aux faibles espacements de particules. À savoir si ceci est suffisant pour expliquer le processus de mouillage stage I est une question qui reste à être étudiée. Pour le moment, les résultats d'essais suggèrent que l'expression pour le potentiel total ψ sol–eau devrait tenir compte de ces forces d'interaction, fournissant ainsi une meilleure explication des processus physiques impliqués dans le mouillage de l'argile gonflante, et un coefficient de diffusion plus réaliste pour le processus total de mouillage.

Mots clés : potentiel sol-eau, potentiel osmotique, pression de gonflement, changement de volume, front de mouillage, couche de Stern, plan intérieur de Helmholtz, plan extérieur de Helmholtz, force de Coulomb, interaction bipole-bipole, interaction ion-bipole.

[Traduit par la rédaction]

Can. Geotech. J. 29, 1060–1070 (1992)

Introduction

In unsaturated soils, the existence of a potential difference in the soil will result in fluid flow in the soil in the direction of the potential gradient, i.e., in the direction of decreasing potential. Of the various components of the soil-water potential ψ that influence the development of soil wetting, the matric potential ψ_m, the gravitational potential ψ_g, and the osmotic potential ψ_s are most often considered as being sufficient in describing ψ. The piezometric potential ψ_p and the pneumatic or air-pressure potential ψ_a are generally considered to be "lumped" into the matric potential ψ_m, primarily because of the conditions existent or controlled by experimental techniques.

When an external source of "free" water is available, wetting of the soil results. For a one-dimensional case, and for the situation where both ψ_s and ψ_g are vanishingly small or zero, as might be for the case of nonswelling soils and tests involving short wetting distances or horizontal flow, if ψ_m is considered to be an unique function of the volumetric water content θ, the following relationship describing the rate of change of θ along the x axis is obtained (Yong and Warkentin 1975):

$$[1] \quad \frac{\partial \theta}{\partial t} = \frac{\partial}{\partial x}\left(k \frac{\partial \psi}{\partial \theta} \frac{\partial \theta}{\partial x}\right)$$

Assuming that no resultant volume change occurs in the soil undergoing wetting, i.e., the soil is assumed to be a rigid porous block with unchanging pore geometry, the continuity condition can be specified as follows:

$$[2] \quad \frac{\partial v}{\partial x} = -\frac{\partial \theta}{\partial t}$$

where v is water flux. Assuming the fluid diffusion coefficient D to be a function of θ in the following form:

[1]Paper presented at the workshop on "Stress Partitioning in Engineered Clay Barriers," May 29–31, 1991, Duke University, Durham, N.C.

[3] $$D(\theta) = k(\theta)\frac{\partial \psi}{\partial \theta}$$

the well-recognized fluid flow diffusion equation is obtained:

[4] $$\frac{\partial \theta}{\partial t} = \frac{\partial}{\partial x}\left(D(\theta)\frac{\partial \theta}{\partial x}\right)$$

It needs to be noted that the relationship shown in [4] has been obtained as a direct consequence of the specific continuity condition invoked, i.e., no resultant volume change occurs as a result of fluid flow into and out of the soil (original pore geometry remains unaltered). This condition (i.e., rigid porous geometry) can be considered to be applicable (more or less) for nonswelling and noncollapsing soils, i.e., $\psi = \psi_m$ (no osmotic or other potential gradients are considered). In the case of unsaturated clays, studies on the wetting phenomenon that results from fluid flow have been well reported in the literature, e.g., Philip and Smiles (1969), Yong and Warkentin (1975), Zaslavsky (1965). For clay soils with little swelling potential (no volume change), it has been shown that the classical diffusion equation can predict moisture transport in the soil. However, in the case of expansive clays, the presence of swelling forces influences the development of the wetting front, resulting thereby in the need for consideration of interparticle relationships and volume change in calculating the soil-water potential ψ. Two limit conditions can be specified during the wetting process in laboratory testing of unsaturated flow in expansive clays: (*i*) the confined situation where no volume change is permitted, and (*ii*) the unconfined case where the free swell is allowed to occur. In the first instance, the restriction of "constant volume" will result in development of swelling forces in the contained soil, and in the second instance, the free-swell condition will produce changes in soil volume which will undoubtedly influence the diffusion rate of moisture transport.

The scarcity of proper experimental (test) information on swelling pressures developed in a confined swelling soil during wetting does not permit one to categorically state that the developed swelling pressures would not affect the transport rate of the fluid, i.e., the diffusion coefficient may (or may not?) be considered to remain constant throughout the transport process. Development of an experimental test technique to measure swelling pressures along the test column during the advance of the wet front is fraught with difficulties. Not only is the measurement of swelling pressure at the moving wetting front very difficult to achieve, but also it is not immediately clear that measurements of total swelling pressure obtained by gauges located at the end of the test sample, which includes both the wetted and unwetted portions of the test sample, are indicative of the pressures developed at the wetting front. The problem of determination of compression of the unwetted portion (due to the swelling pressures developed in the wetted portion) and its influence on the developed swelling pressures measured at the end of the sample remains to be resolved. Accordingly, assumptions made which presume that the unsaturated soil portion remains rigid (i.e., acts as a rigid piston?) and thus will not affect the developed swelling pressures at the wetting front have yet to be tested to determine whether they are tenable.

Adopting the free-swell test condition, i.e., allowing unrestricted swelling of the sample during wetting, as a laboratory test technique for evaluation of the rate of moisture transport in unsaturated expansive clays requires one to account for changes in the diffusion coefficient when volume changes and associated volumetric water content changes occur along the length of the test column. Data-reduction techniques (Yong and Warkentin 1975) that permit one to deduce the diffusion coefficient from measurements of wetting-front advancement must account not only for the volume and θ changes occurring in the wetting portion of the test column but must also ascertain that the unwetted portion remains essentially in the no-volume change (rigid) condition. Otherwise, the changes in the bulk density (particle arrangement and porosity) of the unwetted portion would create fluid-transport conditions dissimilar to those in the wetted portion. Assuming a direct relationship between volume change and swelling-pressure development, and further assuming that the potential equivalence of the swelling pressure is the osmotic potential ψ_s, it follows that ψ_s would need to be considered in the ψ term in [3] in the determination of the diffusion coefficient.

In studying the wetting of a swelling soil, it is important to distinguish between at least two kinds of soil initial conditions, i.e., a completely dry soil as opposed to a partially wet but unsaturated soil. The first initial condition is generally referred to as a dry soil, whereas the second kind of initial soil condition is often referred to as a moist or partly saturated soil. The distinction between the two initial conditions is important in that for the dry swelling soil condition, the resultant volume change that occurs on wetting of the soil would initially be due to hydration of the dry clay particles. van Olphen (1977) indicates that volume changes as high as 100% of the present volume of the dry clay can be obtained for the condition when four monolayers of water enter between the layers of a montmorillonite clay. Beyond this point, where a moist condition can be said to exist, swelling of the clay soil upon wetting is a result of the repulsive forces developed between adjacent clay particles. The two stages of wetting (van Olphen 1977) can be conveniently considered as stage I, where the volume change is due to the hydration energies of interaction, and stage II, where volume change is due to the energies developed due to double-layer repulsion. This is consistent with the analyses given by Nimham (1981), who indicated that surface forces at small distances are dominated by surface-induced liquid structure, and that continuum theories are better applied at distances beyond 10–20 molecular diameters. What happens in the stage I region of wetting? To address this question, a study of swelling-pressure–volume-change relationships at very close particle spacings could perhaps provide some answers in regard to hydration energies of interaction established. The insight obtained therefrom could contribute to a better understanding of the wetting of unsaturated expansive clays.

The Gouy–Chapman diffusive double-layer (DDL) model has been shown to provide capable predictions for interactions occurring at particle spacings distant for the Stern layer. However, evidence from reported studies on osmotic or swelling pressure of active clay soils shows that at close particle separation distances, additional forces or mechanisms not considered in the DDL models were unlikely responsible for unpredictable volume changes or pressures. For example, studies by Barclay *et al.* (1972) show that at particle separation distances of less than 15 Å (1 Å = 0.1 nm), pressures between particles of sodium montmoril-

TABLE 1. Physical properties of materials used

	Kaolinite	Sainte-Rosalie clay	No. 14 glass beads
Minerals present	Kaolinite	Mica and chlorite, with feldspar, amphibole, and small amount of montmorillonite	
Liquid limit (%)	58.4	48.0	
Plastic limit (%)	39.6	23.0	
Specific gravity	2.65	2.7	2.44
Grain-size distribution	100% < 0.1000 mm	68% < 0.200 mm	95–100% with diameter
	75% < 0.0056 mm	52% < 0.002 mm	0.23–0.42 mm
	50% < 0.0015 mm		

lonite in the 10^{-4} M NaCl solution were considerably higher than those predicted from DDL models. Studies reported by Israelachvili (1982) and Pashley (1982) in regard to forces developed between two mica surfaces immersed in an electrolyte solution indicate that additional repulsive forces could be present when particle separation distances become less than 3 nm. The modifications introduced by the Stern (1932) model to account for non-Coulombic interaction between the counterions immediately adjacent to the clay particle surfaces, together with further modifications introduced by Grahame (1947) indicate that a determination of the forces raising from the interactions occurring at the clay–counterion interface could provide a means for explaining the "unpredictable volume changes or pressures."

The need to study some of the problems concerning unpredictable volume changes or pressure, especially at close particle spacings, is considered to be a requirement in sorting out the difficult problems associated with not only the design of experimental procedures for measurement of moisture transport in unsaturated expansive clays but also analysis of the results obtained therefrom. The two-stage concept of energies of interaction (van Olphen 1977) is a useful concept in evaluation of the volume-change and developed swelling-pressure aspects of the moisture-transport problem. The study reported herein has been structured as two separate kinds of experiments. The first type of experiments was designed to examine wetting of initially saturated (slightly moist but not totally dry) soils, whereas in the second type of experiments swelling pressures developed at very close particle spacings for a montmorillonite soil. Obviously, it would have been useful to construct an experimental technique that would permit one to obtain all the information from the two types of tests without having to perform two different and separate kinds of experiments. However, both information and instrumentation constraints proved too difficult to overcome at this stage.

In the first series of experiments, conducted to study the wetting phenomenon of initially unsaturated soils, the results for a natural expansive soil are examined in relation to the development of the wetting-front advance, with and without constraints on axial expansion of the test samples. This set of results is compared with the wetting performance of a nonexpansive soil to provide indications as to the effect of the swelling potential on control of the wetting characteristics of the soils. The results can be used to calculate the diffusion coefficient using the "wetting front advance," the technique given in Yong and Warkentin (1975). In the second part of the study, the energies of interaction developed between soil particles at close and distant spacings are evaluated to permit the soil-water potential ψ to take into account the interaction energies developed at that particle surface – water interface (in the Stern layer), inasmuch as this is considered to be the stage I hydration process, and a significant energy component in the wetting process, as discussed previously. The experiments conducted in support of the development of the interparticle model included high-pressure consolidation experiments on a sodium montmorillonite clay. It is hypothesized that the test results obtained from the two different types of experiment could indicate whether information on particle interaction energies could contribute to a better insight into the stage I wetting and total wetting process relative to constrained and unconstrained boundary conditions.

Experimentation

Infiltration-wetting experiments

The physical properties of the natural expansive soil (from Sainte-Rosalie, Que.), the control kaolinite soil, and the No. 14 glass beads used to mix with the Sainte-Rosalie clay tested in the wetting experiments are shown in Table 1. The Sainte-Rosalie clay (SR) was used as 100% SR and as 50 and 75% SR mixtures with No. 14 glass beads. To prepare the mixtures of SR and glass beads in powdered form, the SR passing through a 0.25-mm sieve was mixed with the glass beads in the desired proportions, and a slurry was formed with the mixture at a water content slightly above the corresponding liquid limit. The slurry was then deaired under vacuum in 3.5-cm ID split moulds and allowed to air.

The basic test apparatus for the infiltration-wetting experiments shown in Fig. 1 utilized a double Mariotte flask system to maintain a constant (water) head. By varying the elevation of the atmosphere-pressure inlet, various positive or negative heads could be imposed for the different test series. The basic test system was adapted for measurement of developed swelling pressure in the test series designed to determine swelling pressure during soil wetting. A pressure transducer was mounted on the lucite platen located at the end of the sample. This platen, with the pressure transducer facing the end-plate restraint, was brought to bear against the restraint, and a zero pressure condition was experimentally set before commencement of the wetting tests. The pressures developed were recorded during the advance of the wet front in the test sample. Although this did not give the actual pressure developed at the wetting front, it nevertheless provided information on the nature of pressures

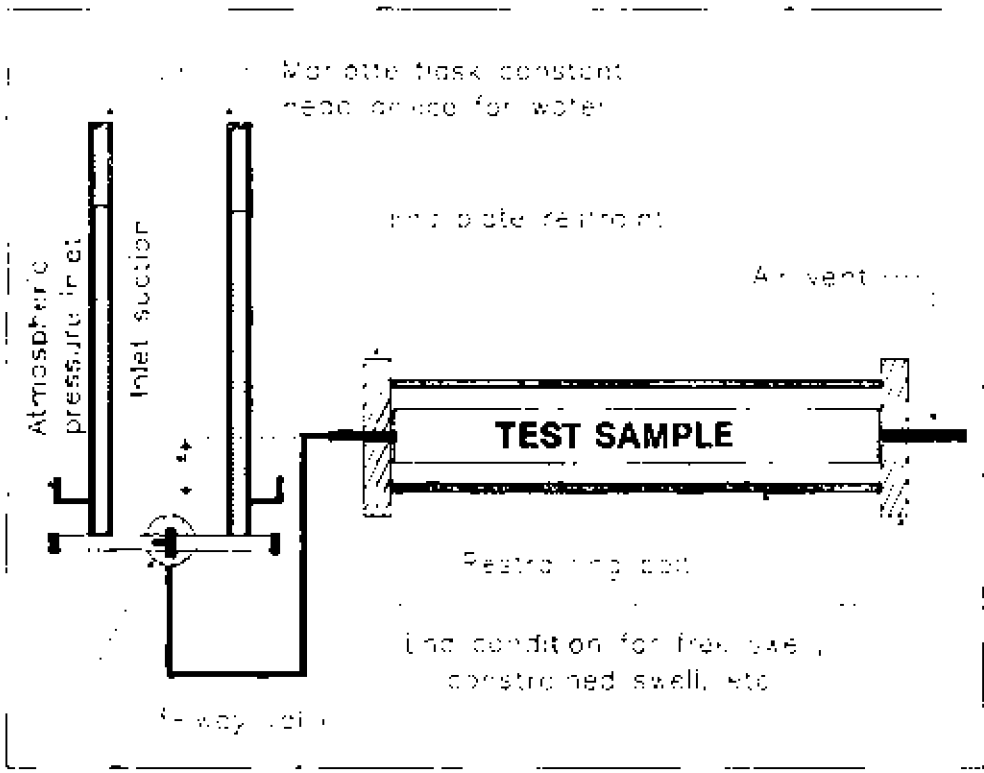

FIG. 1. Schematic of test system used for wetting study.

being developed during wetting. The question of whether some compression of the wetted and unwetted portions of the clay could detract from the actual pressures developed at the wetting front has yet to be addressed.

For the unconstrained swelling test, information on axial expansion of the test sample during wetting was obtained by substituting the pressure gauge with an extensometer. A sufficient length of sample column was provided to allow axial expansion to occur. The inside of the test column was liberally lubricated with petroleum jelly to minimize frictional resistance between the test sample and the sides of the column. It is, however, recognized that this resistance may be of some consequence, and thus the results obtained should be used in a qualitative sense.

High-pressure consolidation experiments

Since the DDL model, which permits one to gain insight into the role of soil–water interaction in development of swelling pressures, has been well reported for tests with Na montmorillonite, this series of experiments was conducted using montmorillonite. The montmorillonite used in this portion of the study was obtained from Fisher Scientific Company, Fairlawn, N.J., and sodium saturation of the montmorillonite was obtained by repeated washings with 1 M NaCl. Following removal of excess salts through washing of the montmorillonite with alcohol in an ultracentrifuge, the montmorillonite was dried at 105°C and subsequently pulverized.

The cation exchange capacity (CEC) and the specific surface area (SSA) of the sodium montmorillonite were determined using atomic-adsorption (Chabbra *et al.* 1975) and ethylene glycol monoethyl ether (EGME, Eltantway and Arnold 1973) techniques, respectively. The values obtained were CEC = 118 mequiv/g, and SSA = 885 m^2/g. These values agree well with published results, e.g., van Olphen (1977). For pressure measurements, a high-stress consolidation cell with compression capability of up to 500 MPa, and with both top and bottom drainage, was constructed (Alammawi 1989) to study the high-pressure swelling-pressure characteristics of the clay using a procedure akin to the consolidation test. In the procedure used to promote parallel particle orientation of the clay particles, a suspension of Na-montmorillonite clay with the desired electrolyte concentration was centrifuged (using the ultracentrifuge), and the sediment was then frozen after decantation of the supernatant to promote dispersion of the clay after thawing. Experience with sediments formed from surface soil suspensions, especially those from the studies reported by Yong (1984), indicates that when the sediments are frozen, the sediment particles tend to be dispersed when thawed. Although the exact mechanisms promoting this tendency are not fully known, this procedure was adopted for the montmorillonite clay. By subjecting the specimens to consolidation loads, the mechanical compression would, in combination with the initial dispersed fabric of the soil, be most likely to develop preferred parallel orientation of the soil particles.

To calculate the separation distance between particles from void ratio determinations, on the assumption that the system is fully saturated and that the soil particles are aligned parallel to each other, the relationship given by Bolt (1956) can be used:

$$[5] \quad e = \gamma_w G_s S_s d$$

where e is void ratio, γ_w is density of water (Mg/m^3), G_s is specific gravity of solid particles, S_s is specific surface area of the solids (m^2/g), and d is one-half of the separation distance between adjacent parallel particles. The final consolidation load of 400 MPa produced a void ratio (e)

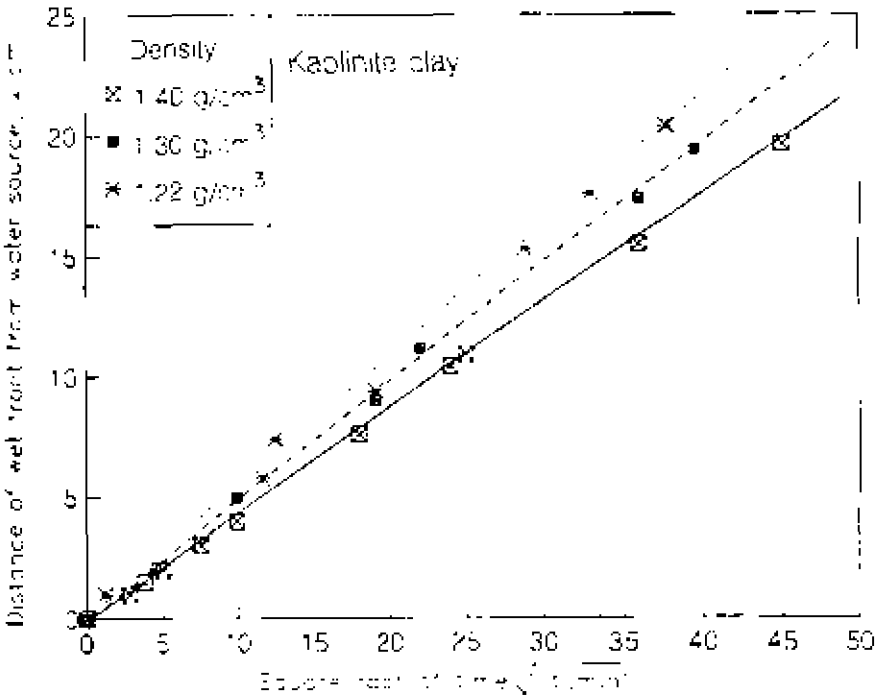

FIG. 2. Wetting-front advance for kaolinite clay at various densities.

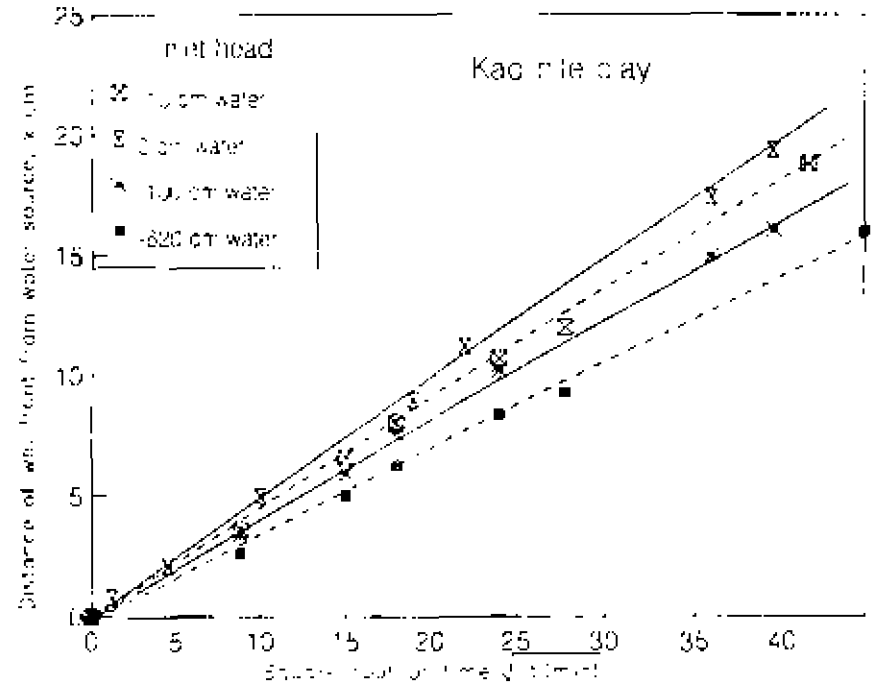

FIG. 3. Influence of inlet suction on advance of wetting front for kaolinite clay.

of 0.52, equivalent to the separation half distance (d) between particles of 0.24 nm.

Void ratios (e) and separation distances (d) of the sample were calculated during the consolidation test, using a specific gravity value of Na montmorillonite of 2.5 as determined for the as-supplied state of the montmorillonite, using a non-polar liquid (methyl alcohol CH_3OH). This value is in close agreement with published average values for montmorillonite (e.g., Waldelich 1958).

Results and discussion

Infiltration–wetting experiments

To demonstrate the classical situation representative of rigid pore geometry infiltration, as generally assumed in the continuity condition $\partial v/\partial x = -\partial\theta/\partial t$ in development of [3], the advance of the wetting front for the kaolinite samples at various bulk densities and at various inlet suctions is shown in Figs. 2 and 3, respectively. The linearity obtained between wetting-front advance x and the square root of time

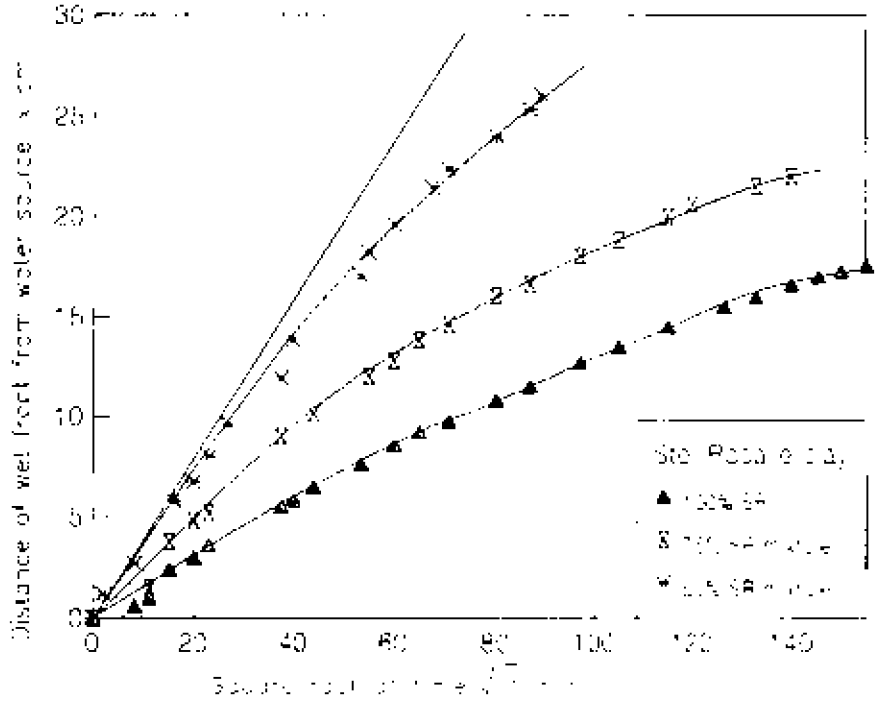

FIG. 4. Wetting-front advance for Sainte-Rosalie clay (SR).

confirms that the continuity conditions leading to development of [3] have been generally met. It is recalled that by invoking the Boltzmann transform $\eta = x/(t)^n = \eta(\theta)$ (Yong and Warkentin 1975) to reduce the classical diffusion equation (eq. [3]) to an ordinary differential equation to obtain a closed-form solution, linearity between x and square root t as a physical fact is required. It should be noted, however, that this is not a necessary condition for the classical diffusion equation if the continuity condition is restated to permit volume change. Also, different forms for $D(\theta)$ can be written in relation to volume change, and the resultant [3] solved using numerical techniques.

Taking the bulk density of 1.3 Mg/m^3 as the comparative case for the swelling SR and nonswelling kaolinite clay, the wet-front advance at various times of the pure SR and SR mixtures is shown in Fig. 4, for the situation where the swelling has been allowed. For comparison, the kaolinite results for the similar bulk density are also shown. To continue with the comparisons the 50% SR mixture is chosen to represent the restrained swelling case for wet-front advance with time (Fig. 5). Similar comparisons can be obtained for the other SR mixtures. The results shown in Fig. 4 demonstrate the influence of greater swelling, as represented by the higher SR proportions, on the wet-front advance with time. Departure from linearity in the x versus $(t)^n$ relationship is obvious. The greater influence exercised from the restrained swelling case, even for the 50% SR mixture, is shown by the higher degree of curvature in the wet-front advance versus time relationship. As noted from the companion curve illustrating the developed swelling pressure in Fig. 5, the pressures measured at the unwetted end of the sample increase in a fashion corresponding to the rate of advance of the wet front. This relationship does not, upon first viewing, appear to be consistent with expectations based on experience with classical swelling-pressure experiments such as those reported previously in the literature (e.g., Bolt 1956; Warkentin and Schofield 1962; Yong *et al.* 1963). The results indicate that in swelling-pressure experiments conducted on the same kind of Na montmorillonite (i.e., same molal concentration), where thin (saturated) samples are tested, the relationship established between swelling pressure and volumetric water content (or particle spacing) is unique, provided that the soil particles are oriented parallel to each other. Clearly, the relationship established between swelling pressure and rate of advance of wet front (from the wetting experiment) shows that the physical (experimental) conditions necessary for the classical swelling-pressure experiment have not been duplicated in the wetting experiment. The length of the test sample used for the wetting experiment, coupled with possible compression of both the wetted and unwetted portions of the test sample during wetting, will contribute greatly to control of the relationship between swelling pressure and rate of advance of the wet front. Since undetermined side-friction effects will also be influential in the development of resultant swelling pressures, it is clear that the results of the developed swelling pressures cannot be accepted as exact quantitative values. However, the qualitative performance of the pressure curve provides a good indication of the participation of developed swelling pressures in the control of rate of wetting-front advance. Similar types of results can be obtained for the 75% SR mixture and for the SR clay, with greater developed swelling pressures and correspondingly greater curvatures for the wetting-front curves.

The question of how all these pieces of information can be evaluated in terms of required modification of the classical fluid-diffusion relationship as represented by [3] can be answered in part by a restatement of the continuity condition to account for volume change, for the case where free swelling of the soil is allowed during soil wetting. This can

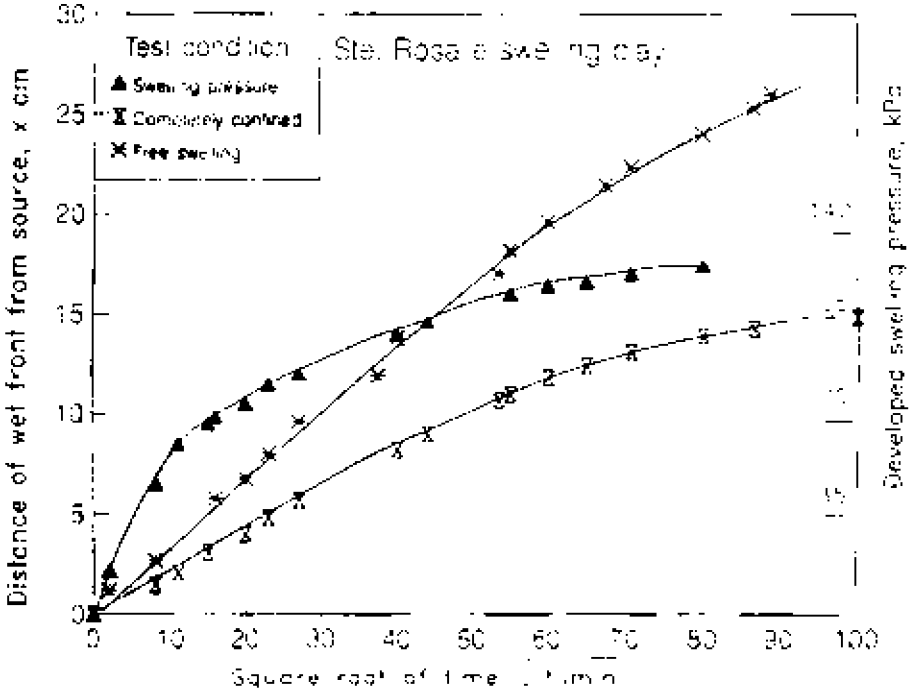

FIG. 5. Swelling pressure and swelling effect on wetting-front advance for Sainte-Rosalie clay.

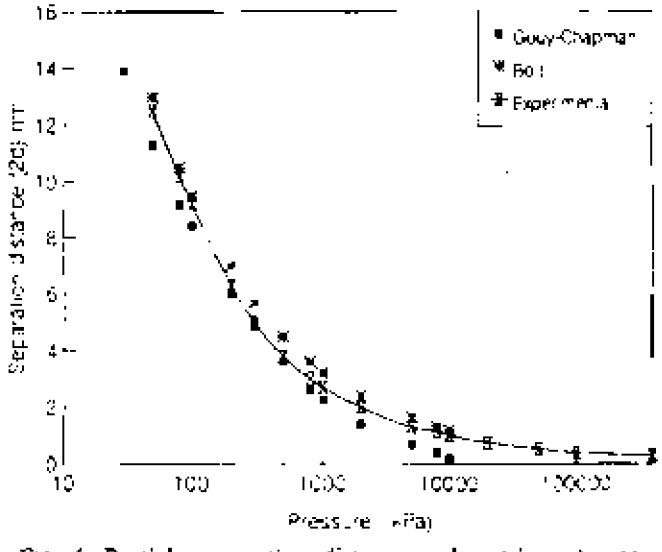

FIG. 6. Particle separation distance, volumetric water content, and swelling pressure for Na-montmorillonite clay at 10^{-3} M NaCl.

be achieved by using the material coordinate system similar to that proposed by Philip and Smiles (1969). This system, which permits accountability for volume change, is simple, since the analytical formulation is similar, in a sense, to the no-volume-change analysis, specifying the relation between material coordinate m and x as

$$m = \int_{\infty}^{x} \frac{dx}{1 + e}$$

where e is void ratio. The corresponding continuity condition will then be given as

$$[5] \quad \frac{\partial}{\partial t}[\theta(1 + e)] = -\frac{\partial v_{ws}}{\partial m}$$

where v_{ws} is velocity of water relative to moving soil particles. Writing Darcy's relationship in terms of water movement relative to the moving soil particles:

$$[6] \quad v_{ws} = -k \frac{\partial \psi}{\partial x}$$

Substituting [6] into [5], the fluid-flow diffusion equation for the case where volume change occurs as a result of soil wetting takes the following form:

$$[7] \quad \frac{\partial}{\partial t}[\theta(1 + e)] = \frac{\partial}{\partial m}\left(k \frac{\partial \psi}{\partial x}\right)$$

and thus

$$[8] \quad c \frac{\partial \theta}{\partial t} = \frac{\partial}{\partial m}\left(D_m \frac{\partial \theta}{\partial m}\right)$$

where void ratio e and soil-water potential ψ are assumed to be functions of volumetric water content θ only (without significant loss of accuracy, Yong and Warkentin 1975), and

$$c = 1 + e + \theta \frac{\partial e}{\partial \theta}$$

$$D_m = \frac{k}{1 + e} \frac{\partial \psi}{\partial \theta} = \frac{D(\theta)}{1 + e}$$

In view of the identical form between [8] and [4], the technique for solution of [8] would also be similar. Writing the Boltzmann transform as

$$[9] \quad \lambda' = \frac{m}{t^{1/2}}$$

[8] can be reduced to an ordinary differential equation and solved subject to the specification of appropriate boundary conditions (Philip and Smiles 1969; Yong and Warkentin 1975).

For the case where swelling is constrained, i.e., no volume change under developed swelling pressures, it is noted that, whereas the no-volume-change continuity condition is

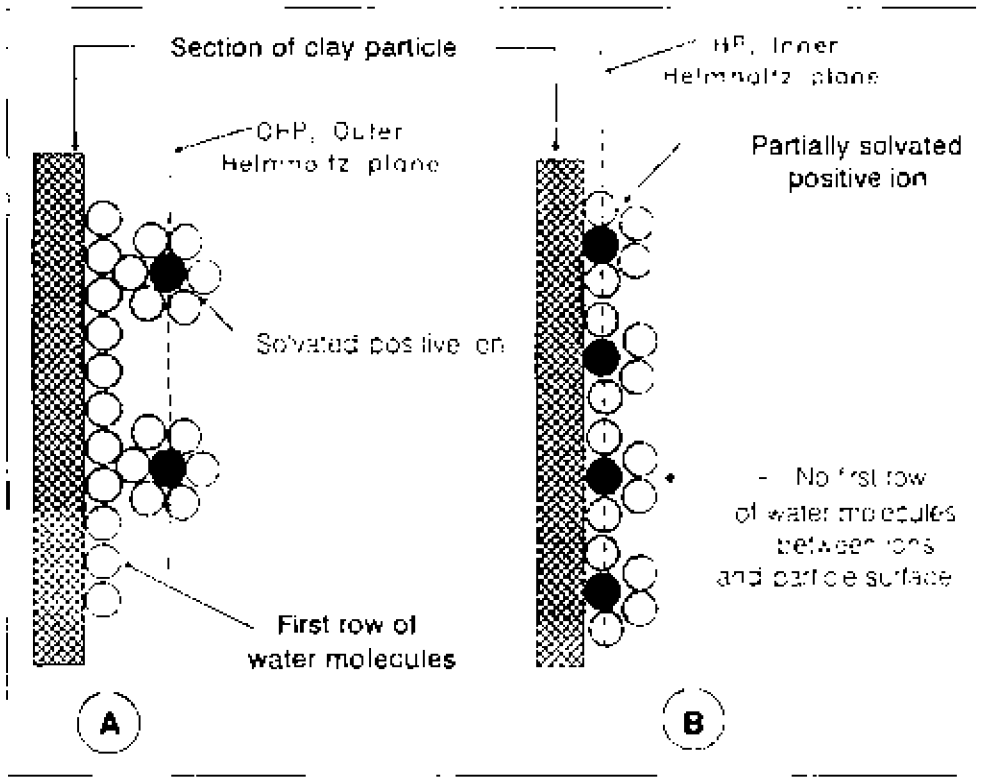

FIG. 7. Two types of arrangement of ions at the particle surface – water interface.

apparently satisfied, the test results obtained will not, in all probability, match the predictions made from the model represented by [3] because of the swelling pressures developed, as noted in Fig. 5. If such is the case, a reevaluation of the swelling – volume change phenomena in the wetted and unwetted portions of the test column and their impact on the soil-water potential, i.e., the ψ term in [3], is needed, especially in regard to the wetting phenomenon where hydration interaction energies are developed at the particle surface – water interface.

High-pressure consolidation and particle interaction energies

As noted in the Introduction, it is important in the study of wetting of a swelling soil to recognize that wetting of a completely dry soil as opposed to a partially wet but unsaturated soil cannot be analyzed without due consideration to the differences in energies of interaction established between particles during the course of wetting. The differences between the two initial soil conditions are thought to be due to the fact that wetting of an initially dry swelling soil produces resultant volume change due to interaction energies responsible for hydration of the dry clay particles. This has been referred to (van Olphen 1977) as the stage I wetting process. The reasoning given is that, whereas the general DDL models can describe the swelling-pressure and volume-change phenomena for the stage II wetting process where energies of interaction due to double-layer interaction dominate, the stage I process where hydration forces dominate can benefit from a closer examination of the energies of interaction developed. To provide a means for evaluation of the energies of interaction developed in the stage I process, the energies of interaction developed in the Stern layer are examined, using high-pressure consolidation tests on Na montmorillonite. It is recognized that these results pertain to the fully saturated soil condition and should therefore be used more in the qualitative sense as input for evaluation of the stage I wetting process than as quantitative values for direct application to analyses of wetting of an initially dry swelling soil.

The results from a high-pressure consolidation test on Na montmorillonite are shown in Fig. 6 together with the calculated results obtained using the Gouy-Chapman (DDL) model and the experimental results reported by Bolt (1956). The detailed development of the relationships for the DDL model and method for calculating the variation of total interaction energy (swelling pressure with particle separation distance) can be found in various reference texts and publications, e.g., Kruyt (1962), van Olphen (1963), Yong and Warkentin (1975), Bohn *et al.* (1979), and thus will not be repeated herein.

The assumptions made for the computed values in Fig. 6 included the following. (1) The relationship between particle separation distance ($2d$) and the overall system void ratio (e), where d represents the equilibrium half-distance between interacting particles, i.e., particle spacing between two adjacent interacting particles at equilibrium, is $2d$. (2) The clay soil is fully saturated, and hence capillary forces may be neglected. (3) The clay particle surfaces are smooth (i.e., surface roughness is neglected). (4) The relationship between total interaction energy E_T and the overall soil-system pressure (P) is expressed as (Barclay *et al.* 1976) $P = \partial E_T/\partial(2d)$. (5) Parallel orientation of clay particle has been achieved in the high-pressure consolidation experimentation, thus permitting use of the face-to-face mode for calculations using the Gouy-Chapman model (with and without the modifications developed in this study).

The results shown in Fig. 6 indicate good agreement between the measured values of Bolt (1956) and this study

and also good agreement between the calculated values and the experimental one for particle spacings above 3 nm. However, at values below 3-nm particle spacings, the measured values do not accord well with those calculated values obtained from the DDL model. This is not unexpected, since the DDL model presumes that the potential at the charged particle surface ψ_p drops linearly to ψ_δ, the potential in the Stern layer, and that the drop of the potential at the Stern layer to the potential ψ_i, the potential at a distance x_i away from the charged particle surface (i.e., ψ_δ to ψ_i), occurs in the Gouy layer. To seek better accord between experimental observations and computed values from the DDL model, the Stern and Grahame suggestions of the electric double layer, i.e., the charged particle surface and the immediate adjacent layer of counter ions, need to be considered in determination of the additional energy term required for modification or extension of the DDL model. The Grahame (1947) partitioning of the Stern layer into two parts, an inner Helmholtz plane (IHP) with potential ψ_{ih} and an outer Helmholtz (OHP) with potential ψ_{oh} equal to ψ_δ, provides the opportunity to examine the interaction energies developed in the layers. The problem of a viable description of the (soil particle) solid–liquid interface in the context of an electrified interface has been discussed by Bockris and Reddy (1970). In regard to the question of the "sticking" of ions to the electrode, two types of arrangement of ions "struck" on an electrode (Figs. 7A, 7B) (Grahame 1947): arrangement A where the hydrated ions interact with the electrified surface with a water molecule separation, and arrangement B where the ions are in direct contact with the surfaces, resulting thereby in partial hydration of the ions. The problem for consideration reduces to an assessment of what constitutes the closest approach distance for the ions and a determination of the forces that influence the sticking of ions to the charged interface. One recognizes that whatever arrangement of ions and water molecules exists at the interface, this arrangement needs to correspond to the configuration of lowest free energy. For arrangement B to occur, ions in the OHP must enter the IHP.

In the Gouy–Chapman model without the Stern correction, the charge on the surface of the particle σ_p must be balanced by the total space charge in the soil solution, if electroneutrality is to be preserved, i.e.,

$$\sigma_p = \sigma_g = -\int_0^\infty \rho_x \, dx$$

where σ_g is surface charge balanced by the diffuse Gouy–Chapman layer, and ρ_x is net charge density at a distance x from the charged surface (volume charge). As detailed in the various reference texts, the Boltzmann relationship for ρ_x as

$$[11] \quad \rho_x = \sum_{x=0}^{\infty} n_{ix} z_i \epsilon = \sum_{x=0}^{\infty} n_{i\infty} z_i \epsilon \exp\left(\frac{-z_i \epsilon \psi_x}{\kappa T}\right)$$

where n_{ix} is concentration of ith species at distance x, $n_{i\infty}$ is concentration of ith species in the bulk solution (outside the influence of the charged surface, z_i is valence of species i, ϵ is electronic charge, ψ_x is electric potential at x, κ is Boltzmann constant, and T is absolute temperature.

In regard to σ_g, the factor within the exponential bracket in [11], $(-z_i \epsilon \psi_i / \kappa T)$, represents the ratio of the electrical and thermal energies of an ion at a distance x from the charged surface. Invoking the Poisson relationship between electric potential and space density, i.e.,

$$\rho_x = -\frac{n}{4\pi} \frac{d^2\psi_x}{dx^2}$$

solution for σ_g can be obtained as the well-known Gouy–Chapman equation:

$$[12] \quad \sigma_g = \left| 2\epsilon\kappa T \sum_{x>0}^{x=\infty} n_{i\infty} \exp\left(\frac{-z_i \epsilon \psi_{oh}}{\kappa T}\right) - 1 \right|^{1/2}$$

However, with the inclusion of the Grahame–Stern modification, and with the model shown in Fig. 7 (arrangement B), [12] needs to include consideration of interactions in the Stern layer. Identifying the surface charge due to the ions in the IHP and OHP as σ_{ih} and σ_{oh}, respectively, the surface charge at the particle surface is balanced by the contributions of both σ_{ih} and σ_{oh} as follows:

$$[13] \quad \sigma_p = \sigma_{ih} + \sigma_{oh}$$

where $\sigma_{oh} = \sigma_g$. To determine σ_{ih}, one needs to obtain the concentration of ions of species i in the IHP, $(n_{i,ih})$, inasmuch as

$$[14] \quad \sigma_{ih} = z_i \Delta x n_{i,ih} \epsilon$$

where Δx is thickness of water layer (2.8×10^{-10} m). From the Boltzmann relationship:

$$[15] \quad n_{i,ih} = n_{i,oh} \exp\left(\frac{E_{oh} - E_{ih}}{\kappa T}\right) = n_{i\infty} \exp\left(-\frac{z_i \epsilon \psi_{oh}}{\kappa T}\right) \exp\left(\frac{E_{oh} - E_{ih}}{\kappa T}\right)$$

where E_{ih} and E_{oh} refer to the interaction energies in the IHP and OHP, respectively, $n_{i,oh}$ refers to the concentration of ions of species i in the OHP, and ψ_{oh} refers to the electronic potential at the OHP.

E_{ih} can be calculated in terms of the Coulomb forces as $E_{ih} = E_c = z_i \epsilon^2 / \xi R$, where R is distance between the centre of the ion i and the negative charge site of the particle, and ξ is dielectric constant. For E_{oh}, one needs to consider not only the same Coulomb forces but also the short-range forces arising from (*i*) ion–dipole interaction, (*ii*) dipole–dipole interaction, and (*iii*) dipole–site interaction. The ion–dipole interaction energy E_{id} can be computed according to Barrow (1973) as

$$[16] \quad E_{id} = \frac{\mu \epsilon}{\xi r^2}$$

where μ is dipole moment of the water molecule ($= 1.8 \times 10^{-18}$ esu cm), ϵ is electronic charge ($= 4.8 \times 10^{-10}$ esu), r is sum of the radii of the ion and water molecule (assuming nondeforming spheres), and ξ is dielectric constant ($= 5$).

Since dipole–dipole interaction could substitute for ion–dipole interaction, the result of dipole–dipole interaction and the magnitude of reduction of E_{id} will increase as the number of absorbed (interacting) water molecules increases. This reduction was calculated by Bernal and Flower (1933) to be

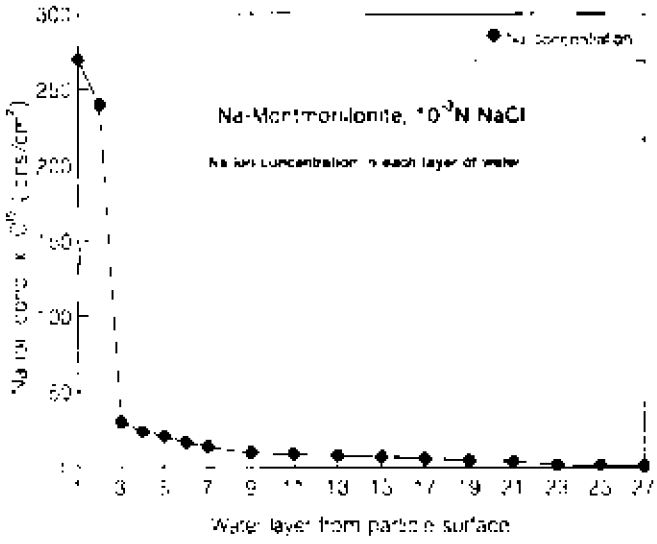

FIG. 8. Na ion concentration distribution in Na-montmorillonite clay (from Alammawi 1989).

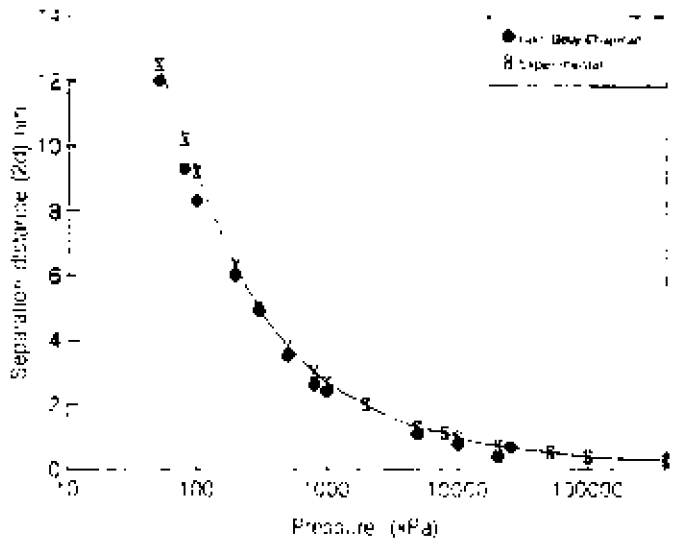

FIG. 9. Particle separation distance, volumetric water content, and swelling pressure for Na-montmorillonite clay with added interaction energy in the Stern layer. Corr. Gouy–Chapman, corrected by addition of hydration energies of interaction to Gouy–Chapman DDL model.

from 10 to 20% of the potential energy due to the ion–dipole interaction when the number of absorbed water molecules is 3–6, according to the following relationship: reduction $= D_a(\mu^2/\xi r^3)$. The geometrical factor D_a is given as 0.344 and 1.188 for 3 and 6 water molecules adsorbed by ion, respectively. In the calculations used to modify the Gouy–Chapman model, a reduction factor of 20% of the energy due to ion–dipole interaction was used to calculate the dipole interaction energy E_{dd}, on the assumption that any Na^+ ion could be surrounded by up to six water molecules, i.e., $E_{dd} = 0.2E_{id}$.

The values for dipole-site interaction energy E_{di} may be calculated as

$$[17] \quad E_{di} = \frac{\mu\,\epsilon}{\xi\, r_i^2}$$

where r_i is the distance between the centre of the dipole and the negative site. The relationship for E_{oh} can now be obtained as the summation of all the interaction energies heretofore considered, i.e., $E_{oh} = E_c + E_{id} + E_{dd} + E_{di}$. Accordingly, with this total interaction energy relationship and the expression given for E_{ih} given in terms of E_c, the term $(E_{oh} - E_{ih})$ can now be evaluated. In addition, ψ_{oh} can be calculated as follows: (*i*) calculating σ_p from the known CEC and S_a, i.e., $\sigma_p = CEC/S_a$; and (*ii*) substituting [12] and [15] into [13]; the only unknown parameter is ψ_{oh}, which can be obtained after substitution of the equations.

At this juncture, it should be noted that to calculate the diffusion coefficient given in [3], the osmotic potential ψ_π (where $\psi_\pi = \psi_{oh}$) needs to be considered in calculating the total soil-water potential ψ.

The concentration of ions at the OHP can be computed from the Boltzmann relationship:

$$[18] \quad n_{i,oh} = n_{i\infty} \exp\left(\frac{-z_i e \psi_{oh}}{\kappa T}\right)$$

The values for $n_{i,h}$ and $n_{i,oh}$ have been calculated by Alammawi (1988) for the Na-montmorillonite clay used in the high-pressure consolidation test, using [15] and [18] to give the distribution of Na^+ shown in Fig. 8.

To calculate the distribution of the electric potential ψ_i at any point x_i, distant from the surface of the charged particle, the following conditions are used in the integration:

$$\psi \to 0 \text{ and } \frac{d\psi}{dx} \to 0 \qquad \text{for } x \to \infty$$

and

$$\psi = \psi_{oh} \qquad \text{for } x = \Delta x$$

at the OHP. The final relationship obtained takes the form similar to the one given by Kruyt (1952):

$$[19] \quad \chi x_i = \ln \frac{\left[\exp\left(\frac{z_i e \psi_i}{2\kappa T}\right) + 1\right]\left[\exp\left(\frac{z_i e \psi_{oh}}{2\kappa T}\right) - 1\right]}{\left[\exp\left(\frac{z_i e \psi_i}{2\kappa T}\right) - 1\right]\left[\exp\left(\frac{z_i e \psi_{oh}}{2\kappa T}\right) + 1\right]}$$

where ψ_i is the potential at a distance x_i from the surface of the charged particle. The term χ is written as

$$[20] \quad \chi = \left(\frac{4\pi e^2 \sum n_{i\infty} z_i^2}{\xi \kappa T}\right)^{1/2}$$

To determine whether the relationship describing ψ_{oh} is valid, recalling that this pertains to the potential at the OHP, the experimental values for the pressure-particle space shown in Fig. 6 need to be compared with the calculations obtained using the energies of interaction developed for the number of ions in the IHP and OHP. The number of cations for each water layer away from the Na-montmorillonite surface has been calculated by Alammawi (1989) using the model given herein (Fig. 8). As observed, the concentrations of cations in the first layer ($n_{i,ih}$) and the second layer ($n_{i,oh}$) are significantly higher than those in the Gouy layer. The high concentration of cations is indicative of the resultant

increase in the soil-water potential ψ at close separation distances between particles.

In the calculations of the swelling pressure using the Gouy–Chapman model, the addition of the energies of interaction within the Stern layer (presented by the IHP and OHP) to the values calculated with the Gouy–Chapman model shown in Fig. 6 will add more swelling pressure of the same particle separation distance. The calculated values with the additional energies of interaction at the IHP–OHP can be seen in Fig. 9. The comparison between experimental and calculated value shows good accord, indicating thereby the merit of incorporating the potential as determined in accord with the Grahame modification of the Stern layer (arrangement B in Fig. 7). The results suggest very strongly that the determination of the diffusion coefficient in [3] should recognize the specification of ψ in the equation, i.e., to be cognizant of the contribution from the Stern layer. It is further suggested that the fluid-transport diffusion coefficient D in the stage I wetting process (van Olphen 1977), where the considerable energies of interaction are developed in hydration (the same region referred to by Ninham (1981) as the region dominated by surface-induced liquid structure), will not be accurately portrayed if the potentials developed at IHP and OHP (ψ_{ih}, ψ_{oh}) are not incorporated into the analyses considered in [3]. Continued work is necessary to combine the sets of results obtained in this two-part study to better evaluate the impact of these potentials on D.

Concluding remarks: implication for soil wetting

The close correspondence between the calculated values using the energies of interaction in the IHP–OHP as additional to the standard Gouy–Chapman model calculations shows that the ψ_{oh} term can be used to provide a measure to the swelling pressure component that needs to be accounted for in measurements of constrained wetting of expansive soils. The manner in which such calculations should be incorporated into analyses of results for wetting of expansive soils is currently under study. Specifically, the hydration forces that are responsible for the hydration energies of interaction in the stage I wetting process referred to by van Olphen (1977) would need to be studied in relation to the swelling pressure test results obtained. Central to any theoretical or experimental development is the need for improvement in the measurement of swelling pressures at the wetting front in the infiltration–wetting experiments to assure that the swelling-pressure measurements obtained reflect the actual swelling pressure developed at the wetting front. In the meantime, research into the wetting performance of expansive soils will need to determine the wetting characteristics of the soils and the related volume expansion during wetting, with the hope that computations of the various interaction energies developed and corresponding volume change can be correlated with the measured soil wetting results.

Acknowledgements

This study was supported by grants in aid of research from the Natural Sciences and Engineering Research Council of Canada to RNY (grant A-882) and AMOM (grant PGPOO46418). The expansive soil wetting experiments were conducted by H.Y. Wong, and the high-pressure consolidation experiments were conducted by A.M. Alammawi. The authors wish to record their considerable appreciation to the two reviewers. The constructive critical review and comments regarding additional points for consideration, given by the two reviewers, have contributed greatly to the revision and improvement of the paper.

Alammawi, A.M. 1989. Some aspects of hydration and interaction energies of montmorillonite clay. Ph.D. thesis, Civil Engineering Department, McGill University, Montréal, Que.

Barclay, L., Harrington, A., and Ottewill, R.H. 1972. The measurement of forces between particles in disperse systems. Kolloid Zeitschrift & Zeitschrift fuer Polymere, 250: 655–666.

Bockris, J.O'M., and Reddy, A.K.N. 1970. Modern electrochemistry. Vol. 2. Plenum Press, New York.

Bohn, H.L., McNeal, B.L., and O'Connor, G.A. 1979. Soil chemistry. John Wiley & Sons, Inc., New York.

Bolt, G.H. 1956. Physico-chemical analysis of compressibility of pure clays. Géotechnique, 6: 86–93.

Chabbra, R., Pleysier, J., and Cremers, A. 1975. The measurement of cation exchange capacity and exchangeable cations in soils. A new method. Proceedings, International Clay Conference, Mexico City, pp. 439–449.

Eltantawy, I.N., and Arnold, P.W. 1973. Reappraisal of ethylene glycol mono-ethylether (EGME) method for surface area estimation of clays. Journal of Soil Science, 24: 232–238.

Grahame, D.C. 1947. The electric double layer and the theory of electrocapilarity. Chemical Reviews, 41: 441–501.

Israelachvili, J.M. 1982. Forces between surfaces in liquids. Advances in Colloid and Interface Science, 16: 31–47.

Kruyt, H.R. 1952. Colloid science. Elsevier, New York.

Ninham, B.W. 1972. Surface forces—the last 30 Å. Pure and Applied Chemistry, 53: 2135–2147.

Pashley, R.M. 1981. DLVO and hydration forces between mica surfaces in Li^+, Na^+, K^+, and Cs^+ electrolyte solutions: a correlation of double layer and hydration forces with surface cation exchange properties. Journal of Colloid and Interface Science, 83: 531–546.

Philip, J.R., and Smiles, D.E. 1969. Kinetics of sorption and volume changes in three-component systems. Australian Journal of Soil Research, 7: 1–19.

van Olphen, H. 1977. An introduction to clay colloid chemistry. 2nd ed. John Wiley & Sons, Inc., New York.

Waidelich, W.C. 1958. Influence of liquid and clay mineral type on consolidation of clay liquid system. Highway Research Board, Special Report 40, pp. 24–42.

Warkentin, B.P., and Schofield, R.K. 1952. Swelling pressure of Na-montmorillonite in NaCl solutions. Journal of Soil Science, 13: 98–103.

Yong, R.N. 1984. Particle interaction and stability of suspended solids. Proceedings, ASCE Symposium on Sedimentation/Consolidation Models: Predictions and Validation, San Francisco, Calif., pp. 30–59.

Yong, R.N., and Warkentin, B.P. 1975. Soil properties and behaviour. Elsevier, Amsterdam.

Yong, R.N., Taylor, L.O., and Warkentin, B.P. 1963. Swelling pressure of sodium montmorillonite at depressed temperatures. Proceedings, 11th National Conference on Clays and Clay Minerals, August 13–17, 1962, Ottawa, Ont., pp. 268–281.

Zaslavsky, D. 1964. Saturated and unsaturated flow equation in an unstable porous medium. Soil Science, 98: 317–321.

Influence of amorphous silica and iron hydroxide on interparticle action and soil surface properties

R. N. YONG AND A. M. O. MOHAMED

Geotechnical Research Centre, McGill University, 817 Sherbrooke Street West, Montréal, Que., Canada H3A 2K6

AND

B. W. WANG

Geocon Inc., 3210 American Drive, Mississauga, Ont., Canada L4V 1B3

Received January 27, 1992

Accepted May 20, 1992

The study of the physicochemical properties of pure amorphous materials (complexes) consisting of Fe_2O_3 and SiO_2 in various proportions indicates that the amorphous complexes will exhibit different properties and characteristics depending on the proportions of Fe_2O_3 and SiO_2. Addition of the amorphous complexes with illitic clay studied shows that the properties of the clay admixture will also vary according to the properties of the amorphous complex, albeit to a lesser degree. The properties and behaviour observed for the amorphous complexes and the clay admixtures can be linked directly to the large specific surface area and high surface charge of the amorphous complexes. The contribution of amorphous complexes to the clay – amorphous complex mixtures (clay admixtures) is twofold: firstly, by the amount of amorphous complex in the clay admixture, and secondly by the composition of the amorphous complex used. The contribution from the amorphous complex is in two forms: water-holding capacity and bonding action. The presence of pH-dependent surface charges associated with the amorphous complexes makes the physicochemical properties and behaviour of the clay admixtures (e.g., liquid limits and zeta potential) sensitive to the pH environment. Coating of amorphous colloids onto clay particle surfaces, shown by scanning electron microscopy, appears to be enhanced by a decrease in pH of the system, indicating that the enhancement is likely due to the increased electrostatic attraction resulting from the increased amounts of positive charges on the amorphous colloids.

Key words: amorphous materials, mass ratio, zeta potential, Bingham yield stress, clay admixtures, hydrogen bonding, specific surface area, cation exchange capacity, anion exchange capacity, fabric and soil structure.

L'étude sur les propriétés physicochimiques de matériaux amorphes purs (complexes), constitués de Fe_2O_3 et de SiO_2 en proportions diverses, indiquent que les complexes amorphes vont présenter différentes propriétés et caractéristiques dépendant des proportions de Fe_2O_3 et de SiO_2. L'addition des complexes amorphes à l'argile illitique étudiée montre que les propriétés de l'admixtion d'argile vont aussi varier selon les propriétés du complexes amorphe, quoiqu'à un degré moindre. Les propriétés et le comportement observé pour les complexes amorphes et les admixtions d'argile peuvent être reliés directement à la valeur élevée de surface spécifique et à la forte charge de surface des complexes amorphes. La contribution des complexes amorphes aux mélanges argile-complexe amorphe (admixtions d'argile) est double: premièrement, par la quantité de complexe amorphe dans l'admixtion d'argile, et deuxièmement, par la composition du complexe amorphe utilisé. La contribution du complexe amorphe se présente sous deux formes: la capacité de retention d'eau et la production de liens. La présence des charges de surface, dépendantes du pH, associées aux complexes amorphes, rend les propriétés physicochimiques et le comportement des admixtions d'argile (i.e., limites liquides et potentiel zêta) sensibles à l'environnement de pH. L'enduisage de colloïdes amorphes sur les surfaces des particules argileuses, mis en évidence par la microscopie électronique à balayage, semble être amplifié par une diminution de pH dans le système, indiquant que cette amplification est vraisemblablement due à l'augmentation de l'attraction électrostatique résultant des quantités croissantes de charges positives sur les colloïdes amorphes.

Mots clés : matériaux amorphes, rapport de masse, potentiel zêta, contrainte limite de Bingham, admixtions d'argile, liens d'hydrogène, quantité de surface spécifique, capacité d'échange de cations, capacité d'échange d'anions, fabrique et structure du sol.

[Traduit par la rédaction]

Can. Geotech. J. 29, 803–818 (1992)

Introduction

Speculation on the presence of amorphous materials in the marine clays of Eastern Canada (Conlon 1966; Quigley 1968) led to several later studies by many researchers (e.g., Loiselle *et al.* 1971; McKyes *et al.* 1974; Hendershot and Carson 1978; Quigley 1980; Locat *et al.* 1984) which confirmed the existence of such materials and that the three major components were amorphous silica, iron, and alumina. These components are believed to exist in the chemical forms of hydroxides and (or) oxides. Interest in the control exercised by the presence and concentration of these amorphous materials has resulted in several studies designed to examine several aspects of soil properties and behaviour, ranging from basic material characterizations to material performance and properties. Beginning with the reporting of presence of the amorphous materials in the marine clays, the early study of bonding or cementing established by amorphous materials, using EDTA (ethylenediaminetetraacetic acid) as a leaching solution (Loiselle *et al.* 1977), was followed by studies of distribution and of the development of physical and mechanical properties (e.g., Yong *et al.* 1979*a*, 1979*b*; Haynes and Quigley 1976; Locat *et al.* 1984; Torrance 1987).

In attempting to determine the contribution of amorphous materials to soil properties and behaviour, attention has been

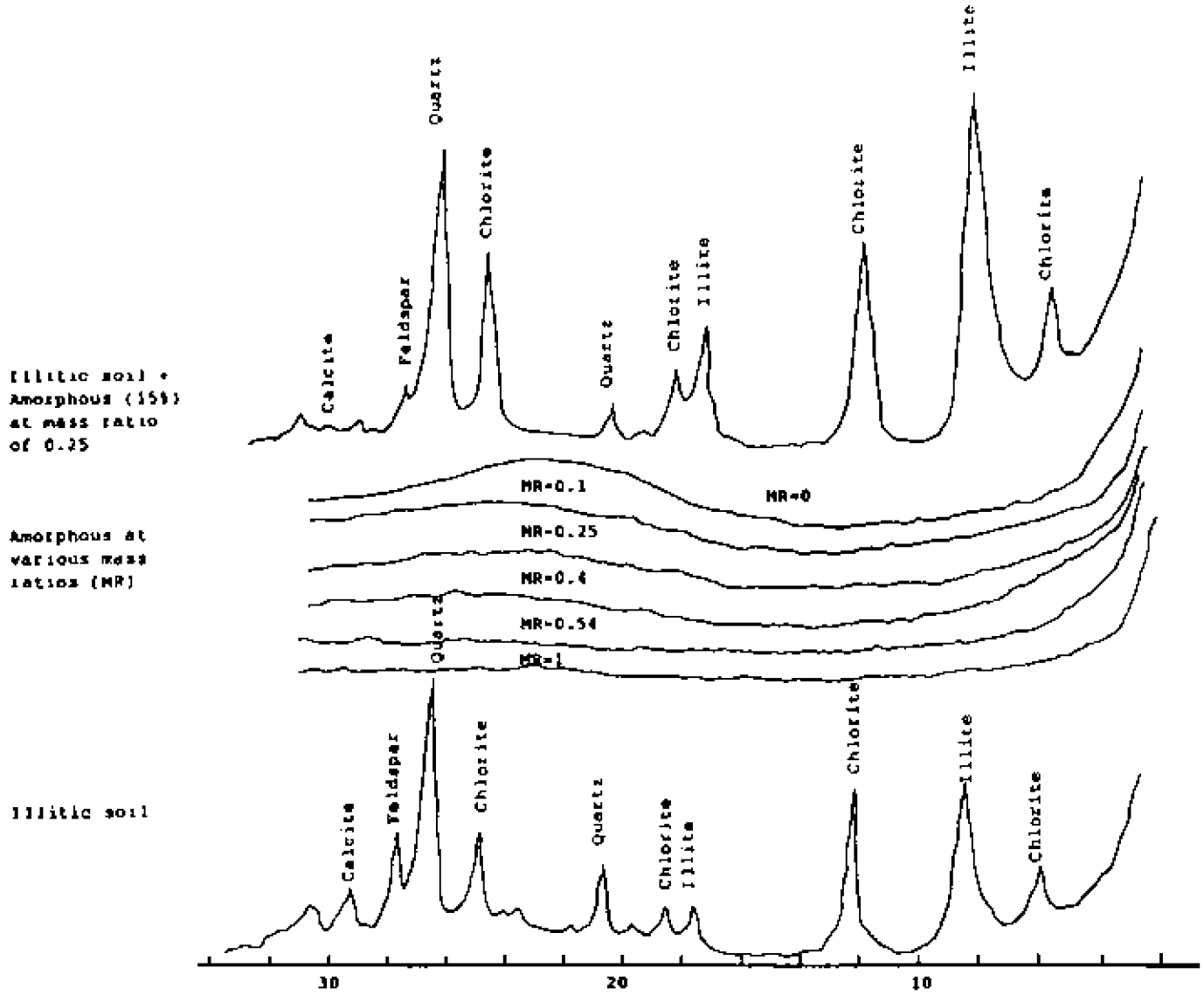

FIG. 1. XRD patterns of illite, soil, amorphous material, and admixtures.

given by many researchers (e.g., Haynes and Quigley 1976; Bentley and Smalley 1978, 1984; Yong *et al.* 1977, 1979, 1980; Quigley 1980, 1983; Locat *et al.* 1984; Yong and Ohtsubo 1987; Torrance 1987) to the thesis that the amorphous materials (*i*) form coatings on soil particle surfaces (deduced from scanning electron micrographs and from enhancement of X-ray peak intensities upon removal of the amorphous materials), and (*ii*) form bonds between clay particles. However, the exact type of bonding and the extent or strength of the bonds formed have not been fully established or definitely defined.

In addition to the interest in the role of amorphous materials in control of soil properties and behaviour, the recent imperative concern regarding the use of clay soil as an engineered barrier for containment of land disposal of wastes has focussed attention on the surface properties of the soil solids in the clay-engineered barrier. The manner in which clay soils accomplish accumulation of contaminants and control transport processes has been described in many reference texts (e.g., Bolt and Bruggenwert 1978; Fuller and Warrick 1985; Greenland and Hayes 1981). Adsorption of cations by clay soils results from the negative surface charges that are characteristic of many layer-lattice minerals. Amorphous materials possess high specific surface areas and high ion-exchange capacities. The surfaces of amorphous materials, as far as the charge is concerned, are dependent on pH and electrolyte concentration in the surrounding medium. The charge arises from association or dissociation of protons and may be represented by

$$M\text{-}OH_2^+ \underset{\text{more acid}}{\overset{H^+}{\rightleftharpoons}} M\text{-}OH \underset{\text{more alkaline}}{\overset{OH^-}{\rightleftharpoons}} M\text{-}O^- + H_2O$$

where M represents a coordinated amorphous ion. The extent of association or dissociation of protons is determined by the concentration of protons near the surface, and hence by pH electrolyte concentration of the soil pore fluid. The pH at which the surface is unchanged is known as the zero point of change (ZPC). It depends primarily on the affinity of the amorphous ions for electrons. The charge reversal of the amorphous material, due to changes in the pH of the soil system in relation to the ZPC pH, will create or affect bonding situations consistent with the changes in the sign

TABLE 1. Mineralogical and chemical composition of soils and amorphous materials used in the study

Composition	Illitic soil	Amorphous material at mass ratio[a] of					
		0.00	0.10	0.25	0.40	0.54	1.00
Crystalline minerals	Quartz, feldspar, calcite, illite, chlorite	—	—	—	—	—	—
Amorphous content (%)							
SiO_2	2.1	100	90	75	60	46	0
Fe_2O_3	3.6	0	10	25	40	54	100
Al_2O_3	1.1	0	0	0	0	0	0
Total	6.8	100	100	100	100	100	100
Organic content (%)	0.2	—	—	—	—	—	—
Cation concentration (mequiv./100 g)							
K^+	2.8	nd	18.8	6.8	4.4	1.2	nd
Na^+	8.4	nd	148.0	184.0	215.6	204.0	nd
Ca^{2+}	65.5	nd	21.2	13.2	23.2	17.2	nd
Mg^{2+}	3.2	nd	1.8	1.8	0.3	0.6	nd

NOTE: nd, not determined.
[a]Mass ratio = $Fe_2O_3/(Fe_2O_3 + SiO_2)$.
[b]Determined by Segalen's (1968) technique for soils.
[c]Cation concentration = soluble + exchangeable.

of the surface charges (Yong and Ohtsubo 1987). Since amorphous oxides and hydroxides in the presence of water have a reduced coordination number in their surface layers, they develop hydroxylated surfaces with a net negative charge at high pH. This results in adsorption of cations at any pH higher than that of the ZPC pH. The adsorption occurs before overall precipitation takes place, saturating the surface sites. On the other hand, for pH values less than the ZPC pH, the surfaces become positively charged due to adsorption of protons in excess of that for hydroxyl ions, and hence adsorption of anions at the surface will be achieved. The magnitude of charge increases with the increase in ionic strength at any given pH below the ZPC. In these circumstances the positive charge is located on the inner Helmholtz layer, with the balancing anion located within the other Helmholtz layer or the diffuse double layer. Such adsorption is termed nonspecific. Furthermore, organic anions can penetrate the coordination shell of the amorphous surface of the hydroxide. The anion is thus incorporated with the surface hydroxyl layer. This process is not sensitive to electrolyte concentration but is sensitive to pH.

It is useful to note that, whereas the record shows (Yong and Rao 1991) that because of their hydrophilic surfaces, clay soils are usually not good adsorbents for non-water-soluble organics, the existence of organic matter in clay soils enhances its adsorption capability for non-water-soluble organics. Recent studies have focussed on the modification of clays to create so-called organo-clays (Boys *et al.* 1988*a*, 1988*b*; Yong and Rao 1991) that utilize macromolecules in developing bonding with organics. Present perception of contaminant–soil interaction suggests that clay soils which contain some amorphous materials would enhance sorption of contaminant solutes. To provide a better understanding of the contribution of amorphous materials to the performance of clay soils, this study examines the effect of amorphous material composition and concentration in combination with an illite soil on some selected surface properties of the soil mixture. To achieve control of the composition of the amorphous material, synthesized amorphous silica and iron hydroxide are used. In addition to the determination of the combinations necessary to obtain maximum adsorption capacity, the physicochemical properties of the soil mixture are examined as a function of pH, and particle interactions in the soil mixture are assessed with the aid of infrared spectrometry, electron microscopy, surface area measurements, determination of both cation and anion exchange capacities, and zeta potential.

Materials and methods

Illite soil

The control soil was a pulverized marine shale (Ordovician sedimentary rock), obtained commercially and identified as Domtar Sealbond silty clay. The procedures for determination of composition and properties of the illite soil (and the amorphous materials) will be given in a later section.

Synthesized amorphous materials

Since natural amorphous material was not readily available for the purpose of this study, laboratory-prepared amorphous materials were used. To maintain a simple system, only two components were used, i.e., amorphous silica and iron hydroxide. Inasmuch as amorphous silica and iron hydroxide possess different properties (Yong *et al.* 1979*b*, 1980), accountability for composition or type of amorphous material was achieved by using the mass ratio (MR) concept (Yong *et al.* 1980), defined as the ratio of amount of amorphous iron to the sum amount of iron and silica in the form of oxides and in units of mass, i.e., $(Fe_2O_3/(Fe_2O_3 + SiO_2))$. Thus, an MR value of zero indicates that the amorphous material consists solely of silica, whereas a value of 0.40 indicates that 40% of the amorphous material consists of Fe_2O_3. For simplicity in presentation and discussion of results, the pure amorphous silica and iron hydroxide as mixtures will be referred to as amorphous complexes. Reference to amorphous material will be made, when required, to avoid confusion. As reported previously (Yong *et al.* 1980), a change in the MR in effect changes the composi-

TABLE 2. Basic geotechnical and physicochemical properties of soils and synthesized amorphous materials

	ASTM test (1989)	Illitic soil	Synthesized amorphous material (fresh) at mass ratio of					
			0	0.10	0.25	0.40	0.54	1
As is water content (%)	D2216-80	0.8	1680.1	1541.6	918 0	380.0	402.6	732.1
Consistency limits								
Liquid limit (%)	D4318-84	34.0	847.6	770.2	451.3	180.1	214.8	364.5
Plastic limit (%)		21.4	402.2	355.0	186.3	112.5	123.1	219.0
Plasticity index (%)		12.6	445.4	415.2	264.6	67.6	91.7	145.5
Flow index		6.0	580.0	528.6	136.4	20.2	54.2	179.9
Grain size								
D_{50} (μm)	D422-63	5.0	nd	nd	nd	nd	nd	nd
D_{10} (μm)		0.4	nd	nd	nd	nd	nd	nd
C_u[1]		20.3	nd	nd	nd	nd	nd	nd
C_c[2]		3.1	nd	nd	nd	nd	nd	nd
pH	nd	7.9	8.0	8.0	8.0	8.0	8.0	8.0
Specific surface area (m^2/g)	nd	88.8	786.1	730.3	639.7	498.8	564.9	677.0
Cation exchange capacity (mequiv./100 g)	nd	16.0	54.9	61.5	71.2	82.0	63.4	8.0

NOTES: C_u, uniformity coefficient (D_{60}/D_{10}); C_c, coefficient of curvature ($D_{30}^2/D_{10} \cdot D_{60}$); nd, not determined.

tion or type of amorphous material and can result in corresponding changes in the soil properties.

To synthesize amorphous silica and iron hydroxides, as well as their mixtures of varying composition, the precipitation technique developed by Herbillon and Tran Vinh An (1969) was employed. A predetermined MR was obtained by mixing together precalculated volumes of $FeCl_3 \cdot 6H_2O$ (0.05 M) and $Na_2SiO_3 \cdot 9H_2O$ (0.05 M) slowly in a beaker. The pH of the mixed solutions was brought to 8 by adding either diluted HCl or NaOH with gentle stirring for a week. In the cases where the MR was 0 or 1, corresponding respectively to pure amorphous silica or pure iron, only the pH adjustment was necessary. Following 1 week of gentle stirring, when the amorphous complex had grown sufficiently large in particle size without being crystallized, the complex was repeatedly filtered and washed with distilled water to remove free salts in the suspension. Repeated filtering and washing was terminated when the NaCl concentration was lowered to 10^{-4} M. The amorphous complex thus obtained was in the form of a gel and was used without being allowed to air-dry.

Visual description of synthesized amorphous material (complex)

All the amorphous complexes were synthesized in the same manner. The following is a visual description of the amorphous complexes in the wet state (i.e., as used in the experiments) with different MRs using the revised Standard Colour Chart by Oyama and Takehara (1976): (*i*) MR = 0: white (an opaque off-white gel); (*ii*) MR = 0.10: pale yellow (an opaque pale yellow gel); (*iii*) MR = 0.25: yellow (an opaque yellow gel); (*iv*) MR = 0.40: bright yellowish brown (a yellowish brown gel); (*v*) MR = 0.54: bright brown (a brown gel); (*vi*) MR = 1: dark reddish brown (a dark reddish brown gel). As noted, the colour changes from white to yellow, and then to brown, as the MR varies from 0 to 0.25, and then to 1. The opacity is reduced as the MR increases, i.e., as the iron content increases.

Mineralogy and composition

Mineralogical analysis of the illite soil, amorphous material, and their admixtures was obtained through X-ray diffraction (XRD) studies, using a Siemens D500 apparatus with CuKα radiation. Oriented slides were obtained after drying a suspension (1.0% solid) of dried and pulverized sample mixed with distilled water. For amorphous materials, a specimen was prepared from approximately 3 g of wet gel, which was spread on an XRD slide and subjected to air-dying. The XRD results (diffractograms) for illite soil, amorphous materials, and admixtures are presented in Fig. 1. Since, by definition, amorphous materials do not exhibit crystalline features, XRD studies were nevertheless conducted on the laboratory amorphous materials to confirm the absence of crystalline material, as demonstrated by the diffraction patterns shown in Fig. 1. As indicated by the XRD results, the illite soil is composed mainly of quartz and feldspar as primary minerals with illite and chlorite as clay minerals.

As expected, the admixtures of amorphous complexes with illitic soil show no alteration of XRD peak positions of various crystalline minerals in comparison with those before addition of amorphous complexes. More specifically, these data indicate that the addition of amorphous complex neither changes the crystalline composition nor forms a new species of minerals with the clays. However, the peak intensities of some minerals are more or less reduced, due probably to amorphous complex coating to clay minerals (McKyes *et al.* 1974). Since it has been suggested that amorphous iron hydroxide may gradually transform into a crystalline substance, namely hematite and (or) goethite upon aging under neutral pH conditions (Gastuche *et al.* 1964), the XRD technique was also used to monitor any transformation of amorphous complex into crystalline matter during "aging" tests.

A trace amount of organic matter of about 0.25 was detected in the illite soil, using the hydroperoxide oxidation technique (Jackson 1967). The amorphous materials deter-

mined according to Segalen's (1968) technique, for the illitic soil, were as follows: SiO_2 – 2.1%, Fe_2O_3 – 3.6%, and Al_2O_3 – 1.1%, for a total amorphous material content of 6.8% by weight. It is recognized that it is difficult to identify and, hence, isolate the effect of this initial amorphous material present, since removal of the amorphous components by selective dissolution techniques may cause alteration of pore-fluid chemistry and perhaps some dissolution of the solid material constituents. Accordingly, quantitative values given are to be taken in the context of the method used and are useful only with respect to a relative comparison of concentrations of the various constituents. This does not apply to the laboratory-prepared amorphous silica or iron hydroxide inasmuch as these were prepared as described in the preceding section.

Cation concentrations (soluble and exchangeable) in the pore fluid, replaced by a silver-thiourea complex (Chhabra *et al.* 1975), were determined using an atomic absorption spectrometer. The synthesized amorphous materials show sodium concentrations higher than the other cations, as indicated in Table 1. This could be attributed to the complexation of sodium and hydroxylated surfaces during the preparation of the synthesized amorphous material; hence, the adsorbed sodium could not be washed off by distilled water during the synthesizing process. The mineralogical and chemical composition of the soils and amorphous complexes used in the study is summarized in Table 1.

Zeta potential measurement

Detailed information regarding the zeta potential measurement and its concept is given in Appendix. The zeta potential of the soils, amorphous complex, and their admixtures was determined with the aid of a zeta meter and application of the Helmholtz-Smoluchowski equation (Heimenz 1977). Only a minute quantity of specimen was required to prepare a very dilute suspension (about 0.02% solids concentration). Several agitations were necessary to break down the soil flocs, followed by a quiescent period to allow the samples to equilibrate with the buffering solutions (i.e., variations of solutions pH from 2 to 10).

Viscosity and Bingham yield stress determination

For viscosity and Bingham yield stress tests, the solids concentration of the test samples consisted of 5% amorphous complexes for tests on these materials. In tests on the illite soil and admixtures with amorphous complexes, the solids concentration for the test samples consisted of 10% soil solids (or soil admixtures). The test samples (suspensions) were well shaken to ensure uniformity and allowed to equilibrate for a period of 24 h before determination of the flow characteristics of the samples. The viscosity values of the samples were measured using a rotating cylindrical viscometer (Contraves Rheomat 15), capable of 15 different shear rates increasing in geometric progression. The shear stress was calculated through measurements of the torque required to maintain a given shear rate, and the Bingham yield stress obtained from the shear rate curve was used as an indicator of the flow behaviour of the material.

Infrared spectrometry (IR) study

The samples were prepared by mixing one part soil, or amorphous complex or admixture, with 10 parts of buffering material (potassium bromide, KBr). Following mixing, manual grinding was carried out in a mortar until the mixture had turned into a very fine powder. The powder, containing 10% soil sample, was compressed to approximately 70 000 kPa by a compressor to obtain a thin-section specimen. A blank sample (pure KBr) was also tested as "background" along with the other samples. The infrared spectrometric patterns were obtained using an infrared spectrophotometer (model ACCULAB manufactured by the Beckman Company). To minimize the effect of moisture adhering to the soil samples, the samples were kept in a desiccator prior to testing.

Scanning electron microscopic (SEM) study

A JVC T300 scanning electron microscope was used to observe the microstructure of the soil – amorphous complex admixtures. The air-dried samples from about 1:1000 (solid: liquid) concentration suspension were coated with carbon and subsequently with gold–palladium as required for the SEM examination. A very small amount of soil and (or) amorphous complex was obtained from the previously prepared and equilibrated samples for immersion in a beaker containing distilled water at a pH preadjusted to 8 by adding NaOH or HCl. One drop of this suspension was pipetted and placed onto the SEM sample stud for air-drying before coating with carbon and gold–palladium.

For suspensions containing samples from molded soils, continuous agitation was performed for about 5 min to ensure that complete disruption of soil structural bonding was obtained. All of the soil samples were aged for approximately 3 months in a humid room prior to preparation for the SEM tests. The magnification for SEM tests was selected at 15 000 × based on the results of several examinations of samples.

Results and discussion

Geotechnical and physicochemical properties

Table 2 presents the test results of some basic geotechnical and physicochemical properties for illite soil and amorphous complexes pertinent to this study. The water content, consistency limits, and grain-size distribution were determined using the ASTM (1989) standard methods as stated in Table 2. Hydrometer tests for evaluation of grain-size distribution of the amorphous complexes (present in the form of gel) could not be undertaken because of the tendency for flocculation of the complexes almost immediately after blending. This phenomenon is not unexpected in view of the strong attractive forces present within the amorphous complex. The addition of a dispersing agent did not achieve the expected dispersion of the amorphous complex, due perhaps to the counterreaction of the variable charged surfaces of the material. The specific surface area values were measured using the ethylene glycol monoethyl ether (EGME) retention technique (Eltantawy and Arnold 1973). The cation exchange capacity (CEC) was determined at a pH of 7 with a silver-thiourea complex as a cation-replacing agent (Chhabra *et al.* 1975).

As noted from Table 2, the synthesized amorphous complexes showed varying values of consistency limits depending on the MR. This can be observed, for example, in the vast difference in the liquid-limit values. The liquid limit decreases from 847.6 to 180.1% and subsequently increases to 364.5% as the MR of the amorphous complex varies from 0 to 0.40 and thereafter to 1. An apparent critical point exists at an MR of 0.40, where the liquid and plastic limits exhibit

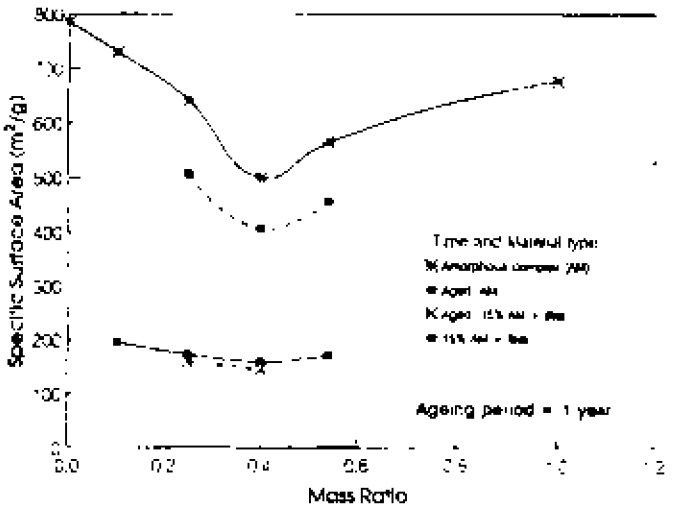

FIG. 2. Specific surface area – mass ratio relations.

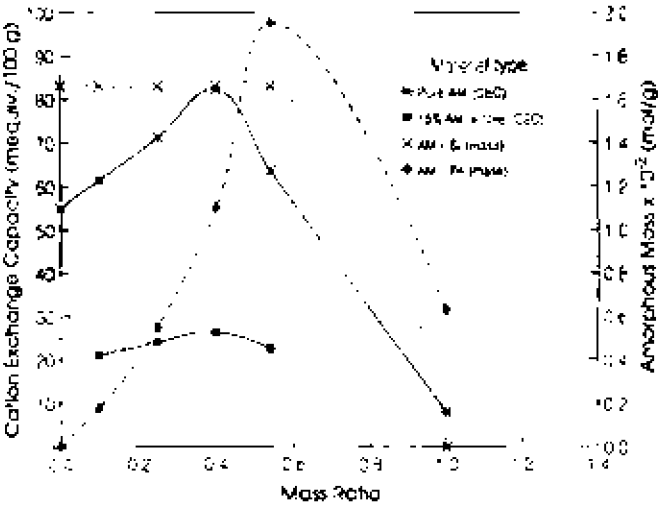

FIG. 3. Cation exchange capacity – mass ratio relations.

minimum values. As might be expected, the specific surface areas of the amorphous complexes vary in the same manner as their consistency limits, inasmuch as the consistency properties are controlled by the surface area of the amorphous complexes. Table 2 shows that a minimum value of specific surface area is obtained at an MR of 0.40, corresponding to the minimum values of consistency limits. The CEC of the amorphous complexes attains its maximum value at an MR of 0.40, in contrast with the specific surface area measurements and consistency limits, which are at a minimum at 0.40. As will be noted in the discussions to follow, whereas this might appear to be inconsistent with initial expectations, the recent studies on isomorphous substitutions in amorphous complexes reported by Cloos *et al.* (1986) and Decareau *et al.* (1987) suggest that these substitutions are responsible for the observed behaviour.

Specific surface area

The results portrayed in Fig. 2 show that the specific surface area (SSA) of freshly prepared amorphous complexes varies from 790 m^2/g for the pure silica (MR = 0) to 670 m^2/g for the pure iron (MR = 1), with a minimum value of about 500 m^2/g for the mixed iron hydroxide and amorphous silica at MR = 0.40, indicating the surface-area dependency on amorphous material composition. As comparative values, it is noted that the SSA for a pure Na-montmorillonite clay is approximately 800 m^2/g, whereas the SSAs for kaolinitic and illitic soils are about 15 and 80 m^2/g, respectively, which in turn suggests that the amorphous material has a SSA close to that of Na-montmorillonite. Furthermore, it is known that the higher the surface area, the greater the number of available sites for chemical interactions; hence, more attenuation capacity. The variation of SSA of the amorphous complex with mass ratio exhibits a V-shaped curve, very similar to that shown for the consistency limits. The same type of relationship is also observed for the admixtures composed of amorphous complex and illitic soil.

The variable SSA measured as a result of variation of mass ratio of the amorphous complex suggests that the combination of Si and Fe during formation of the amorphous complex is not necessarily a simple matter of physical mixing, but rather a more complicated procedure that also involves chemical interaction. The minimum value of SSA at MR = 0.40 suggests the formation of larger particle sizes for the amorphous complexes and the admixtures. This would be consistent with the observation of minimum values for the plastic and liquid limits found at MR = 0.40, inasmuch as low water-holding capacities are indicative of low SSAs.

On the other hand, since the molecular weight of SiO_2 is less than that of Fe_2O_3, the proportionality in the mass of each component is different for each MR. For example, at MR = 0.1, the mass of SiO_2 = 0.0166 mol/g of soil and the mass of Fe_2O_3 = 0.00184 mol/g of soil, whereas at MR = 0.4, the mass of SiO_2 is the same as for MR = 0.1, but the mass of Fe_2O_3 = 0.011 mol/g of soil. This in turn indicates that at MR = 0.4, equal mass of SiO_2 and Fe_2O_3 is present in the complex mixture; hence, maximum substitution of Si^{4+} by Fe^{3+} and optimum surface area of the composition are obtained.

Tests on the illitic soil and admixtures of the soil and amorphous complexes aged in a humid room for 1 year showed that the SSA of the illitic soil was similar to the "un-aged" soil (SSA of about 89 m^2/g). However, as shown in the check samples in Fig. 2, a marked reduction in the SSA occurred for the amorphous complex. The ageing effect on the admixtures is not considered significant for the percentage of amorphous complex used in the admixture. However, it is expected that, if the amorphous complex is increased to values significantly above 15% of the mixture, the ageing effect would be noticeable. It is not immediately clear as to the direct cause of the reduction of SSA other than a "thixotrphic" or aggregation effect leading to an increase in amorphous complex particle size. This will be examined in a later section in the discussion provided in support of the SEM study.

Cation and anion exchange capacities (CEC and AEC)

Using the cation exchange capacity (CEC) and anion exchange capacity (AEC) as indicators of the capability of the soil admixtures to provide interaction with the indifferent ions, i.e., ions that interact in the diffuse double layer and have the ability to influence the magnitude on the zeta potential. Since the CEC and AEC values of a soil mass represent the surface negativity and positivity, respectively, the CEC

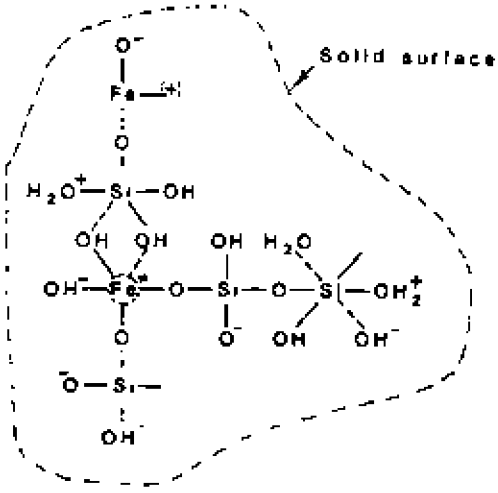

FIG. 4. Schematic representation of molecular structure of silica-iron mixed amorphous complex. *, Si substituted for Fe.

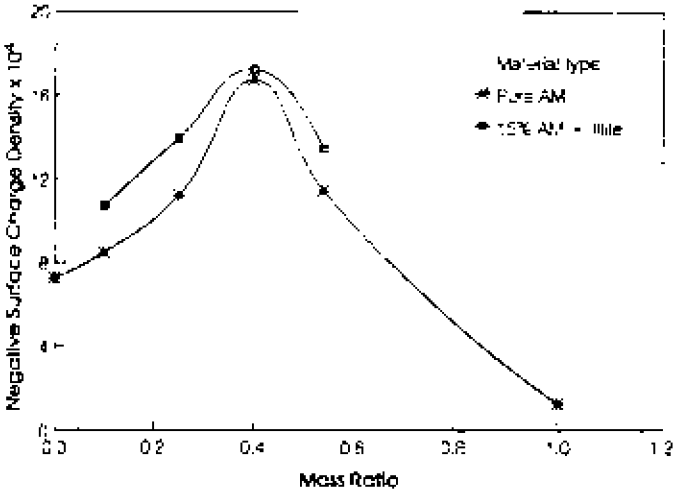

FIG. 5. Negative surface charge density – mass ratio relations.

and AEC were measured at a pH of 7 (solution pH) to provide the same basis for comparison of surface-charge characteristics. This is necessary because the CEC and AEC of soils are functions of the pH environment (Duquette and Hendershot 1987). The CEC values determined by the NH^{4+} adsorption technique for some selected samples were comparable with those obtained by the silver-thiourea method. Thus, the CEC values presented in this section are those determined by the latter technique.

Figure 3 shows the CEC results for both the amorphous complex and the admixtures. The measured CEC values range from 8.0 mequiv./100 g for the pure amorphous iron to 82.0 mequiv./100 g for the MR = 0.40 amorphous complex. An intermediate value of 55 mequiv./100 g was obtained for the pure amorphous silica. In contrast with the trend shown by the SSA relationship, the CEC is an inverted, V-shaped curve with a maximum value at MR = 0.40. A similar trend is shown for the admixtures. Since the CEC of the illitic soil is 16.0 mequiv./100 g, the addition of the 15% amorphous complexes serves to increase the CEC of the admixtures to about 25 mequiv./100 g at MR = 0.4.

Whereas one would expect the CEC to increase with an increase in the SSA of the amorphous complex or admixture, the contrary is obtained, i.e., the maximum CEC is obtained when the SSA is at a minimum, at MR = 0.4 (refer to Fig. 2). This apparent contradiction is in actual fact supported by the earlier work of Herbillon and Tran Vinh An (1969), where an increase in CEC was observed with increasing MR. The proposition of isomorphous substitution of silica atoms by iron during the formation of the amorphous material has been made through a process which suggests that when the hydrous silica and iron ions were coprecipitating in the aqueous solution, a number of Si^{4+} ions can be replaced by Fe^{2+} ions. Thus, instead of forming $Si(OH)_4^0$, $Fe(OH)_4^-$ is produced. The latter bears one negative charge, whereas the former is neutral. The concept of isomorphous substitution in amorphous materials was initially proposed by Cloos *et al.* (1986) for the coprecipitated silica–alumina hydroxide, where the silica atoms can be partially isomorphous substituted by aluminum ions. Most recently, Si^{4+}–Fe^{2+} substitution (Si^{4+} by Fe^{2+}) was also suggested by Decareau *et al.* (1987). It is, however, not yet immediately clear how isomorphous substitution occurs and why it is maximized at an MR of around 0.40. It would be expected that not all of the negative charges on the surfaces of the silica-iron hydroxide are the result of isomorphous substitution, since the presence of broken bonds could constitute another source of negative charges. The former charges are permanent, whereas the latter are variable, i.e., pH-dependent charges.

The structure of the amorphous complex shown in Fig. 4 is postulated on the basis of the following observations: (*i*) existence of Si^{4+}, Fe^{2+}, OH (O and H^+); (*ii*) the amorphous complex is solid; (*iii*) abundance of electric charges arising from broken bonds; (*iv*) isomorphous substitution of Si^{4+} by Fe^{2+}; and (*v*) polymerism of molecules. The portrayal of both negative and positive charges on the surface of the amorphous solid shown in Fig. 4 recognizes that the negative charges are due to both isomorphous substitution and the presence of broken bonds and that the positive charges arise only from the effect of broken bonds. The charges associated with the broken bonds can vary in sign depending on the pH of the system (environment). By and large, a decrease in pH is associated with an increase in the amount of positive charges arising from deprotonation of hydrogen (pronation of oxygen) atoms. It is conceivable that significant hydrogen bonding may occur both within and outside the amorphous domains, as suggested by the infrared spectrometry results, since there are numerous hydroxyls. Moreover, a certain amount of cations, mostly sodium in this case, can be adsorbed on the surfaces of the amorphous complex's particles by the negative charges. The amount adsorbed is proportional to the negative surface charges, i.e., CEC. It is also likely that some cations can be entrapped between two units of the amorphous material complex.

To provide a means for quantification of the surface activity, the concept of negative surface charge density (NSCD) is introduced. The NSCD, which is expressed as the ratio of CEC to surface area (mequiv./m^2), provides an indication of the amount of negative charges per unit area. The higher the NSCD, the greater is the negativity. Figure 5 shows that the NSCD is maximized when MR = 0.40 and that a value as low as 1.2×10^{-4} mequiv./m^2 is obtained

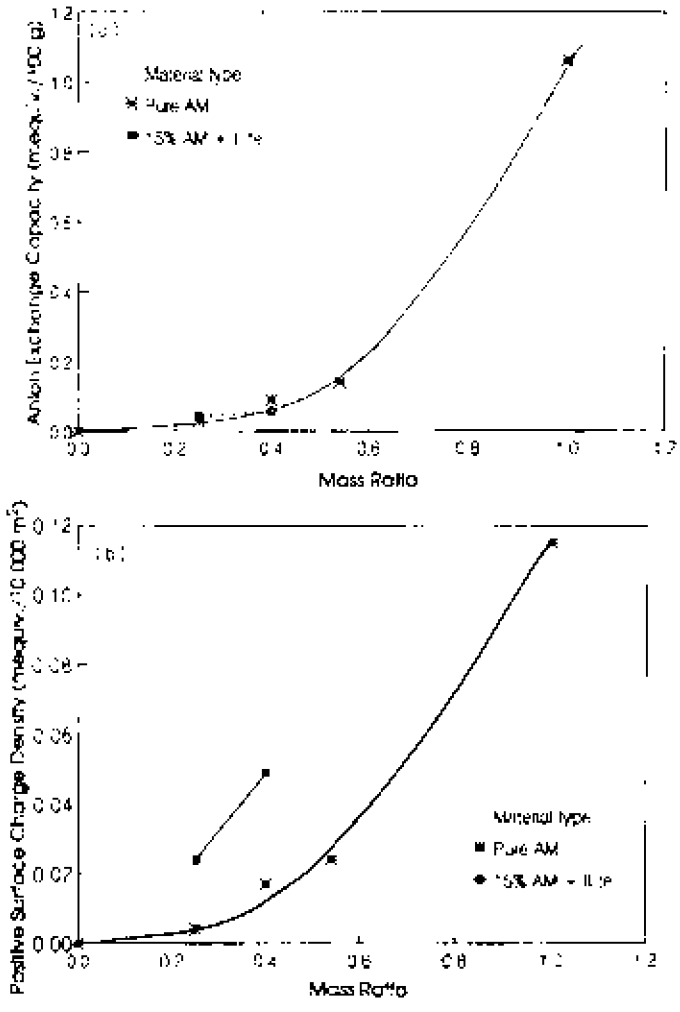

FIG. 6. (*a*) Anion exchange capacity – mass ratio relations. (*b*) Positive surface charge density – mass ratio relations.

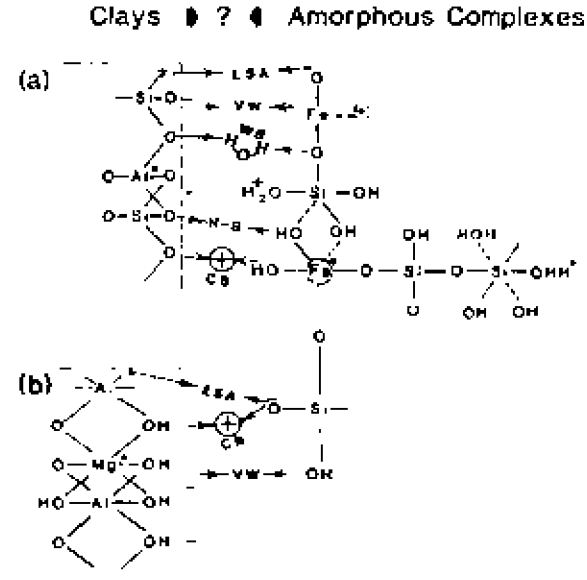

FIG. 7. Illustration of clay-amorphous silica-iron complex interaction-bonding mechanisms. CB, cation bridging; ESA, electrostatic attraction; H–B, hydrogen bonding; VW, van der Waals; WB, water bridging; *, replaced by element shown.

for pure amorphous iron, in contrast with 16.4×10^{-4} mequiv./m^2 at MR = 0.40. This suggests that a very small amount of negative charges are associated with pure amorphous iron and that the negative charge density is significantly increased with the addition of amorphous silica, i.e., up to MR = 0.40.

The NSCD for the clay – amorphous complex admixtures also shows a maximum value at MR = 0.40, as seen in Fig. 5. For the pure illitic soil, the NSCD value calculated from the CEC and specific surface area for the soil given in Table 2 is 18.0×10^{-4} mequiv./m^2. Whereas a comparison of the NSCD values for the soil admixture at various MRs with the corresponding NSCD values for the amorphous complex shows that the NSCD of illitic clay is higher than that for the amorphous complex, the values are still lower than the NSCD value for the pure illitic soil. This is consistent with the expectation that any addition of low-NSCD amorphous complexes will reduce the overall NSCD of the illitic soil.

The AEC values for the pure amorphous iron and the illite soil were obtained as 1.0 and 0.05 mequiv./100 g, respectively. The AEC values for the amorphous complex and soil admixtures and their respective positive surface charge density (PSCD, i.e., AEC/SSA) variations with MR are shown in Figs. 6*a* and 6*b*, respectively. It is seen that the AEC values are generally much lower than the CEC values, especially for those with a MR less than 0.54. The increasing trend of AEC and PSCD with increasing MRs noted in the figures may be attributed to the increasing iron content. The admixtures of illite soil and amorphous materials show higher PSCDs in contrast with the amorphous complex for the two MRs portrayed in Fig. 6*b* because the SSAs of the admixtures are lower than those of the amorphous materials. Although the amount of positive charges is low, it is expected that the positive charges would contribute to the total interactive forces through electrostatic attraction.

Since the amorphous materials possess both positive and negative charges, polymerization of the amorphous colloids can occur in the development of an amorphous-clay soil structure, resulting in an arrangement where growth and attachment of the amorphous "polymer" to clay particles produces chain-like clay – amorphous materials. Figure 7 illustrates the possible interactions that might occur between clay minerals and the amorphous complex, with assumed isomorphous substitution occurring in the clay minerals. The development of the arrangements shown in Fig. 7 recognizes the potential for the following interactive mechanisms. (1) *Electrostatic attraction between clay surfaces and amorphous colloids.* (2) *Cation bridging through adsorbed cations, as a special case of electrostatic attraction.* This can be significant, since the materials show high negative surface charges, especially at MR = 0.40, as indicated by their CEC values. The higher the negative charges, the higher the bridging strength. (3) *Hydrogen bonding, i.e., O–H bonds between the clay minerals and the amorphous complex.* The IR results, which indicate the presence of significant O–H bonds, suggest that the amorphous complex may have penetrated the Stern layer and become physically adsorbed onto the mineral surfaces, thereby enhancing the van der Waals forces. Support for the bond formation is found in the scanning electron micrographs (Figs. 13*b*–13*d*), where

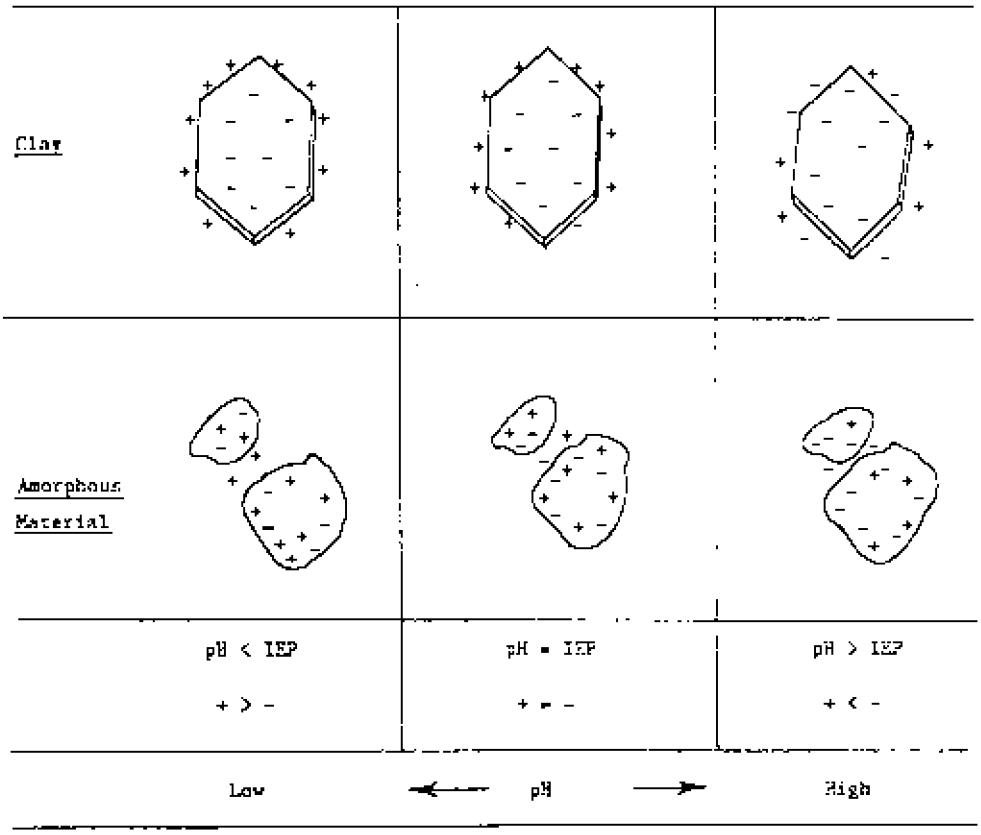

FIG. 8. Presentation of surface charge relative to isoelectric points (IEP).

amorphous coating of the faces of the clay minerals is shown. It should be noted that under certain situations such as that shown, for example, in Fig. 7*b* (gibbsite or brucite), O-H bonds would not be formed where the hydroxyls are exposed to the amorphous material, inasmuch as the hydroxyls at one face of the clay minerals (i.e., chlorite) are hydroxylated. This speculation is supported by the IR results, which will be discussed later. A maximum strength of hydrogen bonding has been measured for soils with amorphous material composed at MR = 0.40. (4) *Water bridging through O-H bonds of water molecules.* This is admittedly a weak bond. (5) *Van der Waals forces.* (6) *Other bonding mechanisms yet to be identified.*

Zeta potential (Zp)

The schematic representation of the general nature and distribution of the charges associated with the amorphous material and clay particles given in Fig. 8 is similar to the one depicted previously by Yong and Ohtsubo (1987) and is used to interpret the Zp measurements for the various amorphous complexes and clay admixture given in Fig. 9 in relation to pH variation. Interpreting the Zp as a measure of the electrokinetic properties, and as a reflection of the total positive and negative charges from all sources, i.e., the net resultant effect, the values measured at various pH levels may be used to estimate the so-called isoelectric points (IEP) of the mixtures (Yong and Ohtsubo 1987). Since the IEP is the pH value at which the net resultant electric charges on the surfaces of the solid from all sources are equal to zero, the electrokinetic potential is expected to be zero at the IEP. Figure 8 demonstrates the influence of the IEP in relation to the changes in the sign of the charges associated

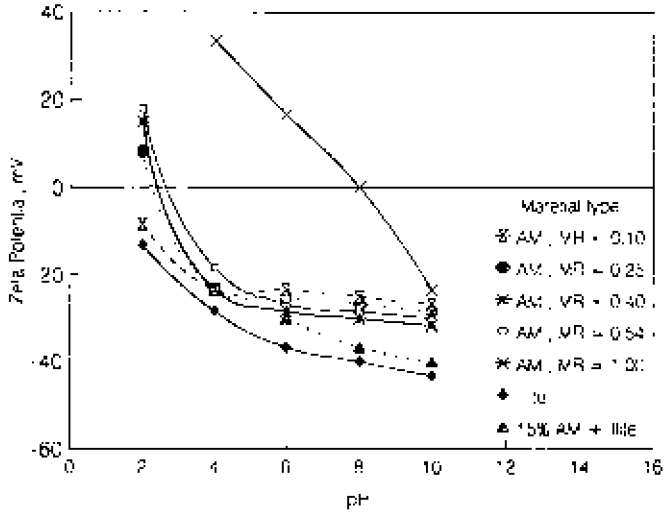

FIG. 9. Zeta potential variations with pH.

with the amorphous complex and the edge charges of the clay particle. The two considerations used to depict the charges associated with the clay mineral and amorphous complex are as follows: (*i*) most clay minerals have both negative or permanent charges on their faces and positive or variable charges on their edges, and the permanent charges do not vary with the pH environment, whereas the variable charges on the edges do change with pH; and (*ii*) the amorphous complex possesses abundant negative charges from broken bonds and isomorphous substitution, but relatively few positive charges, (with the exception of amorphous iron), and the charges associated with the broken

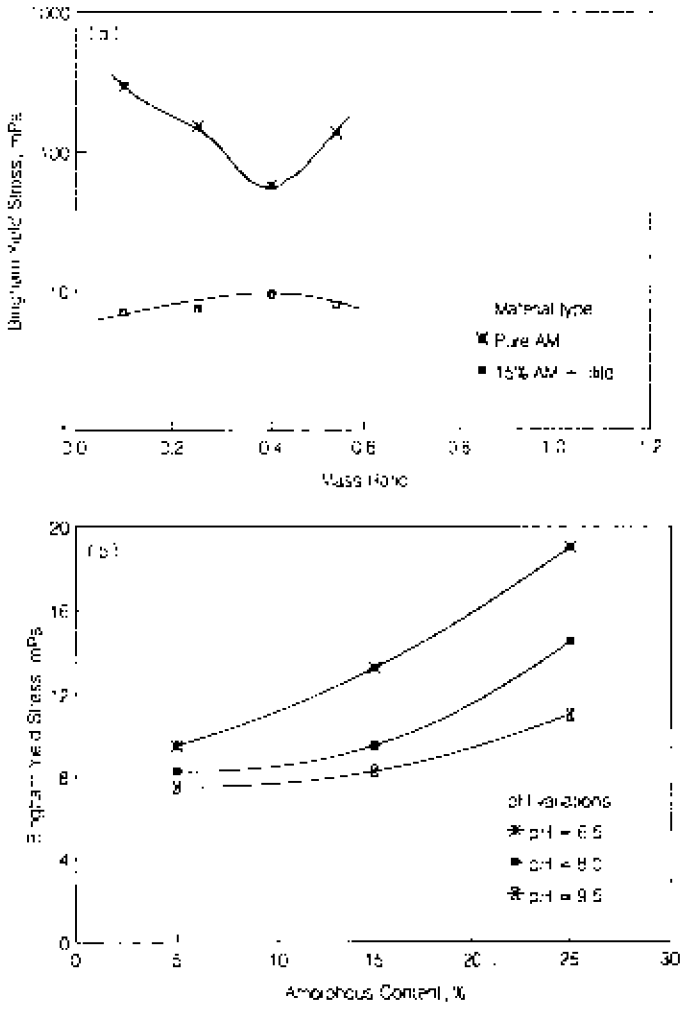

FIG. 10. (*a*) Bingham yield stress – mass ratio relations; pH = 8, 10% solids. (*b*) Bingham yield stress – amorphous content relations.

bonds are variable in sign according to the IEP pH of the system.

The net charge of the amorphous complexes and clay admixture shown in Fig. 9 varies from negative to positive as the pH of the system passes through the IEP. From the measured ZP values shown in Fig. 9 for (*i*) the amorphous complexes, (*ii*) the laboratory illitic soil, and (*iii*) the soil admixture, the IEP values determined from the intersections of the plotted curves with the Zp line can be obtained. It is interesting to note that the addition of 15% amorphous complex (MR = 0.40) did not significantly alter the shape of the Zp curve for the illite soil. Another striking feature of the results is shown in the shapes of the Zp curves for the various amorphous complexes with MRs ranging from 0.10 to 0.54. These curves are quite similar and relatively close to each other. Accordingly, the IEPs for these complexes are not significantly different. In the case of pure amorphous iron (i.e., MR = 1.0), one observes a significant difference in the shape and position of the curve, and correspondingly the IEP is significantly different from the rest of the amorphous complexes. The large difference in the Zp shown between the pure amorphous iron and the other amorphous complexes, where amorphous silica forms part of the complex, suggests that the presence of the amorphous silica, which is abundant in negative charges, influences the net charge (to the negative side). This experimental results obtained confirm the low AEC values measured for this group of amorphous complexes. Considering the Zp results in combination with the CEC, AEC, NSCD, and PSCD results, one is led to conclude that negative charges predominate on the surfaces of the amorphous complexes (excluding amorphous iron) and the clay admixtures under "normal" pH conditions (pH 5–10). This, however, does not exclude the existence of a some positive charges, especially for iron-rich amorphous complexes, i.e., MR = 0.40 and 0.54.

Bingham yield stress (BYS)

Initially, a solids concentration of 10% (w/w) suspension, similar to that used by Yong and Ohtsubo (1987), was selected for both amorphous complexes and the soil admixtures. Since the amorphous complexes appeared as thick gels, especially for the MR = 0.10, the solids concentration was reduced to 5% to facilitate testing. As can be seen in Fig. 10*a*, the rheological behaviour of the amorphous complexes is related to the MR. The Bingham yield stress (BYS) is observed to decrease significantly with an increase in the MR, up to a value of 0.40, apparently due to the viscosity of the complex. The effect of pH on the BYS of the clay admixture with 15% amorphous complex at MR = 0.40 was also evaluated, as illustrated in Fig. 10*b*. The BYS increases with a decrease in pH from 9.5 to 6.5, due apparently to the increased interparticle electrostatic attraction with decreasing pH. The same trend of change with pH was also observed for the consistency limits.

As the same given composition of amorphous complex, i.e., MR, the experimental results portrayed in Fig. 10*b* show an increase in BYS with an increase in the amount of admixed amorphous complex, due apparently to the increased viscosity and bonding action of the amorphous complex. A lowering of the soil pH towards acid conditions ensures a more flocculant aggregated particle arrangement and hence favours clay particle – amorphous complex interactions, as reflected in the measured increased BYS (see Fig. 10*b*). In association with the flocculation of particles, electrostatic attractions arising from a higher edge(+) to face(−) configuration and forces are enhanced. Furthermore, it is expected that edge(+) to face(−) association development is favourably promoted as the pH moves towards the IEP, at which time maximum electrostatic attraction would occur as a result of the presence of equal amounts of positive and negative charges. This evaluation of increasing BYS with decreasing pH is in agreement with the work by Yong and Ohtsubo (1987), concerning the variation of BYSs with pH for a kaolinite–ferryhydrite system. Their results showed that the kaolinite and its admixtures with ferrihydrite (amorphous iron) produced maximum BYS values around the IEP.

Infrared spectrometric study

Even though infrared spectrometry (IR) is mainly to study the presence and strength of organic functional groups, useful results were obtained to permit one to interpret the mechanisms of mineral – amorphous complex interaction. The presence of abundant hydroxyls in the amorphous complexes increases the likelihood of hydrogen bonding between the clay minerals and amorphous complexes; a likelihood that can be evaluated through IR analysis inasmuch as the pur-

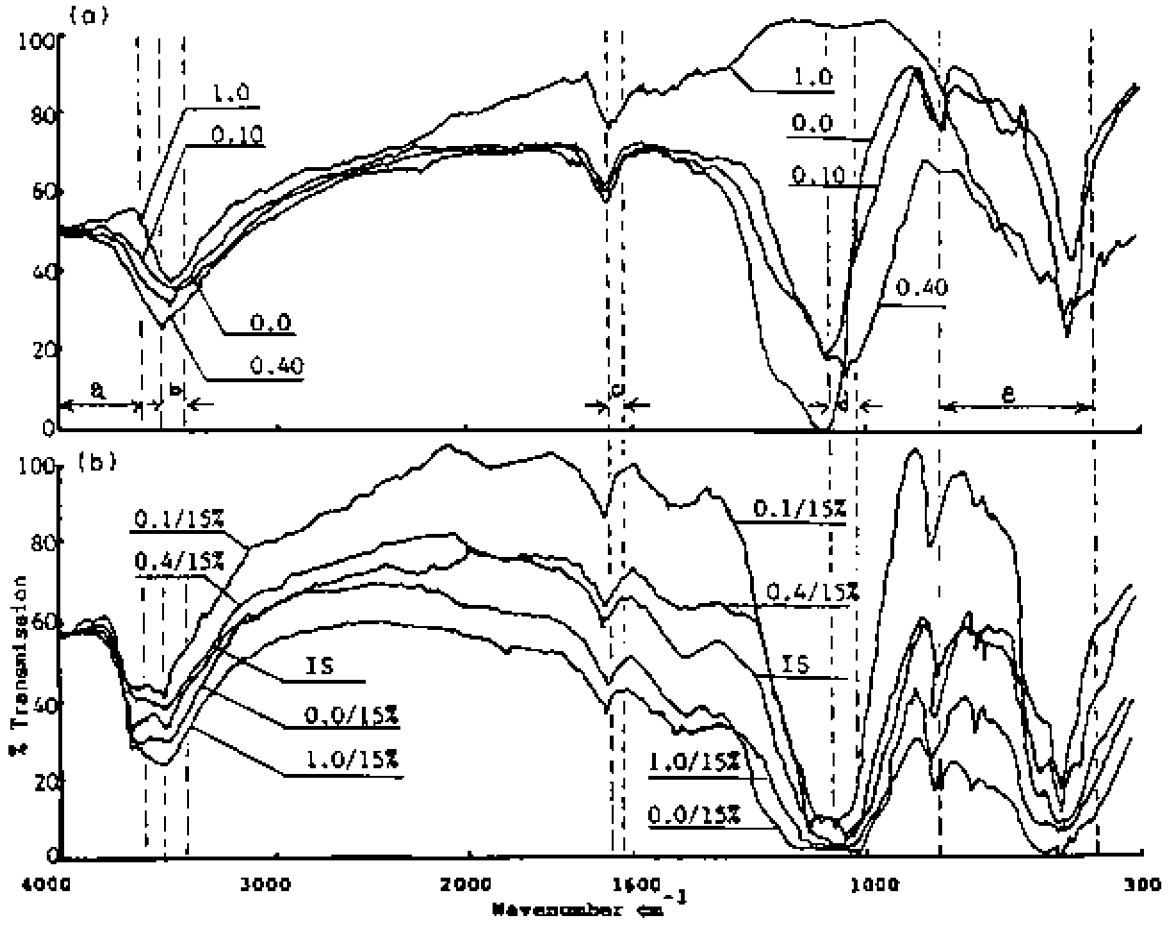

FIG. 11. Infrared spectra of amorphous material and its admixtures with clays. (*a*) Amorphous complexes. (*b*) Amorphous complex admixtures with illitic soils (IS).

pose of IR is to detect the presence and, hence, to quantify the strength of hydrogen bonding.

Figure 11 shows the IR results of the amorphous complexes and the amorphous complex admixtures with illitic soil. The IR pattern of the blank specimen (potassium bromide, KBr) used as an inert media, showed no peak but a clear background. The results noted from the IR patterns for the individual samples indicate that there are five main peak frequency bands representing, respectively (from high to low frequency), (*a*) free O–H; (*b*) bonded O–H, including intra- and intermolecular and dimeric–polymeric bonds; (*c*) capillary condensed or absorbed O–H either polymolecularly or by monolayer; (*d*) Si–O; and (*e*) unidentified. A summary of peak frequency and intensity of each individual sample is given in Table 3, which is taken directly from the experimental data shown in Fig. 11. The first description in Table 3 is the wavelength, and the second is the intensity at the specified wavelength. The descriptions of each frequency band in terms of (*i*) intensity, (*ii*) functional group, and (*iii*) type of vibration of that functional group are summarized in Table 4, based on the work of Kiselev and Lygin (1975) and Parker (1971). Free – partially free O-Hs are seen to be present mainly in the illitic soil. An interesting observation concerns the next three bands, especially *b* and *d*. In band *b*, peak frequency is shifted upwards as the MR of amorphous complexes varies from 0 to 0.40. Moreover, the maximum shift towards a higher frequency number occurs at MR = 0.40, where the strongest hydrogen bonding appears. Correspondingly, most samples exhibit reduced O-H peak intensities at MR = 0.40. A similar observation is obtained for the weak O–H group in band *c*. It is suspected that an increase in O–H bonding strength must be accompanied by a relevant decrease in the bonding strength of an adjacent group. Indeed, in band *d*, a reverse relationship, opposite to the O–H bonds, is observed between the peak frequency shift and the MR for the Si–O interaction. More specifically, the weakest Si–O bonding strength is found to occur critically for the sample with MR = 0.40. This phenomenon is known as the bathochromatic effect. Two possibilities may explain the observed bathochromatic effect. Firstly, the silicon in the

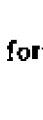

Si–O group acts with the adjacent hydroxyls to form –Si–O

groups, and this interaction can apparently weaken the Si–O intermolecular bonding strength. Secondly, because of silico-iron polymerization and isomorphous substitution, Fe may occupy a position next to the Si–O group, forming an Si–O–Fe chain as shown in Fig. 4. Since iron is more chemically active than silicon in terms of protonation, the in-between oxygen is attracted to the iron, thereby resulting in a reduction of Si–O bonding strength. It is very likely that

TABLE 3. Infrared study results of soil samples showing peak frequency and intensity

Class	Band range (wave number, 1/cm)	Amorphous material (MR) Si(OH)$_4$ 0.0	0.10	0.40	Fe(OH)$_3$ 1.0	Illitic soil	Illitic soil + amorphous 0.0/15%	0.1/15%	0.4/15%	1.0/15%
a	4000–3600					3600(27)				
b	3500–3400	3410(31)	3435(37)	3460(26)	3400(35)	3400(28)	3420(22)	3630(25)	3460(31)	3410(16)
c	1645–1620	1635(61)	1645(61)	1635(39)	1630(76)	1643(55)	1620(40)	1630(54)	1640(61)	1630(34)
d	1090–1020	1090(<0)	1085(18)	1030(15)		1035(<0)	1060(<0)	1050(<0)	1020(2)	1030(<0)
e	800–400									

NOTES: Values in the table are peak frequency, with intensity (percent transmission) given in parentheses.

TABLE 4. Characteristic infrared bands of various groups encountered

Class	Frequency range (wave number, 1/cm)	Intensity	Group	Type of vibration	Description
a	4000–3600	Variable	O–H	Stretching	Free to partially free O–Hs
b	3500–3400	Strong (sharp)	O–H	Stretching	Bonded O–Hs including intra- and intermolecular and dimeric-polymeric bonds
c	1645–1620	Weak (sharp)	O–H	Stretching	Capillary condensed or absorbed O–Hs either polymolecularly or by monolayer
d	1090–1020	Strong (broad)	Si–O	Stretching	Bonding from and Si–O–Si, H, Si–O–Fe
e	800–400	Variable (broad)	?	Stretching	Vibration of Si, Fe Al, O, and H interactions

NOTE: Table based on Kiselev and Lygin (1975) and Parker (1971).

both mechanisms can occur simultaneously in the reduction of Si–O bonding strength.

Scanning electron microscopy (SEM)

SEM micrographs (photographs) were obtained for some selected samples aged for 3 months. Analyses of their microstructure are made based mainly on the following observations and comparisons.

Amorphous material

Figures 12*a*–12*d* present the micrographs of the amorphous complexes with MRs of 0 (pure silica), 0.10, 0.40, and 1 (pure iron), respectively. One common observation made from the four micrographs is the irregular shape of their microstructures, which confirms the XRD study. Unlike the clay minerals, this noncrystalline matter (amorphous material) does not take the form of plates or indicate sharp edges, but rather spherical floc units that form large amorphous material clouds, as seen from the micrographs, especially from (Fig. 12*c*), where the MR = 0.40. The difference between amorphous silica (Fig. 12*a*) and iron (Fig. 12*d*) is not only the opacity, as seen very clearly by eye, but also the form, which consists of large uniform, smooth-looking clouds, compared with the latter, which is seemingly less uniform and rougher. The silica-iron mixed hydroxide at MR = 0.10 (Fig. 12*b*) and MR = 0.40 (Fig. 12*c*) shows a very distinct fabric arrangement. In terms of shape, the MR = 0.10 amorphous complex is more uniform and finer, whereas the latter is uniform but is coarser and tends to aggregate. Moreover, it is very easy to identify each individual fabric unit in Fig. 12*c*, where the spherical-shaped particles can be observed. This is, perhaps, an indication of strong intermolecular attraction, resulting probably from the hydrogen bonding detected in the IR test, cation bridging, coulombic forces, etc.

Illitic clay and amorphous material

The illitic clay, as shown in Fig. 13*a*, is seen to have no amorphous material coating on most of the particle surfaces, though some fine particles, located in the centre, are seen.

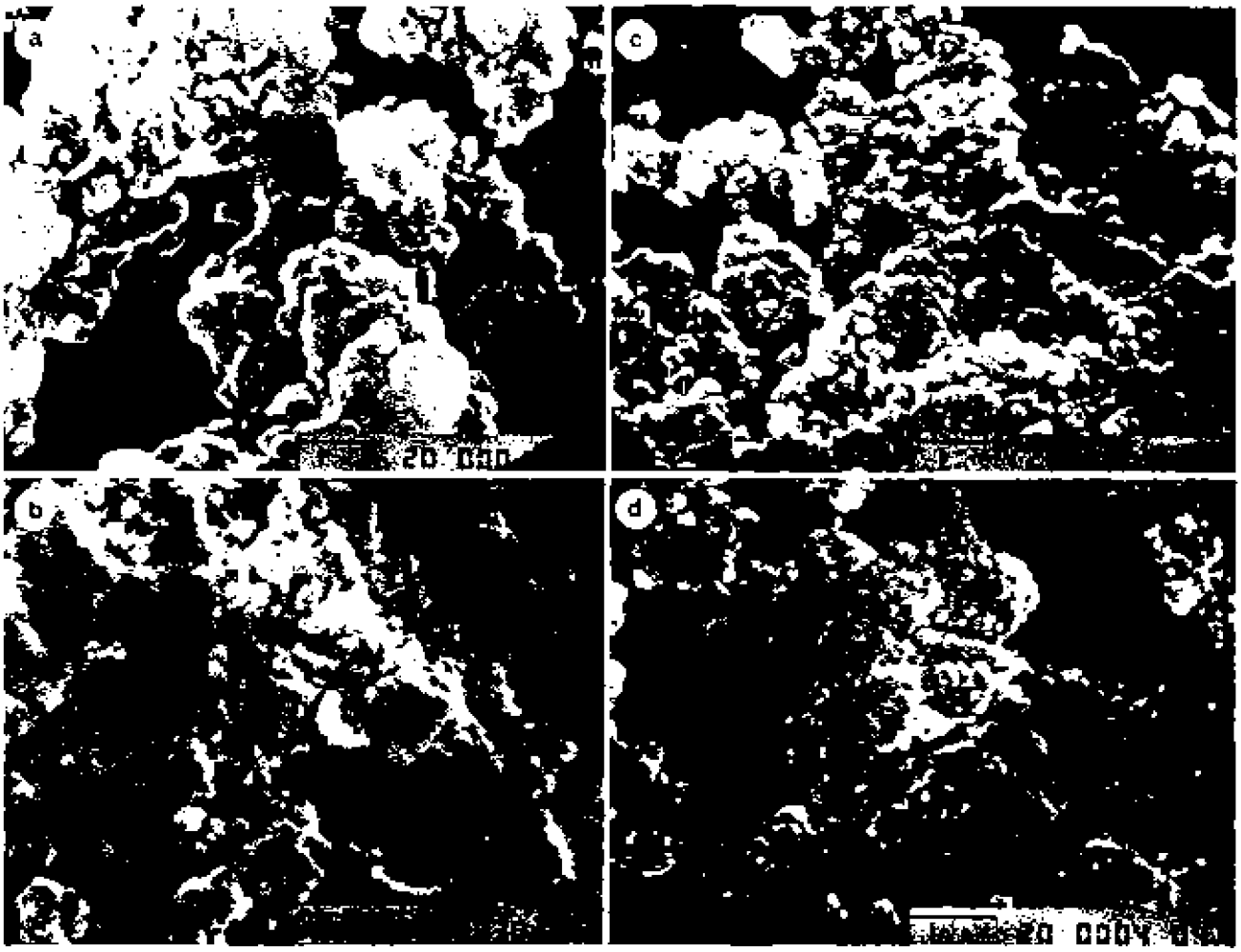

FIG. 12. SEM microphotography of amorphous material complexes with mass ratios of 0 (*a*), 0.1 (*b*), 0.4 (c), and 1.0 (*d*). Scale bars = 1 μm.

These fine particles may consist of colloid fractions of both minerals and original amorphous matter. One may notice that coating of amorphous colloids onto clay particles occurs immediately after the amorphous material is introduced. In Figs. 13*b*–13*d*, amorphous colloids are adsorbed mainly on the faces of the fine particles, whereas the edges remain mostly free of colloids. This evidence suggests that at pH 8.0, the negatively charged amorphous material is attracted to the negative faces of clay particles by at least three mechanisms: (*i*) O–H bonding, (*ii*) cation bridging action, and (*iii*) coulombic (electrostatic) forces.

The first mechanism has been substantiated by the IR results obtained, as discussed previously. The second mechanism can be deduced from the high negative surface charges (CEC) measured. As noted previously, cations exist in between the faces of the clay particles and amorphous colloids, forming a bridge. The third mechanism is directly inferred from the results of the CEC and ACE measurements, in relation to the negatively charged faces that electrostatically attract the positively charged edges of the clay particles.

The effect of remoulding can be seen in the micrograph shown in Fig. 13*d*, where a collapsed structure with a more face-to-face association is observed, with some amorphous coating on the faces. The microphotograph shown in Fig. 14 for pH = 6.5 indicates that no significant difference can be noticed, except that more coating of amorphous particles seems to exist in contrast with that of MR = 0.40 at pH 8.0. The increasing tendency of amorphous material coating with decreasing pH to pH 6.5 is due primarily to the increased electrostatic attraction. This experimental finding matches the previous work reported by Yong and Ohtsubo (1987).

Concluding remarks

The experimental results obtained from this study indicate that amorphous materials consisting of Fe_2O_3 and SiO_2 will exhibit different properties and characteristics depending on the proportions of Fe_2O_3 and SiO_2. Addition of the amorphous materials of various proportions (i.e., amorphous complexes) to the illitic clay studied shows that the properties of the clay admixture will also vary according to the properties of the amorphous complex, albeit to a lesser degree. The properties and behaviour observed for the amorphous complexes and the clay admixtures can be linked directly to the large specific surface area and high surface charge of the amorphous complexes. The specific surface area measured for the amorphous complexes varies from almost 800 m^2/g to a minimum of 500 m^2/g and subsequently to a value of 677 m^2/g as the mass ratio increases from 0 to 0.40 to 1, respectively. Cation exchange capacity

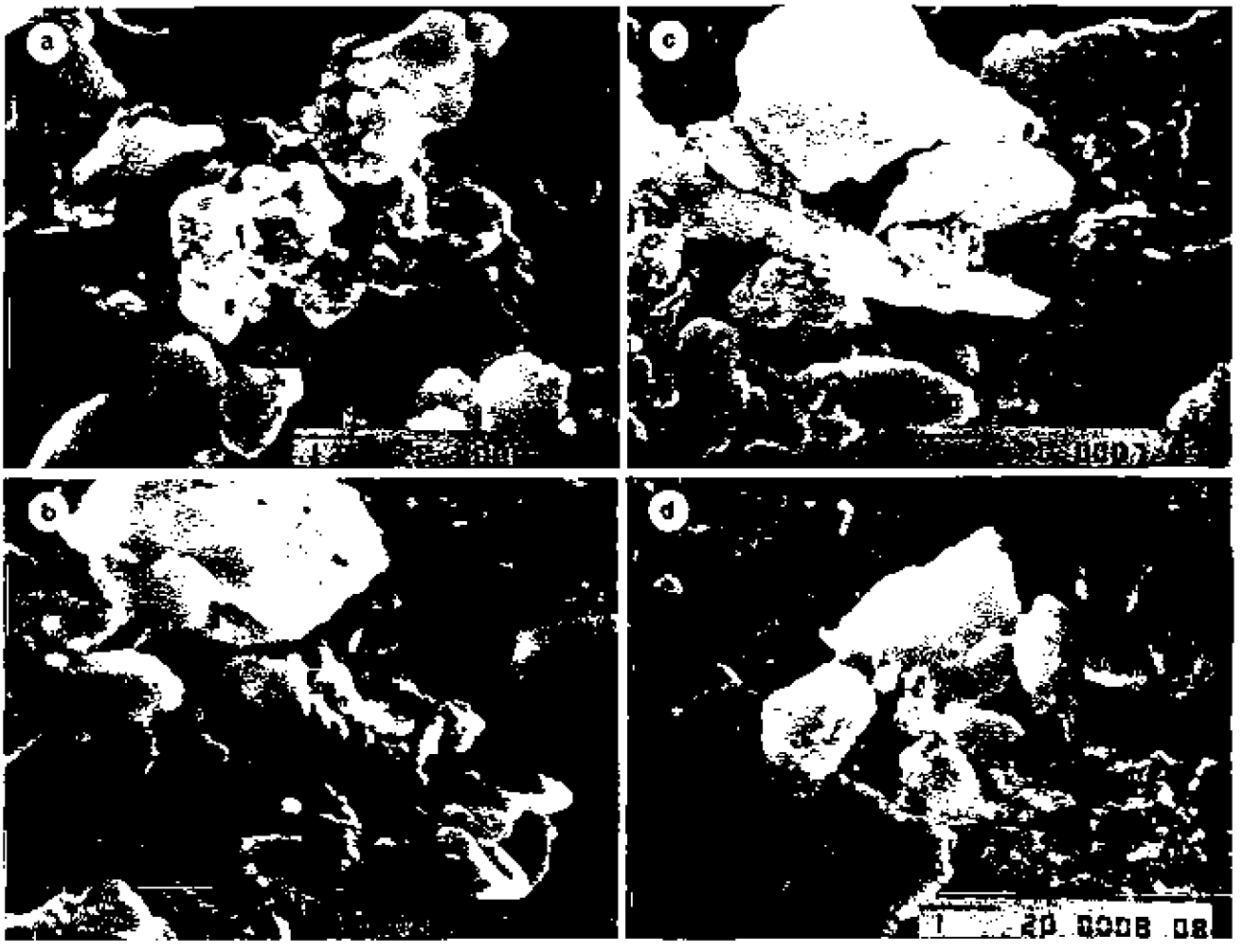

FIG. 13. SEM microphotographs of (*a*) illite soils, (*b*) illite soil and 15% amorphous material at a mass ratio of 0.10, (*c*) illite soil and 15% amorphous material at a mass ratio of 0.4 in undisturbed state, and (*d*) illite soils and 15% amorphous material at a mass ratio of 0.4 in remoulded state. Scale bars = 1 μm.

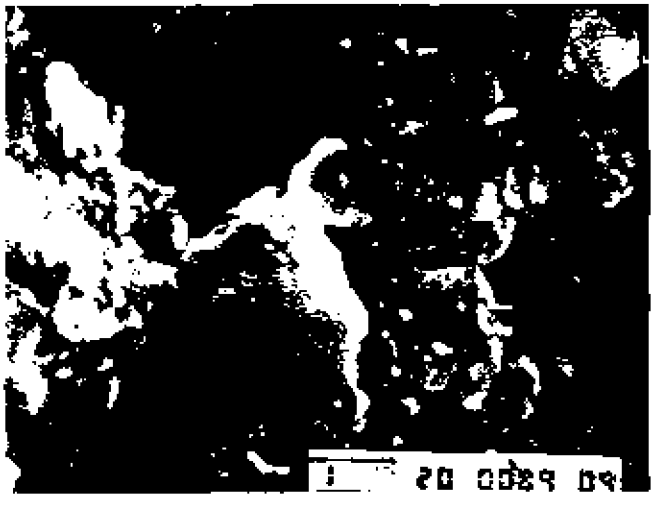

FIG. 14. SEM microphotograph of illite soil and 15% amorphous material at a mass ratio of 0.4 and pH = 6.5. Scale bar = 1 μm.

measurements indicate values of 54.9 mequiv./100 g for MR = 0, 82.0 mequiv./100 g for MR = 0.40, and 8.0 mequiv./100 g for MR = 1.

The contribution of amorphous complexes to the clay – amorphous complex mixtures (clay admixtures) is twofold: firstly by the amount of amorphous complex in the clay admixture, and secondly by the composition of the amorphous complex used. The contribution from the amorphous complex is in two forms: water-holding capacity and bonding action. When the amorphous complex present in the clay admixture consists primarily of silica (up to a mass ratio of 0.25) or mainly of iron (beyond a mass ratio of 0.60), the resultant specific surface area is large, thereby producing a large water-holding capability. However, when the amorphous complex has a mass ratio at or close to 0.40, the resultant minimal specific surface area will produce correspondingly minimum plasticity and water-holding capacity.

Because of the presence of pH-dependent surface charges associated with the amorphous complexes, the physicochemical properties and behaviour of the clay admixtures (e.g., liquid limits and zeta potential) vary with the pH environment. Coating of amorphous colloids onto clay particle surfaces, shown by scanning electron microscopy, appears to be enhanced by a decrease in pH from 8.0 to 6.5 of the system. It may be deduced that this enhancement is due to the increased electrostatic attraction which is a result of the increased amounts of positive charges on the amorphous colloids.

Acknowledgement

This study was conducted under a grant in aid of research from the Natural Sciences and Engineering Research Council of Canada (grant no. A-882).

American Society for Testing and Materials, ASTM. 1989. Annual Book of ASTM standards, sect. 4, vol. 4.08, Philadelphia.

Bentley, S.P., and Smalley, I.J. 1978. Interparticle cementation in Canadian post-glacial clays and the problem of high sensitivity (S_t > 50). Sedimentology, 25: 297–302.

Bentley, S.P., and Smalley, I.J. 1984. Landslips in sensitive clays. *In* Slope instability. *Edited by* D. Brunsden and D.B. Prior. John Wiley & Sons Ltd., London, pp. 457–490.

Boyd, S.A., Mortland, M.M., and Chiu, C.T. 1988*a*. Sorption characteristics of organic compounds on hexadecyltrimethylammonium-smectite. Soil Science Society of America Journal, 52: 652–657.

Boyd, S.A., Lee, J.F., and Mortland, M.M. 1988*b*. Attenuating organic contaminant mobility by soil modification. Nature (London), 333: 345–347.

Chhabra, R., Pleysier, J., and Cremers, A. 1975. Cation exchange capacity and exchangeable cation in soils: a new method. Proceedings, International Clay Conference, Mexico City, pp. 439–499.

Cloos, P., Leonard, A.J., Moreau, J.P., *et al.* 1969. Structural organization in amorphous silico-aluminas. Clays and Clay Minerals, 17: 279–289.

Conlon, J.M. 1966. Landslides on the Toulnustouc River, Quebec. Canadian Geotechnical Journal, 3: 113–144.

Decareau, A., Bonnin, D., Bandaut-Trauth, D., *et al.* 1987. Synthesis and crystallogenesis of ferric smectite by evolution of Si–Fe coprecipitates in oxidizing conditions. Clay Minerals, 22: 207–223.

Duquette, M., and Hendershot, W.H. 1987. Contribution of exchangeable aluminum to cation exchange capacity at low pH. Canadian Journal of Soil Science, 67: 175–185.

Eltantawy, I.N., and Arnold, P.W. 1973. Reappraisal of ethylene glycol monoethyl ether (EGME) method of surface area estimation of clays. Journal of Soil Science, 24: 232–238.

Fuller, W.H., and Warrick, A.W. 1985. Soils in waste treatment and utilization. CRC Press Inc., Boca Raton, Fla., vol 2, p. 229.

Gastuche, M.C., Bruggenwert, T., and Mortland, M.M. 1964. Crystallization of mixed iron and aluminum gels. Soil Science, 98: 281–289.

Greenland, D.J., and Hayes, M.H.B. 1981. The chemistry of soil processes. A Wiley-Interscience Publication, John Wiley & Sons, New York.

Haynes, J.E., and Quigley, R.M. 1976. Mineralogy and physicochemistry of Leda clays from deep boreholes, Hawkesbury, Ontario. Geological Branch, Ontario Division of Mines, OFR 5214.

Hendershot, W.H., and Carson, M.A. 1978. Changes in the plasticity of a sample of Champlain Clay following removal of salt and amorphous material. Canadian Geotechnical Journal, 15: 609–616.

Herbillon, A., and Tran Vinh An, J. 1969. Heterogeneity in silicon-iron mixed hydroxides. Soil Science, 20: 223–235.

Hiemenz, P.C. 1977. Principles of colloid and surface chemistry. Marcel Dekker, New York.

Jackson, M.L. 1967. Soil chemical analysis. Prentice-Hall of India Private Limited, New Delhi.

Kiselev, A., and Lygin, V. 1975. Infrared spectra of surface compounds. John Wiley & Sons Inc., New York.

Locat, J., Lefebvre, G., and Ballivy, G. 1984. Mineralogy, chemistry, and physical properties interelationships of some sensitive clays from Eastern Canada. Canadian Geotechnical Journal, 21: 530–540.

Loiselle, A., Massierra, M., and Sainani, U.R. 1971. A study of the cementation bonds of the sensitive clays of the Outardes River region. Canadian Geotechnical Journal, 8: 479–498.

McKyes, E., Sethi, A.J., and Yong, R.N. 1974. Amorphous coatings on particles of sensitive clay soils. Clays and Clay Minerals, 22: 427–433.

Oyama, H., and Takehara, H. 1976. Revised standard soil color chart. 5th ed., Japan, pp. 1–15.

Parker, F.S. 1971. Applications of infrared spectroscopy in biochemistry, biology and medicine. Plenum Press, New York.

Quigley, R.M. 1980. Geology, mineralogy, and geochemistry of Canadian soft clays: a geotechnical perspective. Canadian Geotechnical Journal, 17: 261–285.

Quigley, R.M. 1983. Glacialacustrine and glaciamarine clay deposits: a North American perspective. *In* Glacial geology. *Edited by* N. Eyles. Pergamon Press Canada Ltd., Toronto, pp. 140–167.

Quigley, R.M. 1984. Quantitative mineralogy and preliminary porewater chemistry of candidate buffer and backfill materials for a nuclear fuel waste disposal vault. Atomic Energy of Canada Limited, AECL-7827.

Segalen, P. 1968. Note sur une méthode de détermination des produits minéraux amorphes dans certains sols à hydroxydes tropicaux. Cahiers ORSTOM, Série Pédologie, 6: 105–126.

Torrance, J.K. 1987. Quick clays. *In* Slope stability. *Edited by* M.G. Anderson and K.S. Richards. John Wiley & Sons Ltd., London, pp. 447–473.

Yong, R.N., and Ohtsubo, M. 1986. Inter-particle action and rheology of kaolinite – amorphous iron hydroxide (ferrihydrite) complexes. Applied Clay Science, 2: 63–81.

Yong, R.N., and Rao, S.M. 1991. Mechanistic evaluation of mitigation of petroleum hydrocarbon contaminated by soil medium. Canadian Geotechnical Journal, 28: 84–91.

Yong, R.N., and Sethi, A.J. 1977. Influence of amorphous material on soil performance and its relation to environmental weathering. Proceedings, 9th International Conference on Soil Mechanics and Foundations Engineering, Special Session on Geotechnical Engineering and Environmental Control, Tokyo, pp. 437–450.

Yong, R.N., Sethi, A.J., and LaRochelle, P. 1979*a*. Significance of amorphous material relative to sensitivity in some Champlain clays. Canadian Geotechnical Journal, 16: 511–520.

Yong, R.N., Sethi, A.J., Booy, E., and Dascal, O. 1979*b*. Basic characterization and effect of some characteristics on a sensitive clay from Outardes 2. Bulletin of the Association of Engineering Geologists, 14: 83–107.

Yong, R.N., Sethi, A.J., and Suzuki, A. 1980. Contribution of amorphous material to properties of a laboratory-prepared soil. Canadian Geotechnical Journal, 17: 440–446.

Appendix

Zeta potential (Zp)

Zeta potential is an experimentally determined potential measured in the diffuse double layer. The exact emplacement where this potential is measured remains questionable. Defined to be close to the shear plane of a colloid or a charged surface, Zp is often described as the potential at the surface of shear, very close to the Stern layer (Hiemenz 1979).

Direct association between Zp and a particle's surface and Stern layer renders this property a valuable tool to investigate adsorption and particle interactions. Changes in Zp and electrophoretic mobility could provide valuable information in the emplacement of adsorption (i.e., inside or outside the shear plane) (Hiemenz 1979) on (*i*) the formation of the adsorbed polymer, (*ii*) the polymer's ability to compress a particle's diffuse double layer, (*iii*) the countercharge effect of adsorbed polymers, and (*iv*) the selective adsorption of polymers on clay edges and (or) surfaces.

Zp changes could be directly used to evaluate the state of dispersibility of a system from a microscopic point of view, with application to a soil's dislocation, piping, and erosion susceptibility (Yong and Sethi 1977).

Method of calculation of Zp

Electrophoretic mobility was measured by tracking 10 individual particles per data point. Triplicate points were collected (total of 30 tracked particles) and averaged. Calculation of a sample's electrophoretic mobility (EM) was carried out as follows:

$$\mathrm{EM} = \frac{d}{t} \cdot \frac{10\ \mathrm{cm}}{V}$$

where d is length of micrometer division (160 μm), 10 cm is length of the cell tube, t is time in seconds to traverse one division, and V is voltage applied (volts). Zp (in mV) calculations were derived from the Helmholtz-Smoluchowski equation (Yong *et al.* 1987*b*), which reads as follows:

$$\mathrm{Zp} = \frac{4\pi \cdot \mathrm{Vt} \cdot \mathrm{EM}}{\mathrm{Dt}}$$

where Vt is viscosity (in poises (1 P = 0.1 Pa·s)) of the suspending liquid at 15°C, and Dt is dielectric constant of the suspending liquid at 25°C.